Variations in Laser-Induced Carbon from Structurally Varied Poly(furfuryl alcohol)

by

Emily Yip

A thesis

presented to the University of Waterloo

in fulfillment of the

thesis requirement for the degree of

Master of Science

in

Chemistry

Waterloo, Ontario, Canada, 2025

© Emily Yip 2025

Author's Declaration

I hereby declare that I am the sole author of this thesis. This is a true copy of the thesis, including any required final revisions, as accepted by my examiners.

I understand that my thesis may be made electronically available to the public.

Abstract

The laser-induced graphene technique, wherein a polymer precursor is irradiated by a CO_2 IR laser, provides a simple method for patterning of carbon materials like graphene or glassy carbon under ambient conditions. This is a highly attractive method of carbonization for applications in electronics and energy storage devices, and fine tuning of the laser-induced carbon's properties is permitted by the choice of precursor. For example, glassy carbon with its disordered structure and defects is desirable for high-performance supercapacitors and so an appropriate precursor can be selected to form glassy carbon by laser irradiation instead of graphene. However, direct structure-property correlations between the precursor and the nature of the resulting laser-induced carbon as well as its quality are unclear. To investigate this, poly(furfuryl alcohol) (PFA), a glassy carbon precursor that is infamously comprised of several structural motifs aside from its monomer unit, was synthesized under a variety of reaction conditions to create three series with different key structural features and then laser irradiated to analyze the resulting carbon material. Typical laser-induced carbon formed from PFA is more akin to glassy carbon, though varied lasing parameters and structures can potentially enable graphenization. Three series of PFA were prepared which exhibit varying degrees of polymerization, extents of ring opening, and high thermal stability. The PFA chemistry had a notable influence on the quality of the resulting laser-induced carbon, which demonstrated a broad range of ordering from an amorphous structure to that with more crystalline graphitic domains. Correlations between the PFA structure and laser-induced carbon quality showed that the most ordered carbon material formed when the PFA crosslinking was minimal and had high thermal resistance. Further structural engineering of the PFA with these properties may then enable laser-induced graphenization of the precursor.

Acknowledgements

I would like to thank my supervisor, Professor Rodney Smith, for his constant support and encouragement throughout my degree. I am grateful that his door was always open, because his advice and attitudes towards science and life will always stay with me.

I would also like to thank Professor Michael Pope, a member of my committee, for allowing me access to his laboratory's instruments which were crucial for this work. I would like to thank Professor Holger Kleinke as well for his time as a committee member.

This degree would not have been possible without the unwavering support I have received from all our group members, past and present. I am so grateful for Dr. Holly Fruehwald, who is the reason why I pursued graduate studies in the first place and who inspires me daily with her passion and drive. Úna Hogan, Jixi Zhang, Xinran Liu, Jordan Lau, and Dr. Christophe Coudercy also provided much needed support and companionship, particularly during difficult times, and I am eternally grateful to have met such amazing people.

Finally, I am so thankful to my family, whom I know stand behind me every step of the way. They remind me that there is more to life. I hope I can make them proud.

Table of Contents

Author's Declaration ii
Abstract iii
Acknowledgements iv
List of Figures vii
List of Tables xii
List of Abbreviations xiii
List of Schemes xiv
Chapter 1 Introduction 1
1.1 Laser-Induced Graphene 1
1.2 Previous Work Using Poly(furfuryl alcohol) as a Substrate for LIG 3
1.3 Nature of Poly(furfuryl alcohol) 5
1.4 Carbonization of PFA 6
1.5 Thesis Motivation and Overview 8
Chapter 2 Methodology 10
2.1 Materials 10
2.2 PFA Synthesis 10
2.2.1 Varied Acid Concentration (PFA/acid concentration) 10
2.2.2 Varied Solvent (PFA/solvent) 11
2.2.3 Varied 1-Alkanols (PFA/alkanol) 11
2.3 PFA Characterization 12
2.3.1 Fourier Transform Infrared Spectroscopy (FT-IR) 12
2.3.2 Swell Test 12
2.3.3 Thermogravimetric Analysis (TGA) 14
2.4 PFA Substrate Lasing 14
2.5 LIC Characterization 14
2.5.1 Raman Spectroscopy 14
2.5.2 Environmental Scanning Electron Microscopy (ESEM) 15
Chapter 3 Structural Modification via Varied Reaction Conditions 16
3.1 Tuning the Degree of FA Polymerization 16
3.1.1 Introduction 16

3.1.2 Characterization and Discussion 17
3.2 Promoting Furan Ring Opening in PFA 24
3.2.1 Introduction 24
3.2.2 Characterization and Discussion 26
3.3 Steric Effects During Polymerization 34
3.3.1 Introduction 34
3.3.2 Characterization and Discussion 34
3.4 Conclusion 41
Chapter 4 Structurally Varied PFA as Substrates for Laser-Induced Carbonization 43
4.1 Introduction 43
4.2 LIC on PFA with Varied Acid Concentration 46
4.3 LIC on PFA with Varied Solvent 52
4.4 LIC on PFA with Varied Alkanols 58
4.5 Discussion 65
4.6 Conclusion 68
Chapter 5 Conclusions and Future Work 69
5.1 Conclusions 69
5.2 Future Work 69
References 71
Appendix A 78

List of Figures

Figure 1.1. Graphene, a 2D monolayer sheet that can be used to form other carbon materials of other dimensions. Reproduced with permission from Springer Nature.[5] 1
Figure 1.2. Characterization of LIG formed on Kapton using a CO_2 IR laser. Reproduced with permission from Springer Nature.[15] 2
Figure 1.3. Optical images of pristine PFA and PFA with 1% GO after lasing. (a) Ablation of pristine PFA by laser irradiation. (b) Carbonization of PFA/1% GO after laser irradiation. Reproduced with permission from American Chemical Society.[26] 4
Figure 1.4. Raman spectra of LIC formed on PFA precursors. (a) LIC on pristine PFA, (b) LIC on PFA/10% Na2SO4 formed by varied laser powers. Reproduced with permission American Chemical Society.[27] 5
Figure 1.5. Possible structural motifs observed in the PFA backbone as a result of side reactions. 6
Figure 1.6. SEM images of PFA prepared with different acid catalysts after pyrolysis at 600°C. Reproduced with permission from Springer Nature.[53] 7
Figure 1.7. Evolution of the Raman spectra of GC on PFA heat treated from 600-2500°C. Reproduced from Jurkiewicz et al.[52] under the terms of the Creative Commons License (http://creativecommons.org/licenses/by/4.0/). 8
Figure 2.1. Swelling of a crosslinked polymer, depicted with bridges between chains, in the presence of solvent. 13
Figure 3.1. FT-IR characterization of PFA samples prepared with varying acid catalyst concentrations. (a) FT-IR spectra of FA monomer and PFA samples. (b) Trend in absorbances for the C-H wagging mode (1014 cm^{-1}), the C=C stretching mode (1560 cm^{-1}), and ketone groups (1715 cm^{-1}) in PFA as a function of acid concentration. (c) Correlation of residue FA monomer to the degree of polymerization indicated by intensity of the band at 1014 cm^{-1}, showing increased conversion of monomer to PFA. 18
Figure 3.2. Swell ratios of the PFA/acid concentration series. 20
Figure 3.3. TGA analysis of PFA samples prepared with varying amounts of oxalic acid catalyst. (a) TGA (solid lines) and DTG (dashed lines) graphs of each PFA sample. Key parameters are labelled, including onset temperatures for 5% decomposition temperature ($T_{5\%}$), mass loss events (T_{onset}), and peaks in the DTG curves (T_{infl}). (b) Temperatures at which 5% mass loss is observed for each sample. (c) Residue at 800°C as a function of acid concentration. (d) Onset temperatures and peaks of the DTG curves for the first two mass loss events as a function of acid concentration. 22
Figure 3.4. Structure-property correlations across all PFA characterization techniques. (a) Thermal stability metrics, residue at 800°C and $T_{5\%}$, as a function of FT-IR absorbances of the 1014, 1560, and 1715 cm^{-1} peaks. (b) Absorbances of the same FT-IR peaks and (c) thermal stability metrics as a function of swell ratios. 23

Figure 3.5. PFA/solvent samples showed distinct differences in colour and viscosity after 30 minutes of mixing. From left to right: PFA/no solvent, PFA/water, PFA/ethanol, and PFA/acetone. 27
Figure 3.6. PFA/solvent samples post-curing. Clockwise starting in the top left: PFA/no solvent, PFA/water, PFA/acetone, and PFA/ethanol. 27
Figure 3.7. FT-IR characterization of PFA samples prepared in various solvents. (a) FT-IR spectra of PFA/no solvent, PFA/water, PFA/ethanol, and PFA/acetone. (b) Absorbances for the 1014, 1560, 1680 and 1715 cm^{-1} peaks as a function of polymerization solvent. (c) Similarity of solvent solubility parameter to solubility parameter of FA. Values closer to the dashed line at 0 are more similar to the solubility parameter of FA, indicating good compatibility. (d) I_{1715}/I_{1014} ratio of PFA prepared in various solvents. 29
Figure 3.8. TGA analysis of PFA samples prepared in different solvents. (a) TGA (solid lines) and DTG (dashed lines) graphs of each PFA sample. (b) $T_{5\%}$, (c) residue at 800°C, (d) onset temperatures and peaks of the DTG curves for the first (black) and second (red) mass loss events, and (e) peak of the DTG curve for the third mass loss event as a function of solvent. 32
Figure 3.9. Correlations between structural data from FT-IR and thermal stability metrics from TGA for PFA/solvent series. (a, c) $T_{onset,2}$ and (b, d) residue at 800°C as a function of absorbance for selected bands and I_{1715}/I_{1014}, respectively. 33
Figure 3.10. Image of PFA/alkanol samples during mixing. 35
Figure 3.11. PFA/alkanol samples post-curing on PET. 35
Figure 3.12. Transmission FT-IR analysis of PFA prepared with various long chain alcohols. (a) Normalized FT-IR spectra for the PFA/alcohol series, including PFA prepared with the same synthesis without alcohol. New peaks are marked by a dashed line. (b) Changes in the absorbances of selected bands as a function of alcohol chain length. 37
Figure 3.13. Average swell ratios of the PFA/alcohol samples. 37
Figure 3.14. TGA analysis of PFA samples prepared with various alcohols. (a) TGA (solid lines) and DTG (dashed lines) graphs of each PFA sample. (b) $T_{5\%}$, (c) residue at 800°C, and (d) onset temperatures and peaks of the DTG curves for the first (black) and second (red) mass loss events as a function of the alcohol chain length. 39
Figure 3.15. Structure-property correlations across all PFA/alcohol characterization techniques. (a) Thermal stability metrics, residue at 800°C and onset temperature of the second mass loss, as a function of FT-IR absorbances of selected peaks. (b) Thermal stability metrics as a function of swell ratio. (c) FT-IR absorbances as a function of swell ratio. 40
Figure 3.16. Thermal stability comparison of PFA prepared with three different syntheses. (a) $T_{5\%}$, (b) residue at 800°C, and (c) $T_{onset,2}$ values measured for all PFA series. 41
Figure 4.1. Raman spectra of exfoliated graphite powder, bulk graphite powder, and glassy carbon. 44
Figure 4.2. Amorphization trajectory of disordered and amorphous carbons. Reproduced with permission from American Physical Society.[85] 45

Figure 4.3. Top-down SEM images of optimal LIC formed by various laser powers on PFA/acid concentration. (a,b) PFA/no solvent (5.0 W), (c,d) PFA/water (5.0 W), (e,f) PFA/ethanol (4.90 W), and (g,h) PFA/acetone (4.95 W). (a,c,e,g) are at 1000x magnification and (b,d,f,h) are at 200x magnification. 46
Figure 4.4. Raman spectra of LIC formed by varied laser powers on PFA/acid concentration. Spectra of LIC on (a) PFA/0.1 M, (b) PFA/0.2 M, (c) PFA/0.3 M, and (d) PFA/0.4 M. 48
Figure 4.5. Raman analysis of LIC on PFA/acid concentration series. (a) Change in I_D/I_G, (b) position of the G band, and (c) FWHM of the D band on PFA as a function of laser power. 49
Figure 4.6. Analysis of the 2D band observed in the Raman spectra of LIC on PFA/acid concentration. (a) Comparison of the 2D band FWHM and I_{2D}/I_G for determination of the optimal laser power for LIC formation on PFA/acid concentration precursors. The optimal laser power where the minimum FWHM and maximum I_{2D}/I_G is observed is shaded in green. Laser powers that did not result in 2D peaks are shaded in grey. (b) Raman spectra of LIC formed by the optimal laser power for each precursor. (c) Narrowing of the 2D band with increasing I_D/I_G for LIC formed by the optimal laser power. 49
Figure 4.7. Raman analysis of the optimized LIC formed on PFA prepared with varied acid concentration. (a) Position of the G band, (b) FWHM of the D peak, (c) I_D/I_G, (d) FWHM of the 2D band, and (e) I_{2D}/I_G of the optimal LIC on each precursor. 50
Figure 4.8. Structure-Raman correlation of the optimal LIC formed on PFA/acid concentration precursors. Changes in the FWHM of the D band, I_D/I_G, I_{2D}/I_G, and FWHM of the 2D band with (a-d) the intensity of the 1014 cm^{-1} band from FT-IR indicating the degree of polymerization, (e-h) swell ratio indicating the crosslinking density, and (i-l) onset temperature of polymer backbone degradation. 52
Figure 4.9. Top-down SEM images of LIC formed on PFA/solvent. (a-c) PFA/no solvent, (d-f) PFA/water, (g-i) PFA/ethanol, and (j-l) PFA/acetone. (a,d,g,j) are at 50x magnification, (b,e,h,k) are at 200x magnification, and (c,f,i,l) are at 600x magnification. 54
Figure 4.10. Raman spectra of LIC formed on (a) PFA/no solvent, (b) PFA/water, (c) PFA/ethanol, and (d) PFA/acetone with various laser powers. 55
Figure 4.11. Raman analysis of LIC formed on PFA/solvent. Changes in (a) position of the G band, (b) FWHM of the D band, and (c) I_D/I_G across a range of laser powers. 56
Figure 4.12. Averaged values of LIC metrics across the full range of laser powers. (a) Position of the G band, (b) FWHM of the D band, and (c) I_D/I_G of LIC on PFA/solvent. Error bars show the standard deviation. 57
Figure 4.13. PFA/solvent structure correlation to LIC properties. Variations in (a-c) the position of the G band, (d-f) FWHM of the D band, and (g-i) I_D/I_G with changes in the PFA structure, including (a,d,g) the intensity of the 1014 cm^{-1} band from FT-IR indicating degree of polymerization, (b,e,h) the onset temperature of the second mass loss event from TGA, and (c,f,i) intensity ratio of the 1715 cm^{-1} and 1014 cm^{-1} bands from FT-IR. 58
Figure 4.14. Top-down SEM images of LIC formed by the optimal laser power on (a-b) PFA/ethanol, (c-d) PFA/propanol, (e-f) PFA/butanol, (g-h) PFA/pentanol, (i-j) PFA/hexanol, (k-

l) PFA/heptanol, and (m-n) PFA/octanol. Images in the top row are at 200x magnification and images in the bottom row are at 1000x magnification. 59
Figure 4.15. Raman spectra of LIC formed on PFA/alkanol at select laser powers. Spectra of LIC from (a) PFA/ethanol, (b) PFA/propanol, (c) PFA/butanol, (d) PFA/pentanol, (e) PFA/hexanol, (f) PFA/heptanol, and (g) PFA/octanol with 1.30-2.45 W laser power. A dotted line at 1600 cm^{-1} shows the shift of the G band with increasing laser power. 60
Figure 4.16. Ordering trajectory of the LIC on PFA/propanol demonstrated by the evolution of the G peak position and I_D/I_G ratio across the range of laser powers. 61
Figure 4.17. Analysis of the 2D band observed in the Raman spectra of the LIC formed on PFA/alcohol precursors to determine the optimal laser power for LIC formation. The laser powers that induced the minimum FWHM of the 2D band and maximum I_{2D}/I_G on (a) PFA/propanol (1.8 W), (b) PFA/butanol (2.2 W), (c) PFA/pentanol (2.25 W), (d) PFA/hexanol (1.95 W), (e) PFA/heptanol (2.0 W), and (f) PFA/octanol (1.85 W) are highlighted in green. Laser powers that did not form 2D peaks are shaded grey. (g) Optimal laser power for LIC formation as a function of the alkanol length used in the precursor synthesis. 62
Figure 4.18. Raman parameters of the optimal LIC formed on each precursor. (a) Position of the G band, (b) FWHM of the D band, (c) I_D/I_G, (d) I_{2D}/I_G, and (e) FWHM of the 2D band of the LIC as a function of the alkanol length. Error bars show the standard deviation of the values from two Raman maps. 63
Figure 4.19. Analysis of Raman data with respect to thermal properties of the PFA/alcohol precursors. Changes in the (a) position of the G peak, (b) FWHM of the D peak, (c) I_D/I_G, and (d) I_{2D}/I_G as a function of $T_{5\%}$ and residue. 64
Figure 4.20. Average Raman parameters of the optimal LIC formed on each PFA series. (a) Average FWHM of the D peak, (b) average position of the G peak, and (c) average I_D/I_G of the optimal LIC of the PFA/acid concentration, PFA/solvent, and PFA/alkanol series. Error bars show the standard deviation. 66
Figure 4.21. Average Raman parameters of the optimal LIC on each PFA series as a function of various PFA structure data. Changes in I_D/I_G and the average position of the G peak as a function of (a-b) the degree of polymerization, (c-d) swell ratio, and (e-f) temperature at which the maximum mass loss is observed during backbone degradation. 67
Figure A.1. Comparison of FT-IR spectra of PFA/ethanol from the PFA/solvent series obtained by the Thermo Fisher Nicolet 6700 and the Thermo Fisher Nexus 670, the latter of which could not capture peaks below 900 cm^{-1}. 78
Figure A.2. Example peak fit of the transmission FT-IR spectra of PFA. Example shown is PFA/butanol. 78
Figure A.3. Lorentzian peak fits of the Raman spectra obtained from the optimal LIC on PFA/acid concentration. 79
Figure A.4. Lorentzian peak fits of the Raman spectra obtained from the optimal LIC on PFA/solvent. 80

Figure A.6. Lorentzian peak fits of the Raman spectra obtained from the optimal LIC on PFA/alkanol. 80
Figure A.5. Raman parameters of the LIC formed from PFA/alkanol as a function of the intensities of the 1014 cm^{-1} and 1715 cm^{-1} bands from FT-IR. 81

List of Tables

Table 2.1. Molar ratios of FA/oxalic acid for PFA/acid concentration. ……..11

Table 2.2. PFA/solvent reaction paraeters and solvent properties at 25°C. ……...11

Table 3.1. Typical peaks observed in FT-IR spectra of PFA. ……19

List of Abbreviations

DTG	Derivative thermogravimetry
ESEM	Environmental scanning electron microscopy
FA	Furfuryl alcohol
FT-IR	Fourier transform infrared spectroscopy
FWHM	Full width at half maximum
GC	Glassy carbon
LIC	Laser-induced carbon
LIG	Laser-induced graphene
PFA	Poly(furfuryl alcohol)
TGA	Thermogravimetric analysis

List of Schemes

Scheme 2.1. Diels-Alder reaction occurring between two PFA chains. ..……..13

Scheme 3.1. Acid-catalyzed condensation reaction of FA to form PFA. Dehydration of an FA monomer forms a carbocation that adds to another monomer, forming the FA dimer. Continued additions of the FA carbocation to oligomers leads to polymerization. .……...16

Scheme 3.2. Reaction mechanism of furan ring opening within the chain in the presence of a nucleophile. ..…….25

Chapter 1

Introduction

1.1 Laser-Induced Graphene

The discovery of graphene in 2004, the first isolated atomic monolayer material, sparked a new field of research in two-dimensional (2D) materials across several disciplines (Figure 1.1).[1–7] Through a simple mechanical exfoliation technique using adhesive tape, researchers were able to make a material with the highest thermal conductivity, electron mobility, and strength observed at the time.[1,8] It was a natural candidate for applications in electronics, optoelectronics, and transistors because of its attractive properties.[8–10] However, its advantage of simple benchtop preparation for small flakes has not scaled well to large-batch synthesis, hindering the commercialization of such applications.[11–13] Major problems arise during industrial production of graphene, including lack of quality control, inconsistent products, and energy intensive processes. Significant efforts have thus been dedicated to the discovery and optimization of scalable synthesis techniques for graphene.[9,11,14]

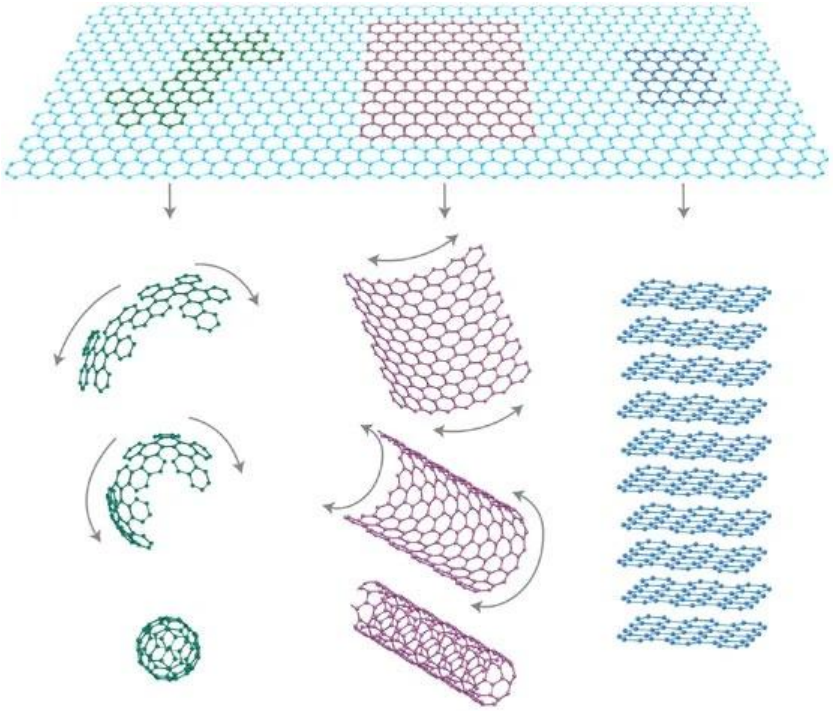


Figure 1.1. Graphene, a 2D monolayer sheet that can be used to form other carbon materials of other dimensions. Reproduced with permission from Springer Nature.[5]

A new technique emerged in 2014 from an experimental error wherein a misaligned CO_2 infrared (IR) laser irradiated a Kapton film instead of the intended embedded graphene oxide target, forming a black material (Figure 1.2).[15,16] Upon further investigation by Raman spectroscopy, they discovered that three-dimensional (3D), porous graphene had been formed. The advantages of this laser-induced graphene (LIG) technique were immediately obvious: a simple, affordable laser setup that could form patternable graphene on flexible substrates at room temperature, opened doors for applications in microsupercapacitors, sensors, and other electronics.[17–20] Control over the resulting LIG's properties was easily achieved by tuning laser parameters such as the power and scanning speed. The precursor was also presumed to influence the LIG, though initial attempts to form the material on 15 other polymers were unsuccessful.

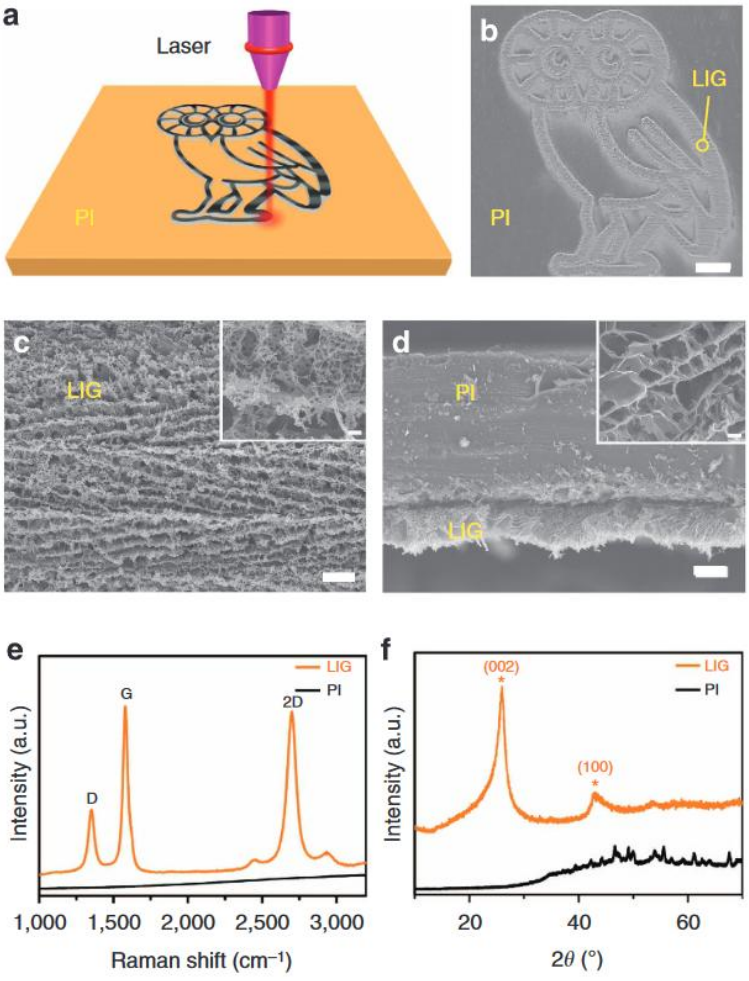


Figure 1.2. Characterization of LIG formed on Kapton using a CO_2 IR laser. Reproduced with permission from Springer Nature.[15]

Further investigation into the mechanism of LIG formation was required to expand the technique to other precursors. With a CO_2 IR laser, photothermal effects dominate the graphitization process; the high, localized temperature induced by the laser breaks the C-O, C=O, and C-H bonds present in the polymer backbone, which releases gaseous products forming the porous LIG structure. The remaining carbon bonds are rearranged into graphene sheets.[15,21] Thus, depending on the chemical composition of the precursor, the porosity, degree of graphitization, and other properties of the LIG will vary.[22]

A comprehensive study regarding the effect of precursor chemistry on LIG formation has not been done despite this promising avenue for LIG tunability. It is known that aromatic units are crucial to LIG formation on polymers, since rearrangement into the graphene structure becomes more efficient. Kapton and poly(etherimide) were the original polymers on which LIG could form, both of which contain repeating aromatic and imide units.[15] It is also imperative for LIG precursors to be highly thermally resistant so they can withstand the temperatures induced by the laser, and so aromatic precursors are inherently suited.[23] Later, however, polysulfones containing only aromatic units were shown to be suitable precursors, as well as sulfonated poly(ether ether ketone) which did not originally form LIG.[17,24] Development of lasing techniques such as multiple lasing and laser defocusing also enabled LIG to form even on aliphatic precursors.[25] Further investigation of LIG formation on a variety of precursors with different chemistry is thus essential for a clearer understanding of its influence on the resulting product.

1.2 Previous Work Using Poly(furfuryl alcohol) as a Substrate for LIG

Initial attempts to form LIG on pristine poly(furfuryl alcohol) (PFA) were made by Hawes et al. in 2019 to no avail.[26] Despite testing a broad range of laser powers and the multiple lasing and laser defocusing strategies that have been shown to successfully carbonize precursors that initially would not form LIG,[25] pristine PFA only ablated under all laser conditions. However, the addition of a 1% graphene oxide (GO) dispersion to the PFA resin immediately enabled carbonization and the subsequent fabrication of microsupercapacitors with comparable performance to those made with LIG from Kapton (Figure 1.3).[26] Various reasons for this transformation were explored, including GO's role as a flame retardant on the polymer and in changing the thermal stability of the PFA, though a single mechanism could not be isolated.

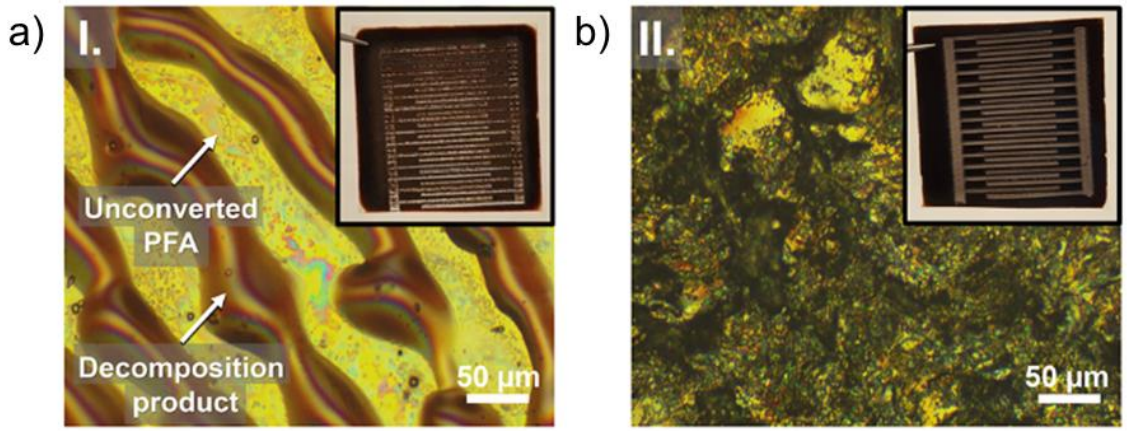


Figure 1.3. Optical images of pristine PFA and PFA with 1% GO after lasing. (a) Ablation of pristine PFA by laser irradiation. (b) Carbonization of PFA/1% GO after laser irradiation. Reproduced with permission from American Chemical Society.[26]

A few years later, Hawes et al. reported the successful laser-induced carbonization of pristine PFA, along with salt-doped PFA (Figure 1.4).[27] With similar lasing conditions, it was clear that there was a difference in the precursor itself that caused this discrepancy. The main reason for this would lie in the difference in preparation of the PFA between works: previously, PFA was polymerized without solvent, whereas ethanol was added in the newer study. Though the change is minor, the synthesis of PFA is known to be complex and sensitive to reaction conditions such as solvent, reaction time, temperature, and nature of the acid catalyst.[28–31] The resulting structure and properties of PFA are thus unpredictable, which complicates its use as a precursor for LIG but also allows for the investigation of the influence of certain structural motifs on LIG formation by varying reaction conditions.

It is prudent to note that when PFA is used as the substrate for laser-induced carbonization, the resulting carbon material is not graphene but is instead more akin to glassy carbon. This distinction governs the metrics by which the quality of the laser-induced carbon is assessed. For accuracy, the carbonaceous material formed on the PFA substrate upon lasing will hereby be referred to as “laser-induced carbon” (LIC) instead of LIG.

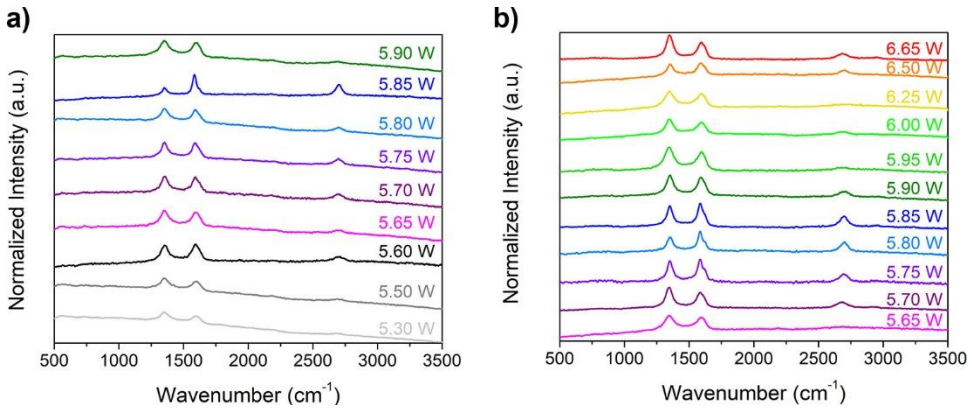


Figure 1.4. Raman spectra of LIC formed on PFA precursors. (a) LIC on pristine PFA, (b) LIC on PFA/10% Na2SO4 formed by varied laser powers. Reproduced with permission American Chemical Society.[27]

Since the scope of polymer precursors enabling LIG formation has been broadened, more focused efforts have been placed on exploring sustainable sources for LIG. Existing LIG precursors such as Kapton and poly(ether ether ketone) are derived from toxic precursors or are energy intensive to produce.[32,33] Though bio-based precursors like wood and lignin can enable LIG formation, their properties are not comparable to that formed from Kapton.[25,34,35] Since previous work has shown that LIC formed from PFA with additives can outperform that on Kapton, it is of interest to investigate whether pristine PFA could produce the same LIG to simplify the synthesis.[26,27] PFA is also commonly used as a precursor for pyrolytic glassy carbon due its high carbon yield and ease of preparation.[36–38] As a result, PFA was chosen as the focus of this work.

1.3 Nature of Poly(furfuryl alcohol)

Poly(furfuryl alcohol) is a thermoset polymer that has been broadly studied since the 20th century.[39–41] Thermoset polymers are distinguished by the unique characteristic of being irreversibly thermally cured, wherein the resulting solid material cannot be turned back into its original liquid form regardless of heating temperature. During the cure, covalent bonds are formed between polymer chains, leading to a crosslinked network which lends thermosetting polymers their high thermal resistance and inertness to harsh solvents.[41] Other commonly used thermosets include phenolic and epoxy resins. They are used extensively as coatings, membranes, and in a variety of other industrial applications.[42–46].

Its monomer, colourless furfuryl alcohol (FA), polymerizes via condensation in the presence of an acid catalyst to theoretically form a linear chain with the furan ring as the repeating unit. However, early studies on the polymerization reaction captured unexpected behaviour, such as the mixture's gradual conversion to a dark brown colour as it increased in viscosity.[47] Since the repeating unit would not form a chromophore, the origin of this colour was initially unclear. Continued investigation into the polymerization reaction revealed several side reactions that occur concurrently to the main polycondensation, both forming small molecular byproducts and modifying the polymer backbone. The PFA backbone is thus comprised of several structural motifs aside from the saturated furan ring, including conjugation across furan rings, ring-opened ketones, and crosslinking from Diels-Alder reactions (Figure 1.5).[39,40,48–50]

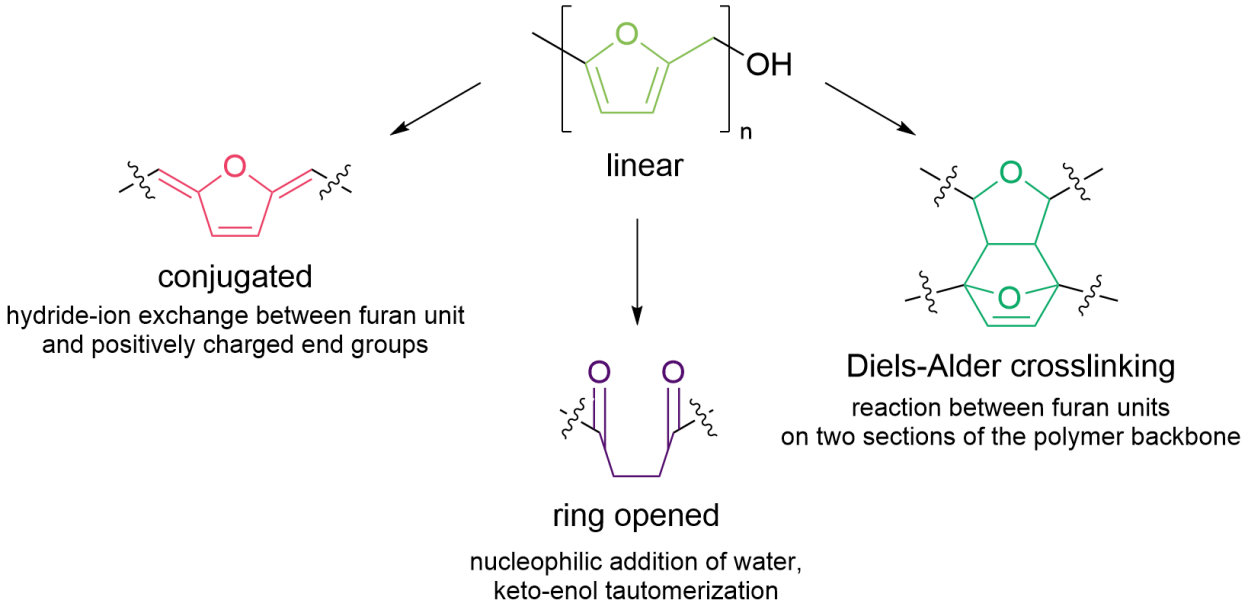


Figure 1.5. Possible structural motifs observed in the PFA backbone as a result of side reactions.

1.4 Carbonization of PFA

The pyrolysis of PFA to form glassy carbon (GC) was first reported in 1969 by Fitzer et al. and has since become the conventional option for its production.[37] PFA is heated at temperatures between 600-2500°C to generate a glasslike carbon (Figure 1.6). Similar to LIC, the precursor chemistry and processing parameters such as heat treatment temperature have a significant influence on the resulting structure of GC. There have thus been extensive studies comparing the quality of GC on PFA pyrolyzed at different temperatures, though less so with varied syntheses of

PFA itself.[51–56] These works are analogous to the research described in this thesis since laser irradiation of PFA similarly induces the high temperatures as in pyrolysis, though on a much shorter timescale. However, the observed evolution of the resulting GC structure and their interpretations can still be used as a framework for the assessment of the LIC formed on PFA.

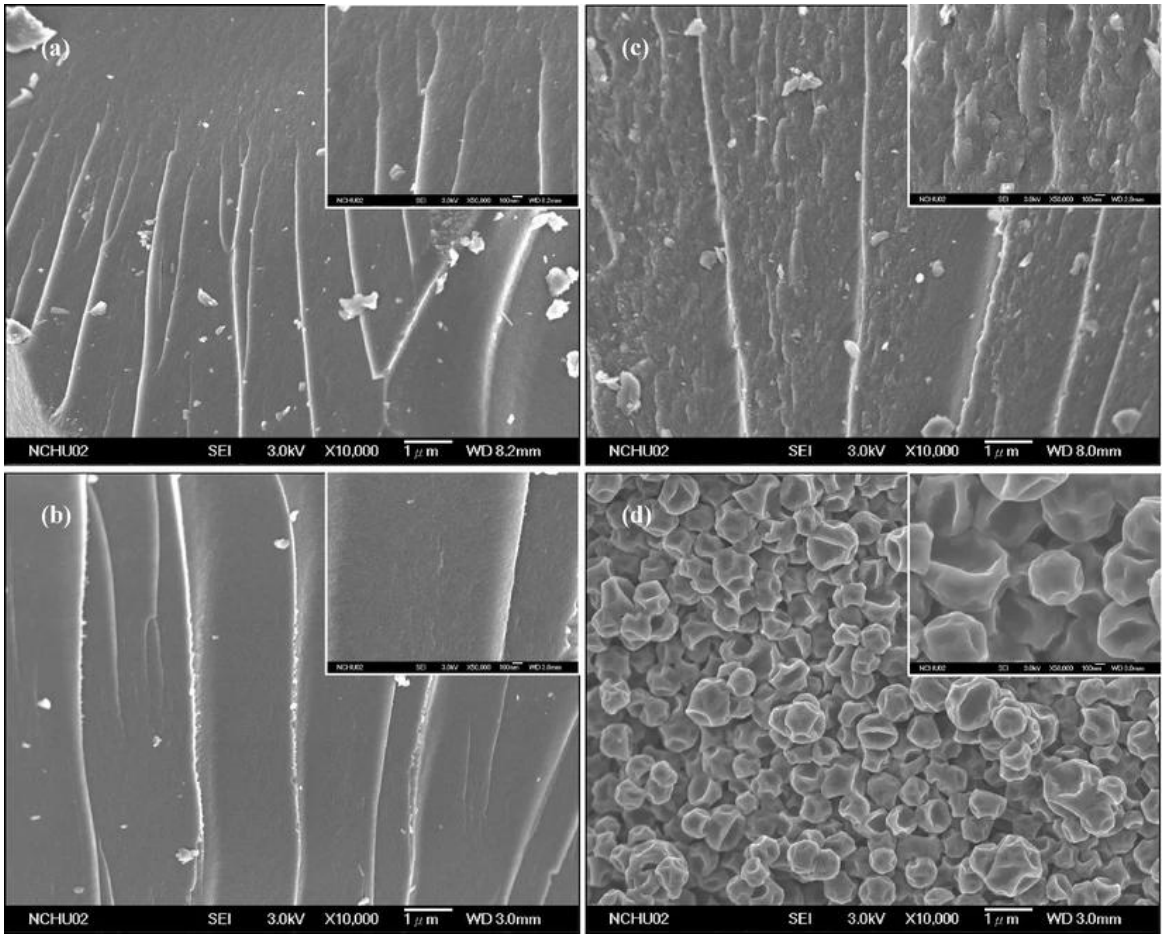


Figure 1.6. SEM images of PFA prepared with different acid catalysts after pyrolysis at 600°C. Reproduced with permission from Springer Nature.[53]

After their initial study on the pyrolysis of PFA, Fitzer et al. immediately investigated the effect of PFA crosslinking on the resulting quantity and porosity of GC formed.[54] They found that the crosslinking did not have a significant effect on the micropore structure and mechanical strength of GC. Following this, several works explored the influence of increasing heat treatment temperatures. Nakamizo et al. performed a comprehensive Raman analysis of various carbon materials, including GC prepared on PFA, and observed significant peak narrowing when the PFA was treated at 2000°C compared to that at 500°C.[56] A more detailed study by Jurkiewicz et al.

confirmed this behaviour, and further showed that the mechanical strength of GC formed on PFA peaked when treated at 1000°C, then decreased at higher temperatures at the cost of the formation of more ordered, graphitic domains in the carbon structure (Figure 1.7).[52] The Raman spectra of carbon materials are discussed in further detail in Chapter 4. Aside from heat treatment parameters, Cheng and Tseng investigated both the effect of acid catalyst type on the PFA structure and resulting GC and found that the catalysts promoted polymerization in PFA, resulting in a less defected and more ordered carbon structure.[53] Such investigations provide insight on how lasing parameters like laser power affect the LIC formed from PFA.

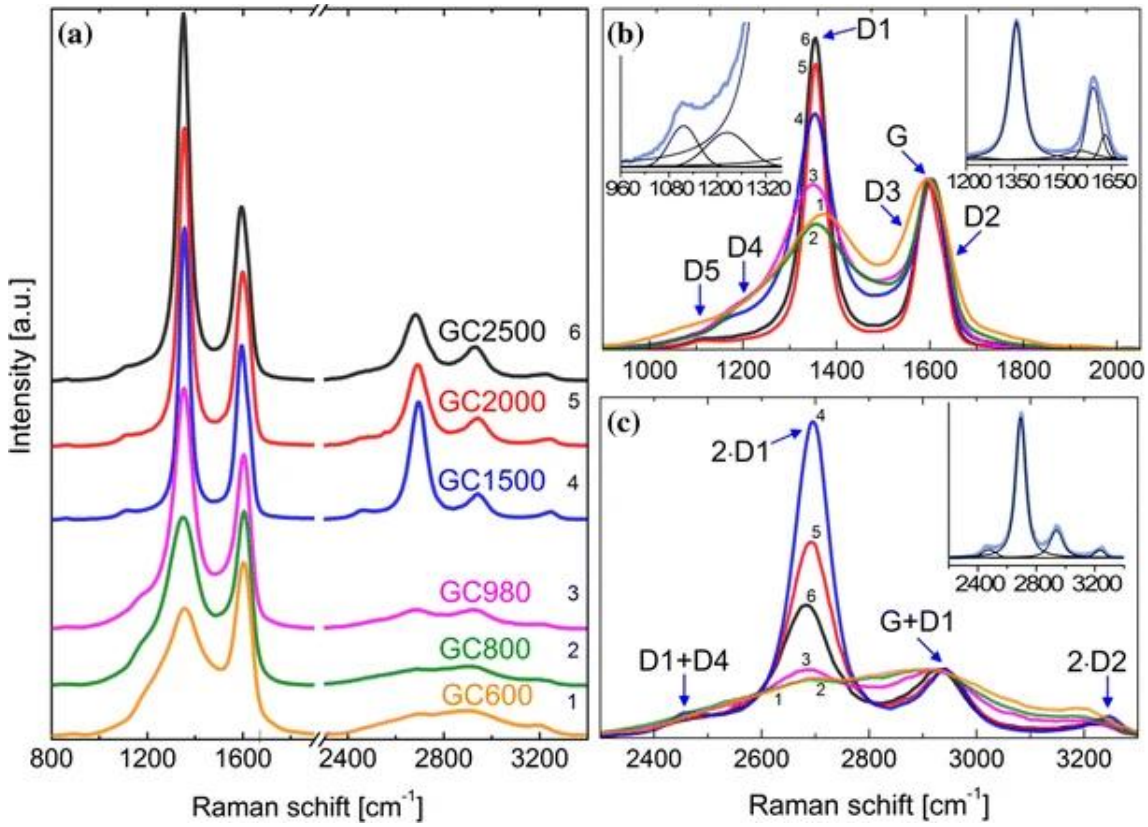


Figure 1.7. Evolution of the Raman spectra of GC on PFA heat treated from 600-2500°C. Reproduced from Jurkiewicz et al.[52] under the terms of the Creative Commons License (http://creativecommons.org/licenses/by/4.0/).

1.5 Thesis Motivation and Overview

Varied reaction conditions will result in an array of structural variation in PFA, which can be expected to directly impact the thermal and mechanical properties of the polymer. A degree of control over the PFA structure and resulting properties can thus be exerted if certain side reactions

are targeted. This enables PFA to be a playground on which to test the influence of chemical structure and properties on LIG formation with simple changes to the synthetic procedure.

This work explores PFA as a viable substrate for laser-induced carbonization by investigating the effect of various synthetic parameters (acid concentration, solvent, and alcohols as a reagent) on the final structure of the polymer network and its subsequent influence on the LIC quality. **Chapter 2** details the experimental methods used in this work, including the various syntheses, polymer characterization methods, lasing parameters, and LIC analysis. **Chapter 3** describes the synthesis and characterization of the three PFA series and discusses how the polymer structure and properties are affected by the varied synthetic parameter. **Chapter 4** investigates the three series of PFA samples as substrates for laser induced carbonization, primarily using Raman spectroscopy to characterize the formed carbonaceous materials and assess how the varied polymer structures affect their quality. **Chapter 5** summarizes the key findings of this work and discusses possible future directions.

Chapter 2

Methodology

2.1 Materials

Each PFA series was synthesized from FA monomer (98%, Thermo Scientific) and either oxalic acid (99.5%, BDH Chemicals, PFA/acid concentration and PFA/solvent series) or 2.8 M sulfuric acid (98%, Sigma-Aldrich, PFA/alkanol series) was used as the acid catalyst. Milli-Q water, ethanol (certified ACS grade, Greenfield Global Inc.), and acetone (99.5%, Sigma-Aldrich) were used for the PFA/solvent series. Ethanol, 1-propanol (certified grade, Fisher Scientific), 1-butanol (99.5%, Merck), 1-pentanol (99%, Alfa Aesar), 1-hexanol (99%, Alfa Aesar), 1-heptanol (98%, Sigma Aldrich), and 1-octanol (99%, Oakwood Chemical) were used as reactants for the PFA/alcohol series. KBr (certified ACS grade, Fisher Scientific) was used to prepare pellets for transmission FT-IR. All materials were used without further purification.

2.2 PFA Synthesis

A general procedure for polymerizing FA was used for all series with some deviations in quantity and duration, which are detailed in the following sections. FA was mixed with the acid catalyst and reactants and allowed to stir either at room temperature or in a heated oil bath until the mixtures turned an opaque dark brown and reached approximately the same viscosity, indicating that the polymerization had reached a high degree of conversion. Approximately 1 mL of the PFA mixtures were then drop cast onto PET substrates which had been ultrasonicated in ethanol for 10 minutes to remove debris. Films were cast to ~1 mm thickness to prevent the laser from cutting through the substrate. The samples were then cured in an oven at 80°C. To prepare samples for characterization, sections of PFA were peeled off the PET substrate and crushed into finer pieces.

2.2.1 Varied Acid Concentration (PFA/acid concentration)

A mixture of 4 mL of FA, 1 mL of ethanol, and varying molar ratios of FA to oxalic acid (Table 2.1) was added to a glass vial and placed in an 80°C oil bath to stir for 2-5 hours. The films were cured in an oven at 80°C overnight.

Table 2.1. Molar ratios of FA/oxalic acid for PFA/acid concentration.

Sample	Acid Concentration (M)	FA:oxalic acid (mol)
PFA/0.1 M	0.1	166
PFA/0.2 M	0.2	81
PFA/0.3 M	0.3	54
PFA/0.4 M	0.4	40

2.2.2 Varied Solvent (PFA/solvent)

A mixture of 4 mL of FA either without solvent or with 4 mL of ethanol, water, or acetone and an FA:oxalic acid molar ratio of 81 was added to a glass vial. The reaction mixtures were stirred on a hot plate at 80°C for 2-5 hours, which varied for each solvent, while capped for at least one hour to prevent solvent loss by evaporation to allow the solvent time to react with the monomer. The films were cured in an oven at 80°C overnight. Solvent parameters, such as dielectric constant and Hildebrand solubility parameter, varied across the range and allowed the investigation of the influence of solvent polarity and polymer-solvent compatibility (Table 2.2).

Table 2.2. PFA/solvent reaction parameters and solvent properties at 25°C.

Reagent	Reaction Time (h)	Dielectric Constant, $\boldsymbol{\varepsilon}$[57]	Solubility Parameter, δ ($MPa^{1/2}$)[58]
FA	2	-	28.2
Water	3	78.5	47.9
Ethanol	5	24.3	26.0
Acetone	3	20.7	20.3

2.2.3 Varied 1-Alkanols (PFA/alkanol)

Sulfuric acid was used as the catalyst for this reaction to maintain a reasonable reaction time, as steric effects are seen to have significant effects on the rate of reaction[30]. A mixture of 3 mL of FA, 0.15 mL of 2.8 M sulfuric acid, and 1 mL of ethanol, 1-propanol, 1-butanol, 1-pentanol, 1-hexanol, 1-heptanol, or 1-octanol was added to a glass vial. The reaction mixtures were stirred at room temperature for 2 hours while capped for at least one hour to prevent solvent loss by evaporation. Films were cured in an oven at 80°C for 3 hours.

2.3 PFA Characterization

2.3.1 Fourier Transform Infrared Spectroscopy (FT-IR)

The transmission mode on a Thermo Fisher Nexus 670 FT-IR Spectrometer was used to obtain FT-IR spectra for the PFA/acid concentration and PFA/solvent series, while a Thermo Fisher Nicolet 6700 FT-IR Spectrometer was used to obtain FT-IR spectra for PFA/alcohols. Instrument failures necessitated the use of two different spectrometers, though measurement parameters remained the same. 128 scans were taken with a 4 cm^{-1} resolution. The Thermo Fisher Nexus spectrometer was unable to capture the peaks expected in the region below 1000 cm^{-1}, and so the spectra in Section 3.1 and 3.2 are presented in the wavenumber range of 4000-900 cm^{-1}, whereas the spectra in Section 3.3 are shown in the range of 4000-550 cm^{-1}. Differences in the FT-IR measurements obtained for the same sample on both spectrometers confirmed this (Figure A.1).

A 13.5 mm diameter pellet, approximately 2 mm thick, was made with 2 mg of sample and 200 mg of oven-dried KBr. All spectra were collected in absorbance mode. Data were exported and processed using Renishaw WiRE 5.5 software to perform baseline subtraction, normalization, and curve fitting operations.

2.3.2 Swell Test

Crosslinking density directly influences the mechanical properties of the polymer, so characterization is crucial. A simple, quantitative method developed by Flory[59] involves measuring the swelling behaviour of a crosslinked polymer in a suitable solvent. When placed in a solvent in which it is soluble, the solvent will enter the crosslinked network, causing the polymer to swell (Figure 2.1). The degree to which the polymer is crosslinked (i.e. the average length of chains between crosslinked junctions) will dictate the extent of swelling.

Crosslinking in PFA is mainly attributed to the Diels-Alder reaction that occurs between a conjugated furan ring acting as the diene and a typical furan unit acting as the dienophile (Scheme 2.1). This reaction occurs after oligomers are formed, leading to the gelation stage at the end of polymerization, and continues during the curing step.[60] The crosslinked motif is thus an inherent feature of the PFA network.

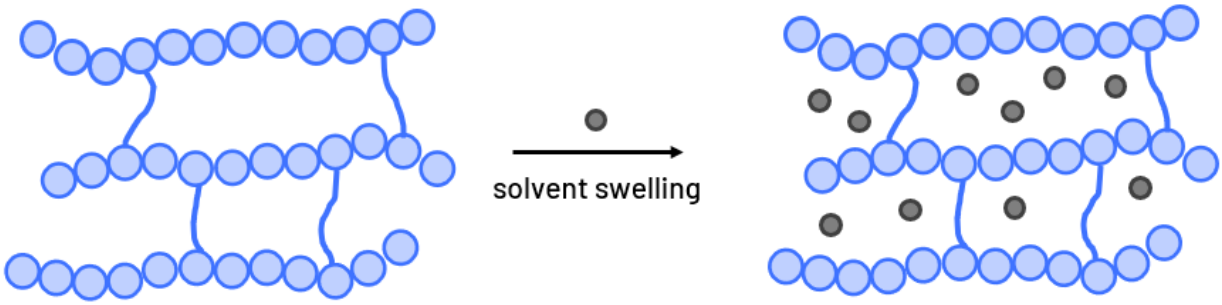
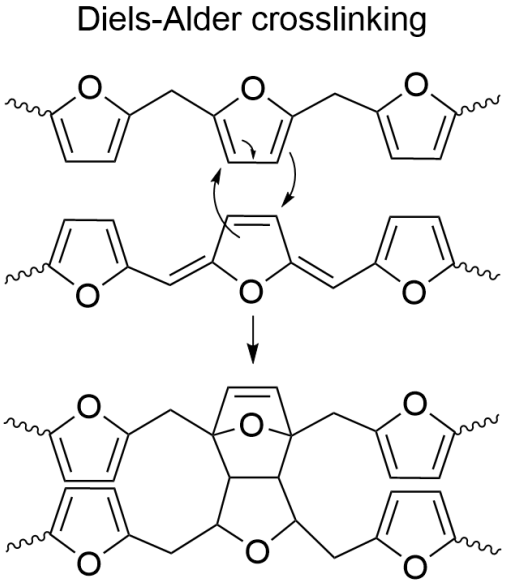


Figure 2.1. Swelling of a crosslinked polymer, depicted with bridges between chains, in the presence of solvent.



Scheme 2.1. Diels-Alder reaction occurring between two PFA chains.

Crushed PFA sample was weighed to obtain the dry mass (W_d) and submerged in water for about 24 hours at room temperature until equilibration.[61] Swelled samples were removed from the solvent and weighed to obtain the sample mass in the swollen state (W_s). The swell ratio, describing the extent of solvent uptake in the polymer, was then determined using Equation 1.[61] A higher swell ratio indicates a lower degree of crosslinking.

$$swell\ ratio = \frac{(W_s - W_d)}{W_d} \quad (1)$$

Ethanol and acetonitrile were also tested as solvents for the swell test, which theoretically are more suitable solvents for the swelling of PFA due to a better match of their solubility

parameters with that of PFA.[61] However, PFA submerged in ethanol for 24+ hours did not exhibit any swelling. Samples immersed in acetonitrile dissolved, resulting in a "swelled" mass that was lower than the original dry mass and thus prevented quantification of crosslinking density with these solvents. As such, water was chosen as the solvent for all swell tests.

2.3.3 Thermogravimetric Analysis (TGA)

A TA Instruments TGA Q500 was used to measure the thermal stability of the PFA samples. Approximately 15 mg of sample was placed in an alumina pan and heated at a ramp rate from 22.5°C to 800°C at a ramp rate of 10°C/min in nitrogen gas flowing at 50 mL/min.

2.4 PFA Substrate Lasing

A BossLaser 1416L 50W CO_2 IR laser machine was used to carbonize the PFA/acid concentration and PFA/solvent precursors in rows of thin 6 mm x 1.5 mm rectangles designed in RDWorks, v8.0. Each rectangle was scribed using a different laser power in the range of 4.75-5.65 W at 0.05 W increments. The PFA/alkanol precursors were scribed with the Thunder Bolt laser cutter from Thunder Laser due to operational issues with the BossLaser cutter that occurred during this work.

The precursors were initially scribed using the same range of laser powers as the previous two PFA series, but the lowest laser power completely charred the precursor despite not even carbonizing the previous precursors. The laser power range was thus lowered to 1.2-2.45 W to scribe the PFA/alcohol precursors, wherein the sequence of no carbonization, carbonization, and ablation was observed. Possible reasons for this discrepancy are discussed briefly in Chapter 5.

2.5 LIC Characterization

2.5.1 Raman Spectroscopy

A Renishaw inVia Reflex Raman microscope and a 532 nm excitation laser with 1800 and 2400 lines/mm gratings were used to perform Raman spectroscopy measurements. For the PFA/acid concentration and PFA/solvent series, a laser power of 1% was used to avoid sample degradation with 10s exposure time. Spectra maps were obtained on two different locations of the LIC, typically within a 4 x 3 μm area, then averaged to obtain a representative spectrum of the entire scribed rectangle. Spectra were measured with the extended range of 100-3200 cm^{-1} to capture all Raman peaks that are known to appear in the spectra of carbonaceous materials. For the

PFA/alkanol series, the spectra were centred at 2070 cm^{-1} and taken with 1s exposure time. Data were processed using Renishaw WiRE 5.5 software to perform map averaging, cosmic ray removal, baseline subtraction, and normalization. Lorentzian peak fitting was performed using a Python script.

2.5.2 Environmental Scanning Electron Microscopy (ESEM)

A Quanta FEG-250 environmental scanning electron microscope was used to image the morphology of the LIC under high vacuum. Images were taken at 50x, 100x, 600x, and 1000x magnification on several locations of the LIC.

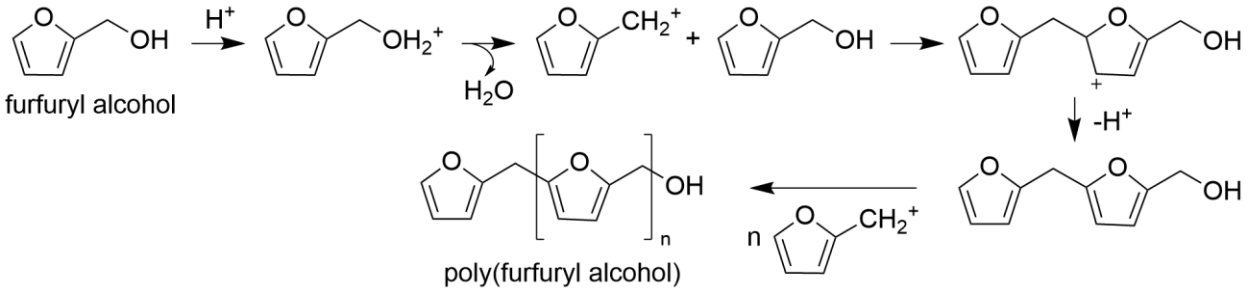
Chapter 3

Structural Modification of PFA via Varied Reaction Conditions

3.1 Tuning the Degree of FA Polymerization

3.1.1 Introduction

The condensation reaction driving FA polymerization requires an acid catalyst, which initiates the reaction through protonation of the hydroxyl group on an FA monomer (Scheme 3.1). The influence of the acid catalyst identity and concentration on the polymerization has been studied extensively. Several categories of acids have proven effective in FA polymerization, including organic acids such as oxalic acid, maleic acid, or p-toluenesulfonic acid,[26,28,39,62,63] mineral acids such as H_2SO_4, HCl, or HNO_3,[31,40,49,53,64] and Lewis acids such as $SnCl_4$, $TiCl_4$, or $ZnCl_2$.[39,48,65] The effect of increasing the monomer to acid catalyst ratio on both the polymerization and subsequent curing step was also studied in several works.[39,48,61,64]



Scheme 3.1. Acid-catalyzed condensation reaction of FA to form PFA. Dehydration of an FA monomer forms a carbocation that adds to another monomer, forming the FA dimer. Continued additions of the FA carbocation to oligomers leads to polymerization.

Increasing the acid catalyst concentration increases the rate of polymerization, though it remains unclear exactly how the resulting polymer structure is altered due to simultaneous side reactions whose kinetics are also affected by acid catalysts. Previous work showed that increasing the acid concentration resulted in a more viscous PFA resin, hinting at a higher degree of polymerization prior to curing.[48] Increased acid concentration can also increase the cross-linking density of the cured polymer when added prior to curing.[61] However, a 'limit' for the monomer to acid catalyst ratio was observed, wherein decreasing the ratio beyond this limit no longer has an appreciable effect on the polymer structure.[61,64] These works demonstrate that, despite the side

reactions contributing to PFA's structural complexity, increasing the acid concentration for polymerization will cause systematic changes. The extent of reaction and therefore the degree of polymerization can thus be tuned by varying the ratio of monomer to acid catalyst, and such changes will influence the polymer's structure and physical properties.

Herein, a series of PFA samples is synthesized with varied monomer to oxalic acid ratios and the effect of acid concentration on the final polymer is analyzed. Changes in the degree of polymerization were examined by tracking absorbance changes in the FT-IR spectra as a function of acid catalyst concentration. Oxalic acid is selected for its weak acidity, permitting a slower and more controlled polymerization. Absorbance increases in key vibrational bands such as the C-H wag of the furan unit revealed a greater extent of polymerization with higher acid concentration, supported by TGA measurements that showed corresponding increased thermal stability.

3.1.2 Characterization and Discussion

Transmission FT-IR spectra of the FA monomer and PFA/acid concentration samples show how PFA differs from FA and how the polymerized structure evolves as a function of acid concentration (Figure 3.1a). The peaks observed in these spectra are typical of PFA, regardless of synthetic conditions, and the assignments are summarized in Table 3.1. Polymerized FA exhibits several variations in the FT-IR spectrum compared to the monomer, particularly in the 1800-900 cm^{-1} range. The most intense peak, observed at 1014 cm^{-1}, is assigned as a C-H wagging mode on the furan rings.[49] This peak is unique to the polymer and indicates the degree of polymerization.[66,67] The series of bands between 1100 and 1280 cm^{-1} is attributed to various asymmetric and symmetric C-O vibrations in the furan ring.[31,49] The peak at 1505 cm^{-1} arises from the C=C stretch of an end group or monomer furan unit, whereas a new peak in the PFA spectra observed at 1560 cm^{-1} is assigned to the C=C stretch of 2,5-substituted furan (i.e. furan within the polymer chain).[50] The ring-opening side reaction results in the formation of ketone motifs within the structure, whose C=O stretch yields a peak at 1715 cm^{-1}.[66] Combinations of the ring-opened and conjugated motifs result in two other peaks appearing at 1610 and 1680 cm^{-1}, attributed to C=C stretches vicinal to the ketone and a conjugated C=O stretch, respectively.[49] These features will be discussed further in Section 3.2. The band at 1760 cm^{-1} is assigned to the C=O bond of an ester, such as ethyl levulinate.[66,68] Peaks observed between 3000-2800 cm^{-1} and between 3200-3000 cm^{-1} are assigned to the sp^2 and sp^3 C-H bonds in the backbone, respectively. The broad peak spanning 3400-3200

cm^{-1} is attributed to the hydroxyl group on the monomer and is less intense in the PFA spectra than that of FA, indicating a lower degree of residual monomer in the polymers.[50] The disappearance of the strong band at 915 cm^{-1} (furan C=C bend) from the PFA spectra, which was originally observed in the FA spectrum, further corroborates that polymers contain negligible amounts of residual monomer.[53]

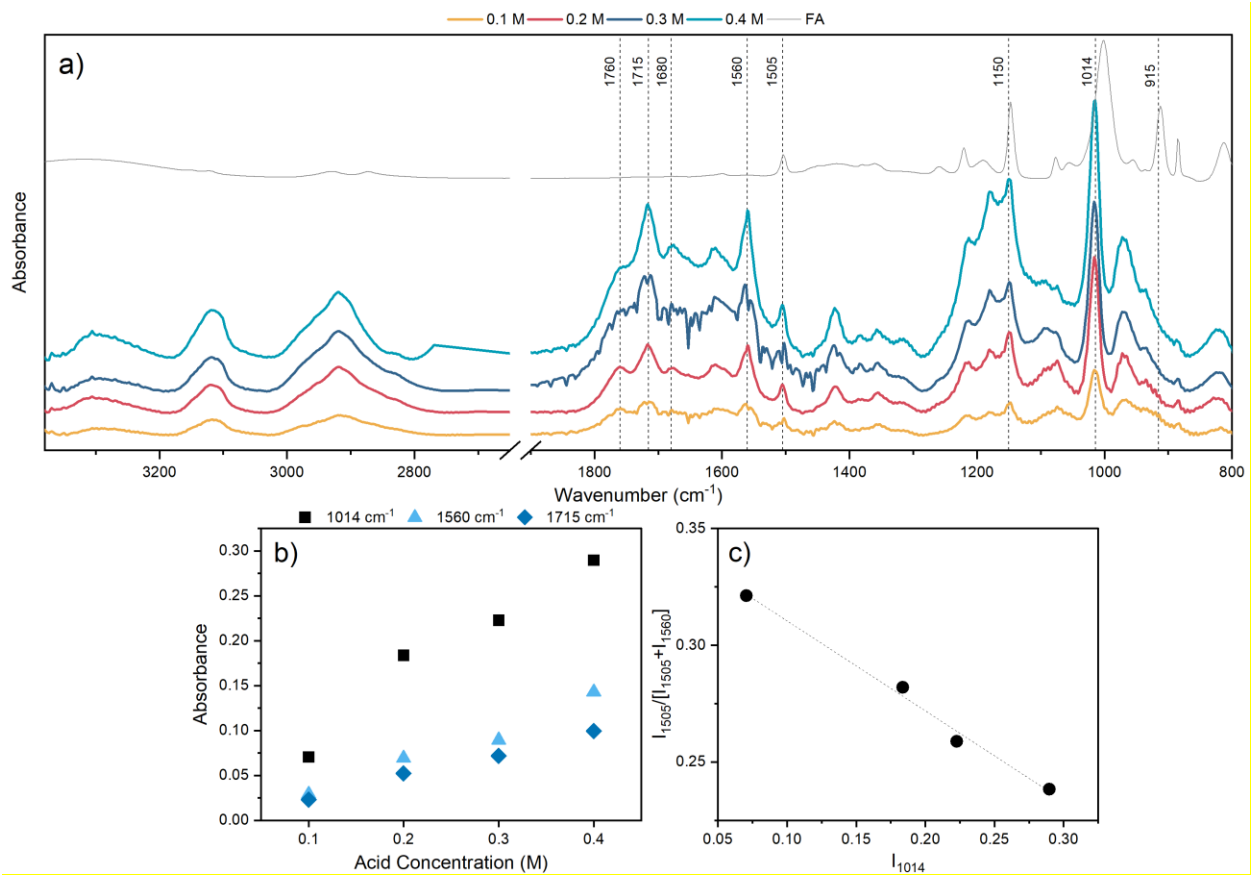


Figure 3.1. FT-IR characterization of PFA samples prepared with varying acid catalyst concentrations. (a) FT-IR spectra of FA monomer and PFA samples. (b) Trend in absorbances for the C-H wagging mode (1014 cm^{-1}), the C=C stretching mode (1560 cm^{-1}), and ketone groups (1715 cm^{-1}) in PFA as a function of acid concentration. (c) Correlation of residue FA monomer to the degree of polymerization indicated by intensity of the band at 1014 cm^{-1}, showing increased conversion of monomer to PFA.

Changes in the FT-IR peak absorbances were investigated to compare structural differences between the PFA samples with varying acid concentrations. The peak fitted absorbances of significant bands in the spectra (Figure A.2), including the 1014 cm^{-1} band, increased with increasing acid concentration (Figure 3.1b). PFA/0.4 M had a nearly threefold increase in the absorbance of the 1014 cm^{-1} peak compared to PFA/0.1 M, indicating a significantly higher degree

of polymerization. This finding is supported by increases in the absorbance of the C=C stretch from the 2,5-substituted furan indicating more polymerized furan units. While the amount of residual monomer increases in the samples with higher acid concentration (indicated by the band at 1505 cm^{-1}), the changes are minimal and are outpaced by the evolution of the polymerized furans. The fraction of residual monomer in PFA is determined by Eq. 2 utilizing the two C=C bands from free (I_{1505}) or end group (I_{1560}) furan units and oligomeric furan units. Increased degree of polymerization (i.e. absorbance of the 1014 cm^{-1} band) should correspond to a lower fraction of residual monomer. A linear, decreasing slope is yielded when plotted against the degree of polymerization, which further confirms that FA polymerized with higher acid concentration results in higher conversion (Figure 3.1c).

Table 3.1. Typical peaks observed in FT-IR spectra of PFA.

Wavenumber (cm^{-1})	**Bond**	**Assignment**[31,38,49,50,66]
1014	C-H	Furan in-plane wag
1150	C-O	Furan vibration
1380	C-H	Terminal methyl group bend
1505	C=C	Furan stretch (free or end group)
1560	C=C	Furan stretch in oligomer or conjugated diene
1610	C=C	Vicinal to ketone
1680	C=O	Conjugated ketone
1715	C=O	Ketone after furan ring opening
1760	C=O	Carboxylic acid from small molecules
3000-2800	C-H	Aliphatic C-H
3200-3000	C-H	Aromatic C-H
3600-3300	O-H	Broad, hydroxyl end groups or residual FA monomer

$$Fraction\ of\ residual\ FA = \frac{I_{1505}}{I_{1505} + I_{1560}} \quad (2)$$

Aside from functional groups and bond types in the backbone, crosslinking is also an essential feature in PFA's structure as a thermoset polymer. Swell tests in solvent allow the quantitative determination of the crosslinking density, which reveals insight on the effect of acid catalyst concentration on the curing stage of PFA synthesis. The PFA samples with higher acid concentration swelled to a greater extent in water, suggesting that the crosslinking density of the samples decreases when more acid catalyst is present (Figure 3.2). This is an unexpected result, as it has been demonstrated previously that the acid concentration has the opposite effect on the degree of crosslinking.[29,61] However, the previous studies performed a second addition of acid catalyst prior to the curing step after resinification, which allows direct examination of the acid concentration's effect on crosslinking. In this synthesis, the same amount of acid catalyst is present during both polymerization and curing, so the effect of the acid concentration on side reactions before curing makes it difficult to deconvolute its influence on crosslinking during the cure. Despite the relatively large uncertainty that is inherent in these measurements, the results indicate a lower degree of crosslinking in the cured PFA samples when higher acid concentrations are used.

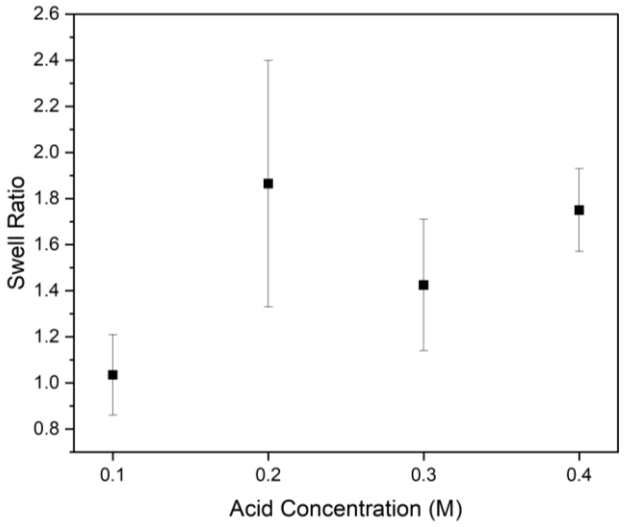


Figure 3.2. Swell ratios of the PFA/acid concentration series. Error bars show the standard deviation.

The thermal stability of all PFA sample series was investigated by TGA in inert atmosphere to support the structural analysis from FT-IR, as the two aspects are closely intertwined. Thermally-induced mass loss provides insight on the PFA samples' thermal resistance and decomposition pathways, which reveals specific aspects of the polymer structure. A common

metric to assess thermal stability of polymers is the temperature at which 5% weight loss is observed ($T_{5\%}$), where a higher temperature indicates better thermal resistance.[66] The residue at 800°C is the weight percentage of the sample that remains after the heating, also referred to as carbon yield. This metric reveals the overall mass loss experienced by the sample and so a higher residue indicates that the sample is more resistant to thermal decomposition.

The TGA and derivative thermogravimetry (DTG) curves show that the PFA samples with lower acid concentration have different thermal decomposition profiles (Figure 3.3a). Each of the graphs exhibits three weight loss events that are readily shown by the DTG curves. The first weight loss begins above 100°C for all PFA and exhibits a maximum rate of loss between 170-190°C. This event corresponds to the removal of residual ethanol, unreacted monomer, and free water.[28,64] The second weight loss begins after 300°C with the maximum rate of mass loss at ca. 360°C and is attributed to the release of CO, CO_2, or H_2O.[54,64] At these temperatures, the furan ring structure is degraded.[54] Since the matrices of the polymers differ in this work, resulting in varied mass losses of residual species, the onset and peak temperatures of this event are also used to assess thermal stability. The third and final weight loss event overlaps with the second and yields a peak rate of weight loss at ca. 430°C. A mixture of CH_4, CO, and H_2 are released in this temperature range.[38,66] The temperatures for onset of mass loss (T_{onset}) and maximum rate of mass loss (T_{infl}) for each event, along with $T_{5\%}$ and the total final residues, are evaluated to determine the relative thermal stability of each sample with varying acid concentration.

Quantitative analysis of the data shows that $T_{5\%}$ of PFA/0.1 M is 190°C, nearly 40°C lower than that of PFA/0.2 M, PFA/0.3M, and PFA/0.4 M, which stabilizes around 230°C (Figure 3.3b). The significantly higher rate of mass loss at a lower temperature indicates that the matrix of PFA/0.1 M contained appreciable amounts of residual monomer and thus was polymerized to a much lower extent. The $T_{5\%}$ of the samples with higher acid concentration are all similar, indicating that a comparable degree of conversion is reached by the three samples. Increased acid concentrations also consistently yielded larger residues: at 800°C, the carbon yield of PFA/0.4 M was about 50% while that of PFA/0.1 M was ca. 42% (Figure 3.3c). Lower overall mass loss can be attributed to less free species in the polymer matrix and higher connectivity within the network. The onset and peak temperatures of both mass loss events are also higher with greater acid concentrations, with the onset of the second mass loss PFA/0.4 M beginning at 329°C, and PFA/0.1

M at 317°C (Figure 3.3d). Overall, the TGA data show that the thermal stability of the PFA series increases with acid concentration.

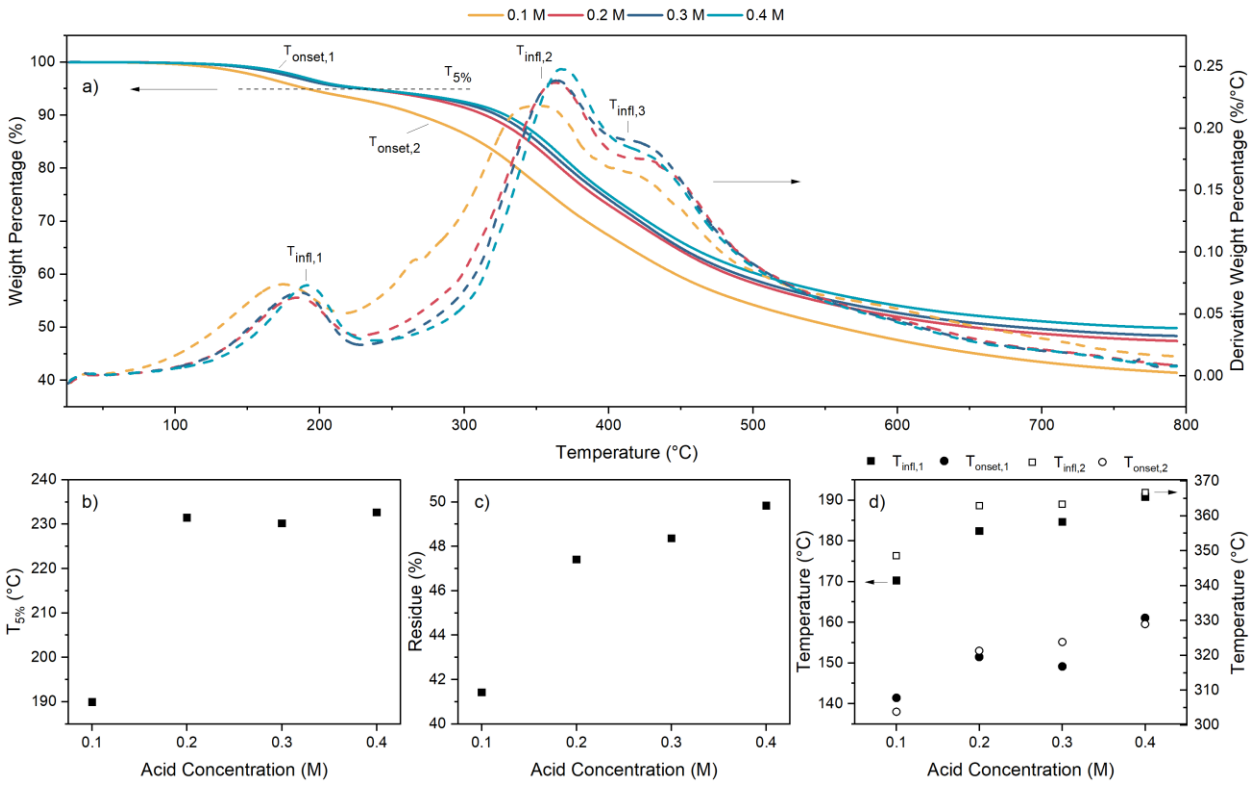


Figure 3.3. TGA analysis of PFA samples prepared with varying amounts of oxalic acid catalyst. (a) TGA (solid lines) and DTG (dashed lines) graphs of each PFA sample. Key parameters are labelled, including onset temperatures for 5% decomposition temperature ($T_{5\%}$), mass loss events (T_{onset}), and peaks in the DTG curves (T_{infl}). (b) Temperatures at which 5% mass loss is observed for each sample. (c) Residue at 800°C as a function of acid concentration. (d) Onset temperatures and peaks of the DTG curves for the first two mass loss events as a function of acid concentration.

The relative thermal stability of the PFA/acid concentration samples can be explained by the structural information obtained from the FT-IR spectra and swell tests. The highest thermal stability of PFA/0.4 M can be correlated to its overall highest degree of polymerization as determined from the FT-IR spectra (Figure 3.4a). Residue at 800°C and $T_{5\%}$ increase as a function of the degree of polymerization, characterized by the C-H wagging band at 1014 cm^{-1} and the polymerized furan C=C band at 1560 cm^{-1}. Since the degree of polymerization implies longer polymer chains and less free species in the matrix, the increased number of covalent bonds lends the sample a higher thermal stability. Analysis of the polymer swell tests showed, however, that a greater degree of polymerization does not necessitate a more branched, crosslinked network

(Figure 3.4b). The PFA with a lower degree of crosslinking exhibited higher thermal stability (Figure 3.4c), implying that structural factors other than crosslinking contribute strongly to PFA's thermal properties. Aromatic structures are known to greatly increase the thermal resistance of polymers, so the higher thermal stability is likely a result of the increased amount of furan rings in the PFA backbone, as indicated by the greater extent of polymerization.[69,70] Overall, the three characterization techniques support the picture that this PFA/acid concentration series encompasses a range of PFA with varied degrees of polymerization.

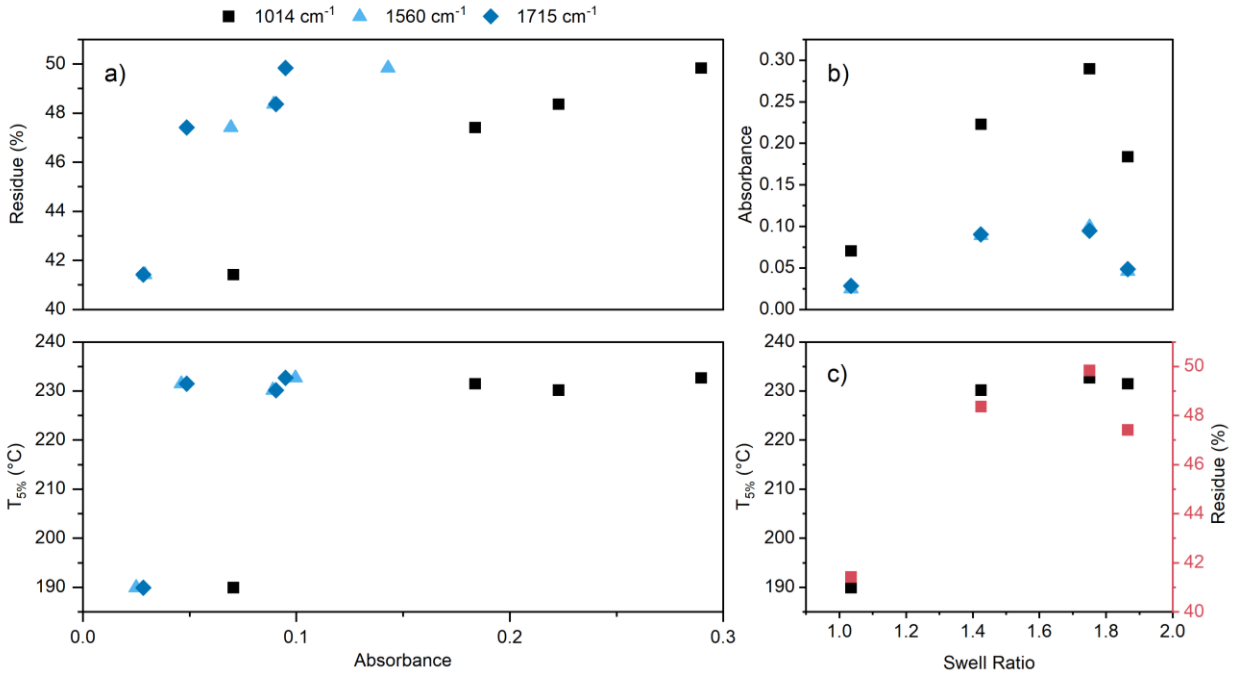


Figure 3.4. Structure-property correlations across all PFA characterization techniques. (a) Thermal stability metrics, residue at 800°C and $T_{5\%}$, as a function of FT-IR absorbances of the 1014, 1560, and 1715 cm^{-1} peaks. (b) Absorbances of the same FT-IR peaks and (c) thermal stability metrics as a function of swell ratios.

This series of PFA samples prepared with varied ratios of FA to oxalic acid catalyst showed that the degree of polymerization can be tuned by adjusting the acid catalyst concentration. Structurally, PFA/0.4 M with the highest acid concentration had a significantly higher degree of polymerization than that of PFA/0.1 M, which indicates a greater amount of furan units in the polymer backbone and thus higher overall aromaticity. Consequently, PFA prepared with higher acid concentration also has a greater thermal stability. This property may be desirable for LIC substrates to avoid decomposition at the extreme temperatures induced by the laser, as less

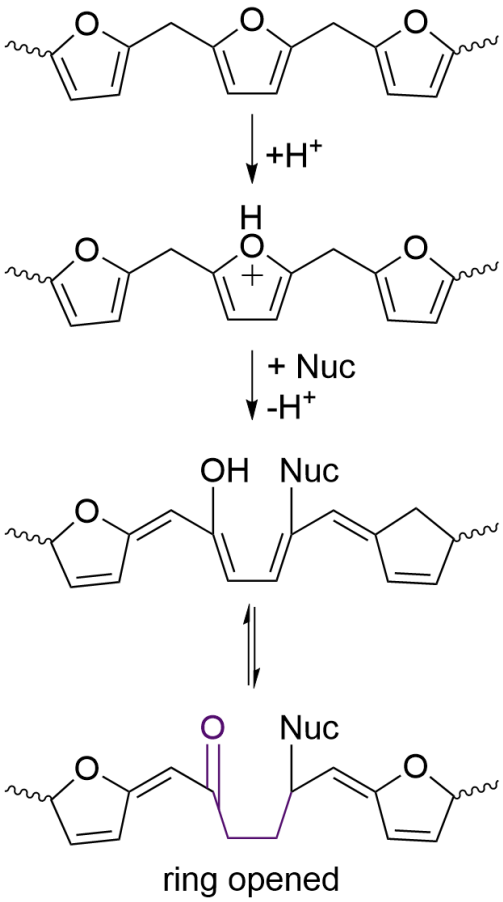
thermally resistant samples will tend to ablate instead of form LIC.[23,27] Thermal stability of the PFA samples will be correlated to the inclination of the samples to LIC formation in Chapter 4 to assess its effect on the resulting LIC.

3.2 Promoting Furan Ring Opening in PFA

3.2.1 Introduction

Aside from modifying the chain length, targeting the concentration of furan ring opening along the chain was also of interest. Increased ring opening implies a decrease in the polymer's aromaticity. They appear in the polymer chain by a side reaction that opens the furan ring.[39,66] Targeting this reaction requires additional reactants in the polymerization, which can be achieved simply by performing the reaction in a solvent. Solvent effects on PFA have been broadly studied, ranging from polar protic solvents like water and isopropyl alcohol[66] to non-protic solvents such as acetone,[64] each affecting the PFA structure to varying degrees. He et al. did not report structural differences when water, ethanol, or acetone were used as reaction solvent.[64] Isobutanol and n-butanol were found to negatively affect reaction kinetics through steric hindrance of the monomers, though their effect on the resulting polymer structure was not explored.[30] Falco et al. prepared PFA with water and isopropyl alcohol (IPA) as solvents and found that the ring opening reaction was amplified when they were present in the reaction mixture.[66] This applied to furan rings in the FA monomer, oligomers, end groups, or within the polymer backbone. The increased amount of ring opening led to noticeable differences in the mechanical properties of the final PFA, shown by decreased glass transition temperatures of the samples prepared in solvent. This influence of the solvent on FA polymerization can be explained by the ring opening mechanism.

In the ring opening reaction, the furan unit within the polymer opens into at least one ketone structure. Besides the linear furan unit, the ring opened structure is the next most prevalent in the resulting polymer network.[50] Within the polymer backbone, a furan ring is opened by an initial protonation of the oxygen atom followed by nucleophilic addition (Scheme 3.2). This results in the formation of the enol tautomer, which is in equilibrium with the favoured keto tautomer, the structure as which the ring-opened structure is most often depicted. Since the polycondensation reaction produces water, this reaction also occurs in the absence of solvent. Nucleophilic solvents can, however, further induce ring opening during polymerization.



Scheme 3.2. Reaction mechanism of furan ring opening within the chain in the presence of a nucleophile.

It should be noted that other ring-opening reactions involving FA monomers or end-groups of oligomers may also occur aside from the reaction occurring within the chain as described above. The formation of small molecules such as levulinic acid (LA) and furfuryl levulinate from the reaction between water and the FA monomer is well known.[39,66] This work focuses mainly on ring opening within the polymer backbone, though these byproducts can also influence the polymer matrix and resulting thermal properties.

In this section, a series of PFA was prepared in water, ethanol, and acetone. The solvents' effect on the ring opening side reaction was investigated by monitoring changes in the FT-IR bands related to ketones as a function of reaction solvent. The ring-opening reaction was promoted in each solvent, which was confirmed by the increased absorbance of the tracked bands as well as the absorbance ratio of the carbonyl and C-H wag bands. The resulting decrease in aromaticity

resulted in noticeably negative effects on the thermal stability of PFA, as shown by TGA measurements.

3.2.2 Characterization and Discussion

Visual observation of the PFA/solvent during polymerization affirm the solvent's influence on the reaction. PFA/no solvent is a baseline for the reaction sequence: the mixture is light yellow in its initial stage, and as the polymerization proceeds, it takes on a progressively darker brown colour. In the final stages of the reaction, the mixture becomes opaque and highly viscous. The increased viscosity indicates that the polymerization has reached the gelation stage of the reaction and can be cured. Polymerizations in the presence of solvent are evaluated relative to this benchmark reaction.

The three PFA samples with solvent added showed clear differences compared to PFA/no solvent even after only 30 minutes of mixing (Figure 3.5). There is a distinct phase separation in PFA/water since the PFA resin is immiscible with water. The added water sat on top of the resin, though its brown colour indicates some dissolution of FA, confirmed by the decreased volume of the remaining resin sitting underneath. At this time, the viscosity of PFA/water had already surpassed that of PFA/no solvent owing to the decreased volume of resin with the same concentration of acid catalyst. PFA/no solvent and PFA/water reached the desired viscosity around 2 and 3 hours of polymerization, respectively. Contrarily, the organic solvents added alongside the polymerization were fully miscible in FA and this property remained constant even through the later stages of the reaction. Whereas PFA/no solvent had already darkened after 30 minutes of mixing, PFA/ethanol and PFA/acetone had barely assumed a dark orange colour and was still translucent. The miscibility of ethanol and acetone in FA clearly slow polymerization kinetics, which may be due to dilution of the monomer reactant. Steric effects may also be at play, where the presence of solvent molecules can shield the monomer from the initial protonation therefore stunting the rate of chain growth.[30] Opacity was achieved by the PFA/organic solvent samples only after four hours of mixing and finally reached comparable viscosities to PFA/no solvent and PFA/water at the time of completion an hour after that, for a total polymerization time of 5 hours. These differences between the polymerization in the presence and absence of solvent are pronounced, and this remains true of the PFA/solvent samples post-curing.

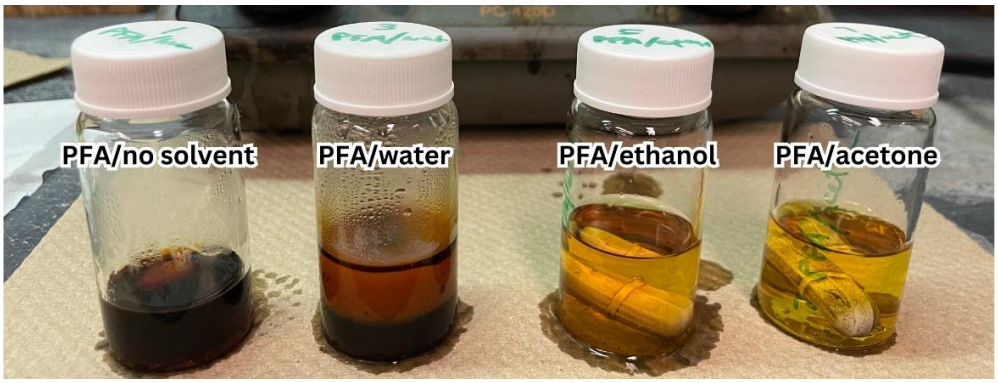


Figure 3.5. PFA/solvent samples showed distinct differences in colour and viscosity after 30 minutes of mixing. From left to right: PFA/no solvent, PFA/water, PFA/ethanol, and PFA/acetone.

Clear differences in the surface texture of the PFA samples were observed after curing overnight at 80°C (Figure 3.6). PFA/no solvent was smooth and matte upon curing, whereas the three other samples exhibited a sheen. PFA/water and PFA/ethanol both remained smooth on the surface, but PFA/acetone was significantly more porous despite being even upon pouring the mixture onto the PET substrate. Acetone has the lowest boiling point of the solvents (56°C)[71], which can explain the formation of holes where acetone is released as a gas during curing. The boiling point of ethanol is near the curing temperature, so gas release was likely slower leading to the observed smoother film. The volume of casted PFA/ethanol polymer significantly decreased after curing, which affirms that while the sample experienced solvent evaporation, it occurred at a much slower rate than PFA/acetone.



Figure 3.6. PFA/solvent samples post-curing. Clockwise starting in the top left: PFA/no solvent, PFA/water, PFA/acetone, and PFA/ethanol.

The FT-IR spectra of PFA prepared in varied solvents exhibit the expected peaks at 1014, 1505, 1560, 1610, 1680, and 1715 cm^{-1}, as described in Section 3.1 (Figure 3.7a). Within the 4000-2700 cm^{-1} spectral region, the typical sp^2 and sp^3 C-H stretches are observed in the 3100-2900 cm^{-1} range as well as a muted, broad O-H peak from 3600-3300 cm^{-1} attributed to the hydroxyl end groups in the polymer. PFA/no solvent had a significantly less intense FT-IR spectrum than PFA prepared in solvent and thus the lowest degree of polymerization in the series, whereas PFA/ethanol had the highest absorbance of the 1014 cm^{-1} band indicating the greatest degree of polymerization (Figure 3.7b). PFA prepared in water and acetone showed similar extents of polymerization to each other. The solvents thus promoted FA polymerization. Kim et al. showed previously that solvents can shield FA monomers from protonation, slowing the rate of reaction.[30] This consequence was observed in this synthesis, leading to longer reaction times for PFA in any solvent than PFA/no solvent (Table 2.2), which can increase degree of conversion.[72,73] Among the PFA prepared in solvents, the increased extent of polymerization in ethanol can also be attributed to the best match of ethanol and FA's solubility parameters (Figure 3.7c). Ethanol thus stays miscible in FA for longer, specifically through the gelation stage of the polymerization, further increasing the reaction time since the rate of viscosity increase is slowed. The absorbance of the 1560 cm^{-1} peak followed a similar trend as the 1014 cm^{-1} band, further supporting that these peaks in tandem can shed light on the furan units in the polymer backbone structure.

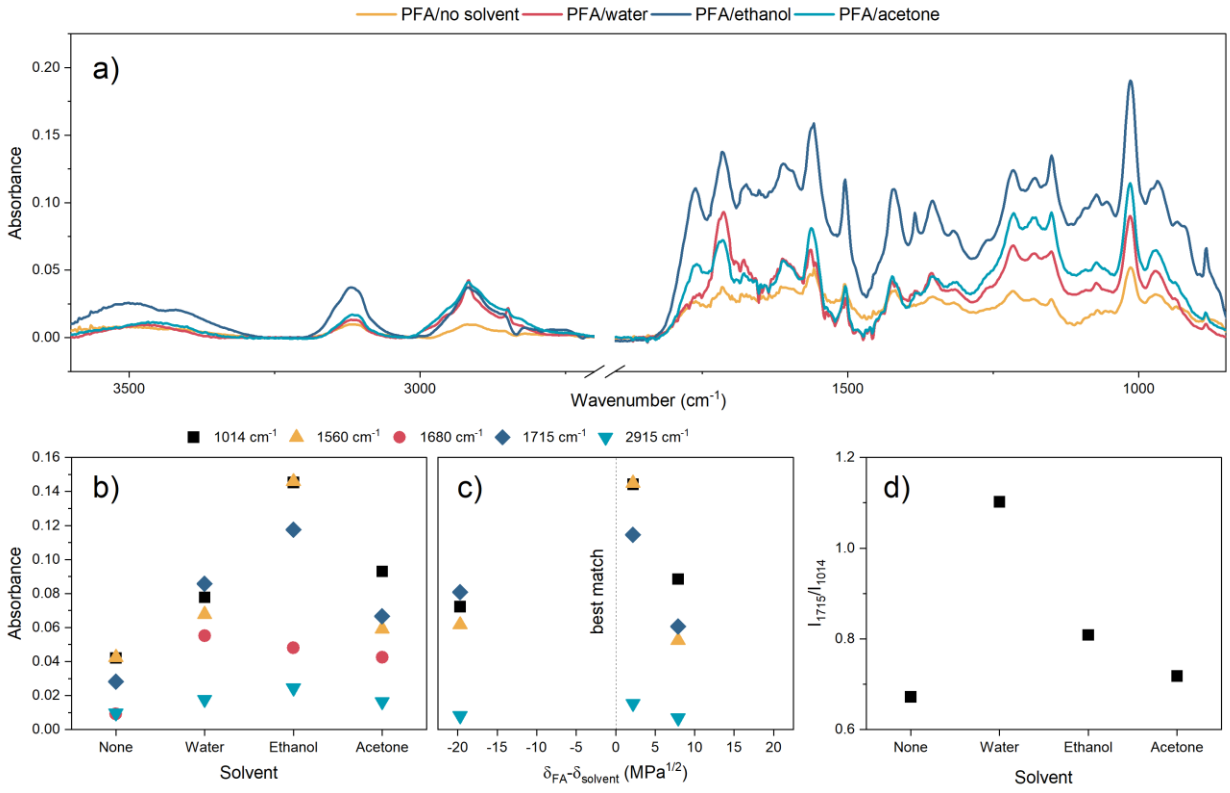


Figure 3.7. FT-IR characterization of PFA samples prepared in various solvents. (a) FT-IR spectra of PFA/no solvent, PFA/water, PFA/ethanol, and PFA/acetone. (b) Absorbances for the 1014, 1560, 1680 and 1715 cm^{-1} peaks as a function of polymerization solvent. (c) Similarity of solvent solubility parameter to solubility parameter of FA. Values closer to the dashed line at 0 are more similar to the solubility parameter of FA, indicating good compatibility. (d) I_{1715}/I_{1014} ratio of PFA prepared in various solvents.

The absorbances of the band at 2915 cm^{-1} in PFA/water and PFA/acetone are similar to that of PFA/ethanol, despite the overall lower intensity of their FT-IR spectra. There must be structural differences induced by water and acetone that increase the concentration of sp^3 carbons in the polymer which cannot be explained only by the degree of polymerization. Solvents can also promote small molecule formation during polymerization, such as LA with two additional sp^3 carbon centers, which is formed by the reaction between water and FA.[30] Acetone does not participate in any known reactions with FA to form low molecular weight species. Its two methyl groups may contribute minorly to this band, but it is unlikely for a significant amount to remain in the matrix after curing due to the reaction and curing temperatures. The Diels-Alder crosslinking motif (Scheme 2.1) contains more sp^3 carbons, which may be the reason for the increased

absorbance of the 2915 cm^{-1} band, though FT-IR alone cannot confirm their existence. Other characterization techniques discussed below attempt to shed light on these results.

A significant change across this series of samples is the development of the peak at 1715 cm^{-1}, which reveals the extent of furan ring opening in PFA. The absorbance of this band increased in the order of PFA/no solvent < PFA/acetone < PFA/water < PFA/ethanol, in agreement with the promotion of the ring opening side reaction by nucleophilic solvents.[66] Though the ketone forms in PFA even in the absence of solvent, opening the furan ring relies on the small amount of water that forms as a byproduct of the polymerization. The solvents act additionally as nucleophiles, which allows the side reaction to proceed more frequently.[66] The 1715 cm^{-1} band in the PFA/water spectrum also includes contributions from the levulinic acid (discussed earlier), but the small shoulder at 1760 cm^{-1} indicates that only a minor amount is formed. Acetone itself exhibits a strong ketone peak at this frequency, though it is not a significant contributor for reasons previously mentioned. Because of the increased ring opening in PFA prepared in solvent, the backbones of PFA/ethanol, PFA/water, and PFA/acetone contain greater amounts of aliphatic motifs than PFA/no solvent.

To quantify this, the degree of ring opening in the PFA network is approximated by a ratio of the absorbances of the ring opening band at 1715 cm^{-1} and the band at 1014 cm^{-1} (I_{1715}/I_{1014}) indicating the degree of polymerization. This metric allows a more representative assessment of the contributions of structural combinations observed in PFA to its properties, rather than viewing singular motifs as acting in a vacuum. It must be noted that values are overestimated due to the contributions from small molecules and ring opened FA monomers and oligomers to the absorbance of the 1715 cm^{-1} band. The I_{1715}/I_{1014} ratio of PFA/water was over 1, the highest of the series, indicating a significantly higher composition of aliphatic bonds in the structure (Figure 3.7d). The I_{1715}/I_{1014} ratio of PFA/no solvent was 0.71 in contrast, whereas the values for PFA/ethanol and PFA/acetone were intermediate between the two.

Conjugated ketone motifs are tracked by the band at 1680 cm^{-1}, which is observed to have the lowest absorbance for PFA/no solvent and relatively similar values for PFA prepared in any of the solvents. Despite being closely linked to the ketone peak, the absorbance of this band does not vary to the same extent as the 1715 cm^{-1} band. This indicates that conjugation in the PFA backbone

does not have a dependence on the solvent and that the PFA structures do not vary significantly in conjugation.

Swelling data was inconclusive and therefore is omitted for this series. The PFA did not exhibit any swelling behaviour over 24 or 48 hours, including PFA/no solvent. Further investigation is required to determine whether there was an issue with the experimental method or if the samples were highly crosslinked, as the ring opening motif can also appear in tandem with Diels-Alder crosslinking.[49] Previous work has shown, however, that increased ring opening reduces the possibility of conjugation along the chain which is required for the Diels-Alder reaction to occur, so lower crosslinking would be expected.[66] The crosslinking density of the PFA/solvent series is thus unclear.

The same TGA metrics discussed in Section 3.1 are used to assess the thermal stability of the PFA/solvent series. TGA and DTG curves for the PFA prepared in various solvents show noticeably different thermal degradation mechanisms, a consequence of the structural variations discussed previously (Figure 3.8a). PFA/acetone was the most thermally stable of the series, with the highest $T_{5\%}$, residue at 800°C, as well as onset and peak temperatures for the second mass loss event (Figure 3.8b-d). Its $T_{5\%}$ was 226°C, which was the most similar to that of the PFA/acid concentration series. PFA prepared in no solvent or water and ethanol had significantly lower $T_{5\%}$, with PFA/ethanol having the lowest at 190°C. The high degree of mass loss at low temperature is attributed to evaporation of residual ethanol trapped in the PFA network.[74] The differences in the cured polymer matrix with each solvent thus causes $T_{5\%}$ to be an incomparable metric for the thermal stability of these polymers. Despite the significant early mass loss, PFA/ethanol had 47% residue at 800°C, comparable to PFA/acetone at ca. 48% residue. This suggests that the polymer network itself had high thermal resistance. The onset temperature of the second mass loss event for PFA/water, corresponding to furan ring degradation, was the lowest of the series at 289°C. This value is also the lowest of the two series overall, suggesting that the PFA/water network is comprised of weaker bonds than the other polymers. Finally, the peak temperature of the final mass loss from the removal of H_2 and CO is consistent for all samples at ca. 450°C. The thermal degradation mechanisms observed for this PFA series are varied, hinting at distinct polymer structures.

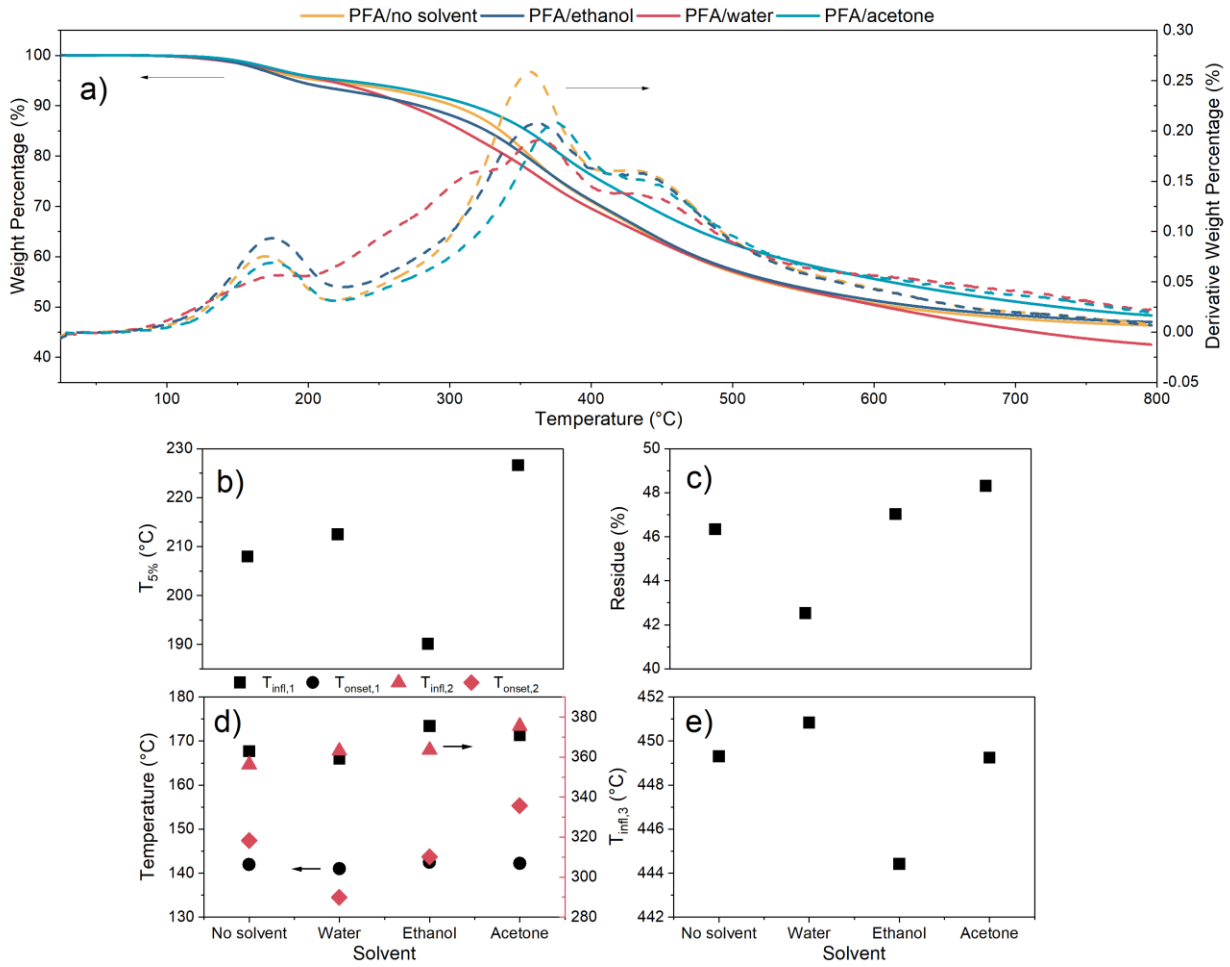


Figure 3.8. TGA analysis of PFA samples prepared in different solvents. (a) TGA (solid lines) and DTG (dashed lines) graphs of each PFA sample. (b) $T_{5\%}$, (c) residue at 800°C, (d) onset temperatures and peaks of the DTG curves for the first (black) and second (red) mass loss events, and (e) peak of the DTG curve for the third mass loss event as a function of solvent.

An attempt to deconvolute these structures is made by correlating the structural characterization techniques to the observed thermal properties. The absorbances of structural features observed by FT-IR do not have direct relationships with the thermal stability metrics obtained by TGA (Figure 3.9a-b). However, it is challenging to relate singular structural motifs to the complex degradation pathways as discussed above, particularly since the FT-IR data suggested varied structural composition between different PFA. Since the most significant difference was in the degree of ring opening, the resulting I_{1715}/I_{1014} was also correlated to thermal stability. PFA with higher I_{1715}/I_{1014} had lower onset temperatures for the second mass loss and residue, which can be explained by the consequently decreased aromaticity (Figure 3.10c-d). When the furan ring

is opened, strong C=C bonds with 611 kJ/mol bond strength are substituted with C-C bonds with weaker bond strengths of 345 kJ/mol, allowing chain degradation to occur at lower temperatures.[75]

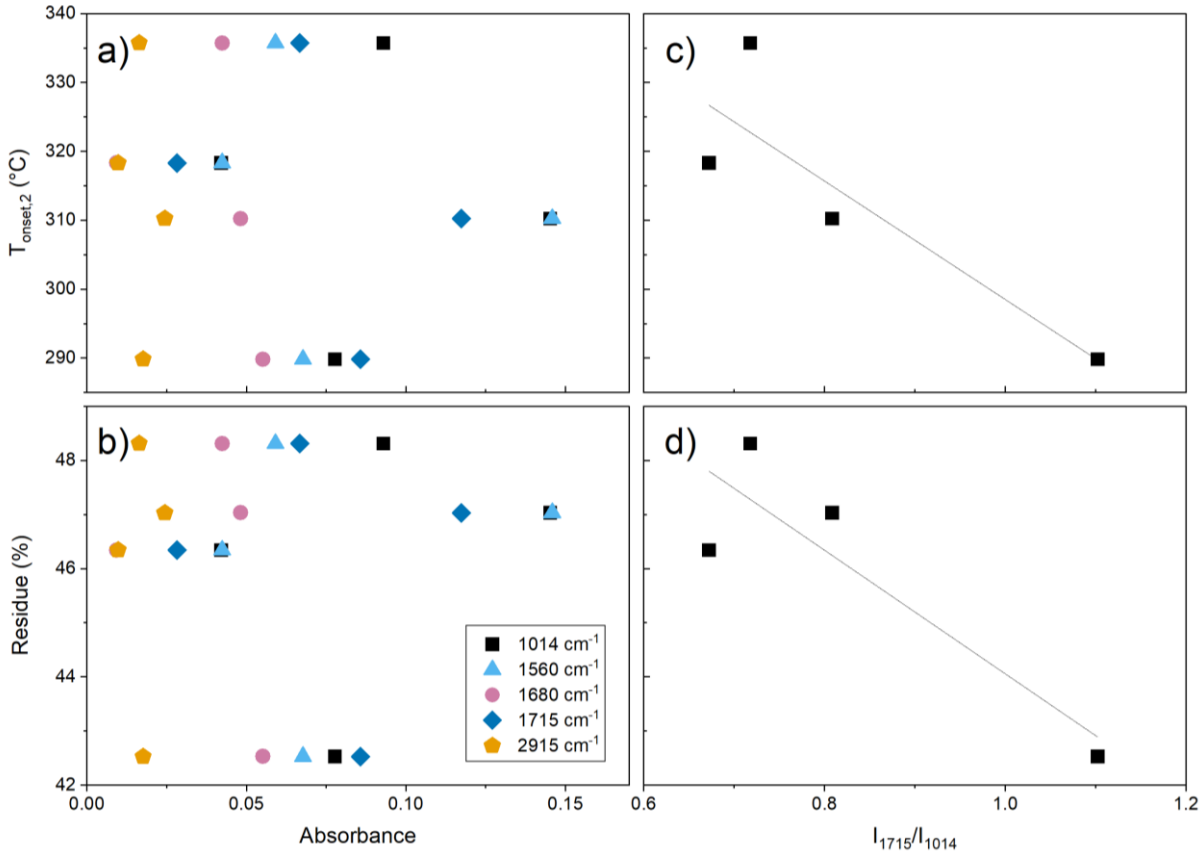


Figure 3.9. Correlations between structural data from FT-IR and thermal stability metrics from TGA for PFA/solvent series. (a, c) $T_{onset,2}$ and (b, d) residue at 800°C as a function of absorbance for selected bands and I_{1715}/I_{1014}, respectively.

Overall, characterization of the PFA/solvent series pointed to PFA with varied degrees of ring opening and therefore aliphatic bonds. The FT-IR spectra showed clear differences between the concentrations of the expected ketone structures in each sample, with the three solvents promoting both overall polymerization and the ring opening side reaction. A combination of factors such as extended reaction time due to solvent-polymer compatibility and the addition of nucleophiles contribute to these structural variations. The resulting decrease of aromatic groups in the PFA structure corresponded to decreased thermal stability for the PFA/ethanol and PFA/water samples, whose effect on carbonization will be discussed in Chapter 4.

3.3 Steric Effects During Polymerization

3.3.1 Introduction

Alongside the functional groups, another important property of PFA as a thermoset polymer is its crosslinking density. This PFA/alkanol series was an exploration of how steric effects could hinder the crosslinking of the PFA network, inspired by the reaction scheme originally reported by Falco et al. (Scheme 3.2).[66] They depicted the attachment of IPA to the polymer backbone during the ring opening reaction, and so a hypothesis formed wherein attaching longer, 'bulkier' alcohols would cause steric hindrance and entanglements within the polymer network to decrease the efficiency of crosslinking by keeping chains apart as the attached alcohol increased in length. Even without attaching to the backbone, the alcohol would still impart steric effects on polymerization kinetics as mentioned previously by shielding sites from protonation.[30]

In this section, a series of PFA was prepared with various 1-alkanols as a reactant, ranging from ethanol to 1-octanol. Despite slight variations observed in the FT-IR absorbances for some structural motifs, no trends between the resulting polymer structure and length of the alcohol chain were found. Polymer swelling and TGA measurements also did not exhibit trends, confirming that the addition of progressively longer alkanols to polymerization has little systematic influence on the PFA structure, though the series had the overall highest thermal stability of the three PFA series.

3.3.2 Characterization and Discussion

Differences in the polymerization of the PFA/alkanol samples were apparent by visual comparison during the reaction, not only between samples but also against the other two PFA series. Instead of the typical colour progression from light yellow, to dark orange, to an opaque brown, the PFA/alkanol samples took on a green hue during polymerization instead of the typically observed orange (Figure 3.10). The control sample (FA polymerization without alcohol) exhibited the same green colour, indicating that the alcohols do not contribute to this change. Aside from the alcohols, the other difference in this series' synthesis is the acid catalyst; instead of oxalic acid, sulfuric acid was used in this series to shorten polymerization time to alleviate the steric effect on kinetics (described in Section 3.2). Sulfuric acid is commonly used in FA polymerization and several studies have compared the influence of different acid catalysts,[64,76] but this behaviour has not been described. Pure FA is colourless, but exposure to air will gradually turn the liquid yellow

as is the case with the FA used in these syntheses. The observed discolouration indicates the development of long conjugated systems, which can be interrupted by the electrophilic addition of sulfuric acid to the alkenes, causing a blue-shifting of the colour.[75] Over the course of the polymerization, the mixtures' colours gradually darkened as expected but maintained its green hue.

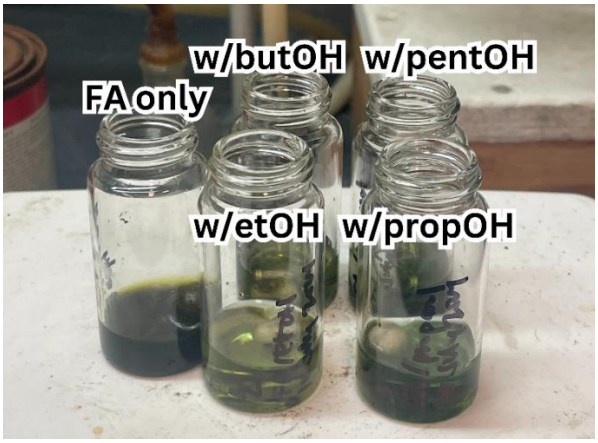


Figure 3.10. Image of PFA/alkanol samples during mixing.

The cured PFA/alkanol samples had a shiny finish, as was also observed for the PFA/ethanol sample in the series described in Section 3.2 (Figure 3.11). This texture is not observed on PFA prepared without alcohol. The alcohols used in this series have boiling points considerably above the curing temperature, slowing their evaporation from the film. They remain in the matrix, whether incorporated or unincorporated in the polymer chain itself.

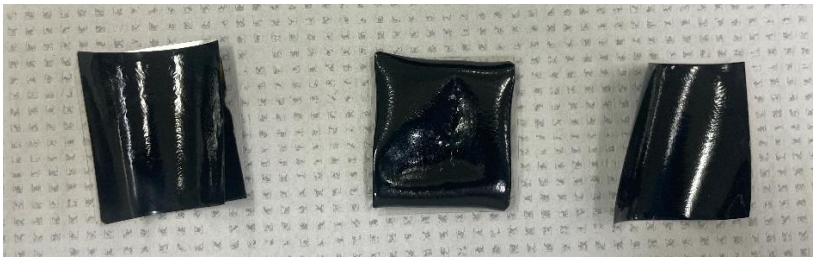


Figure 3.11. PFA/alkanol samples post-curing on PET.

FT-IR spectra of PFA prepared with various long chain alkanols show the expected bands described in Table 3.1, indicating that FA polymerization was achieved with the various alkanols (Figure 3.12a). Additional bands at 885 and 735 cm^{-1} which were not discussed previously are observed in these spectra, which are assigned to out-of-plane furan C-H vibrations and bends, respectively.[49,63,76] A reduction of these bands' absorbances suggest increased linear chain

polymerization or crosslinking in PFA owing to the consumption of the furan ring hydrogen.[63] Another peak at 1460 cm^{-1} appeared only in the PFA/hexanol, PFA/heptanol, and PFA/octanol samples, which is likely an artifact of residual alcohol.

Overall differences in the PFA/alkanol structures are observed, though not in a clear trend (Figure 3.12b). The spectra are normalized to the 1014 cm^{-1} band because significant differences in the PFA density of this series made it challenging to accurately weigh samples for FT-IR analysis. Differences in the 3600-2700 cm^{-1} spectral range characterize the alkanols in the final PFA film. The broad peak centred at 3450 cm^{-1} is the O-H stretch of the hydroxyl groups and decreases as the length of the alkyl chain increases due to the decreased concentration of hydroxyl groups by volume. From 3000-2800 cm^{-1}, increased absorbances are observed with increasing alkanol length due to the greater concentration of aliphatic C-H stretches from the alkyl chains. There is also a progressive decrease in the absorbance of the 1715 cm^{-1} band compared to PFA/no alcohol and with increasing alkanol length, indicating that less ring opening occurs when PFA is prepared with longer chain alkanols. This could be attributed to shielding effects that prevent the initial protonation of the oxygen in the furan that are enhanced with longer alkyl chains.[30] Absorbances of the 735 and 885 cm^{-1} bands fluctuated around the same value across the series which makes it difficult to assess the degree of crosslinking with certainty. The other bands showed similar variations in absorbances across the series. In each case, the minimum absorbances were observed for PFA/pentanol, and maximum absorbances arose from PFA/propanol and PFA/heptanol. It is thus not possible to make meaningful structural comparisons between PFA prepared with different alkanols using FT-IR data alone.

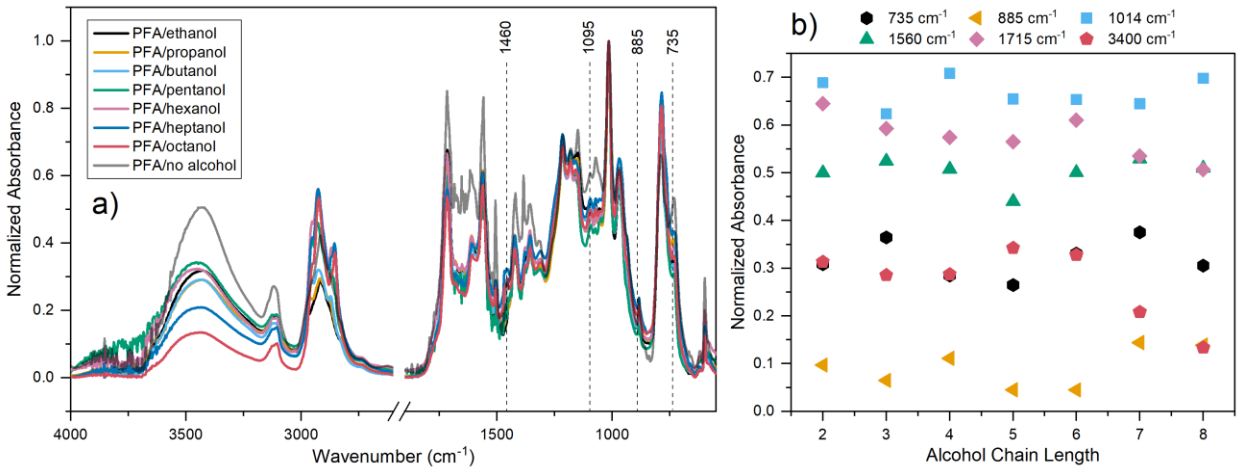


Figure 3.12. Transmission FT-IR analysis of PFA prepared with various long chain alcohols. (a) Normalized FT-IR spectra for the PFA/alcohol series, including PFA prepared with the same synthesis without alcohol. New peaks are marked by a dashed line. (b) Changes in the absorbances of selected bands as a function of alcohol chain length.

A similar fluctuation is observed in the swell test results (Figure 3.13), though PFA/C_{5-8}OH showed similar values. PFA/propanol showed a significantly lower swell ratio out of all the samples, potentially indicating a higher degree of crosslinking. Overall, there is significant overlap between the swell ratios measured for each PFA. The swell ratios alone are thus not sufficient to distinguish crosslink densities between the PFA/alcohol samples.

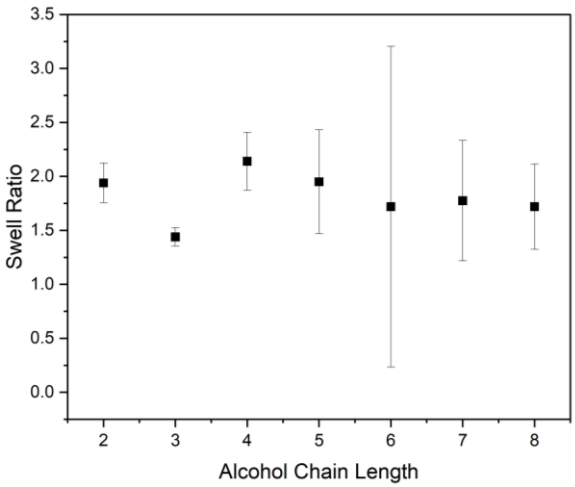


Figure 3.13. Average swell ratios of the PFA/alcohol samples. Error bars show the standard deviation.

Thermal stability measurements of the PFA/alcohol samples further showed minor variations in the thermal stability across the series (Figure 3.14a). $T_{5\%}$ varied in the range of 165-195°C across the sample series, decreasing in the order of PFA/propanol > PFA/ethanol > PFA/butanol > PFA/hexanol > PFA/pentanol > PFA/octanol > PFA/heptanol (Figure 3.14b). The samples prepared with longer alcohols exhibit significantly more mass loss in the first event than the others due to their higher molecular weights. The residual masses varied systematically across the series, with less overall decomposition observed in the PFA samples prepared with shorter alcohols (Figure 3.14c). PFA/ethanol was the most thermally resistant with 50.7% residue, whereas PFA/heptanol had the most decomposition with 44.4% residue. No clear trend is observed for the onset and peak temperatures of the first mass loss (Figure 3.15d). The onset temperature of the second mass loss generally increased with longer alkanol length. This event occurs at 355°C for PFA/octanol, the highest of the series, whereas it begins at 349°C for PFA/ethanol. The third mass loss event, which is well defined in the DTG curves of the previous two PFA series, is not prominent except for PFA/ethanol. DTG curves for PFA/$C_{4\text{-}7OH}$ showed a small bump around 630°C, which was not observed in the analysis for the previous two series. This is not reported in PFA literature; however, it suggests decreased thermal stability compared to the PFA that does not exhibit this mass loss.

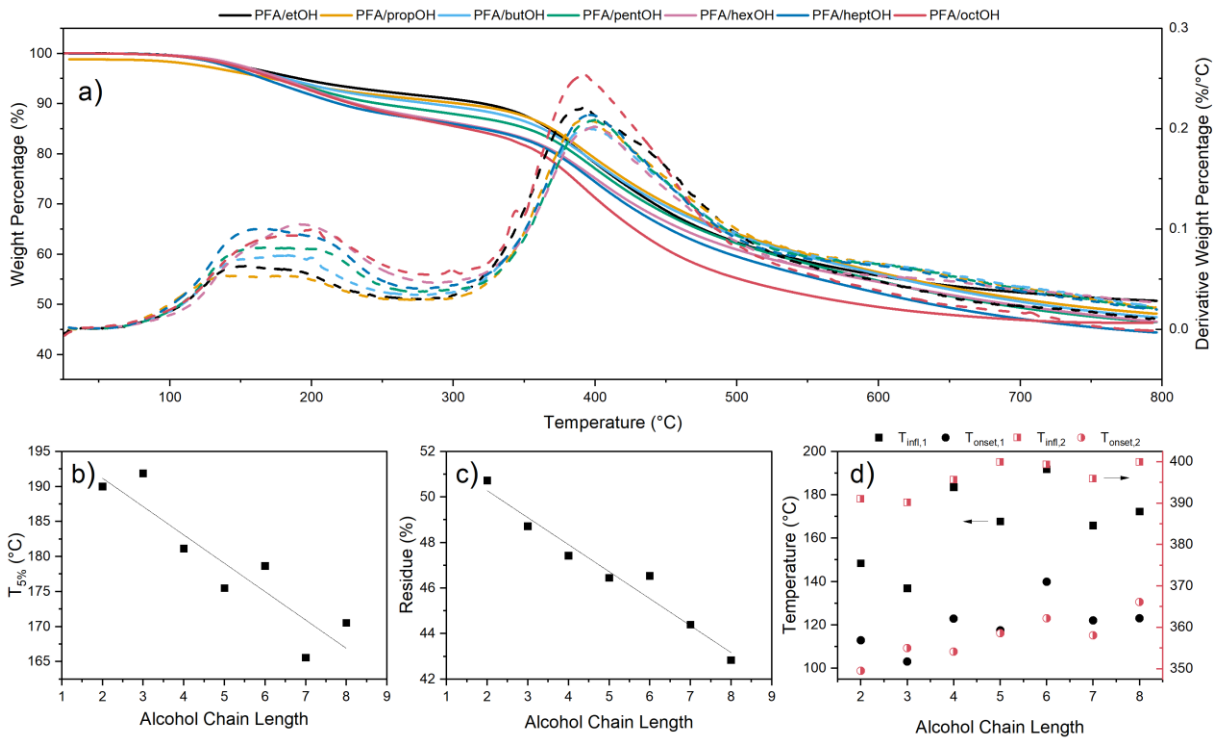


Figure 3.14. TGA analysis of PFA samples prepared with various alcohols. (a) TGA (solid lines) and DTG (dashed lines) graphs of each PFA sample. (b) $T_{5\%}$, (c) residue at 800°C, and (d) onset temperatures and peaks of the DTG curves for the first (black) and second (red) mass loss events as a function of the alcohol chain length.

It is unclear how changes in the PFA structure after preparation with different alkanols influence the thermal stability. The residues and onset temperatures do not show systematic changes as a function of FT-IR peak absorbances despite their trends across the series (Figure 3.15a). No trend was observed in the crosslinking density between PFA prepared with various alkanol lengths (Figure 3.15b). However, the absorbance of the 735 cm^{-1} band, whose reduction can be attributed to increased linear polymerization or crosslinking, decreased with decreasing crosslinking (Figure 3.15c). Meanwhile, the absorbance of the band at 1014 cm^{-1} increased with decreased crosslinking. This indicates that linear chain polymerization dominates in the PFA/alcohol series, particularly when prepared with longer alkanols. Overall, significant structural differences were not observed between PFA prepared with various alcohols.

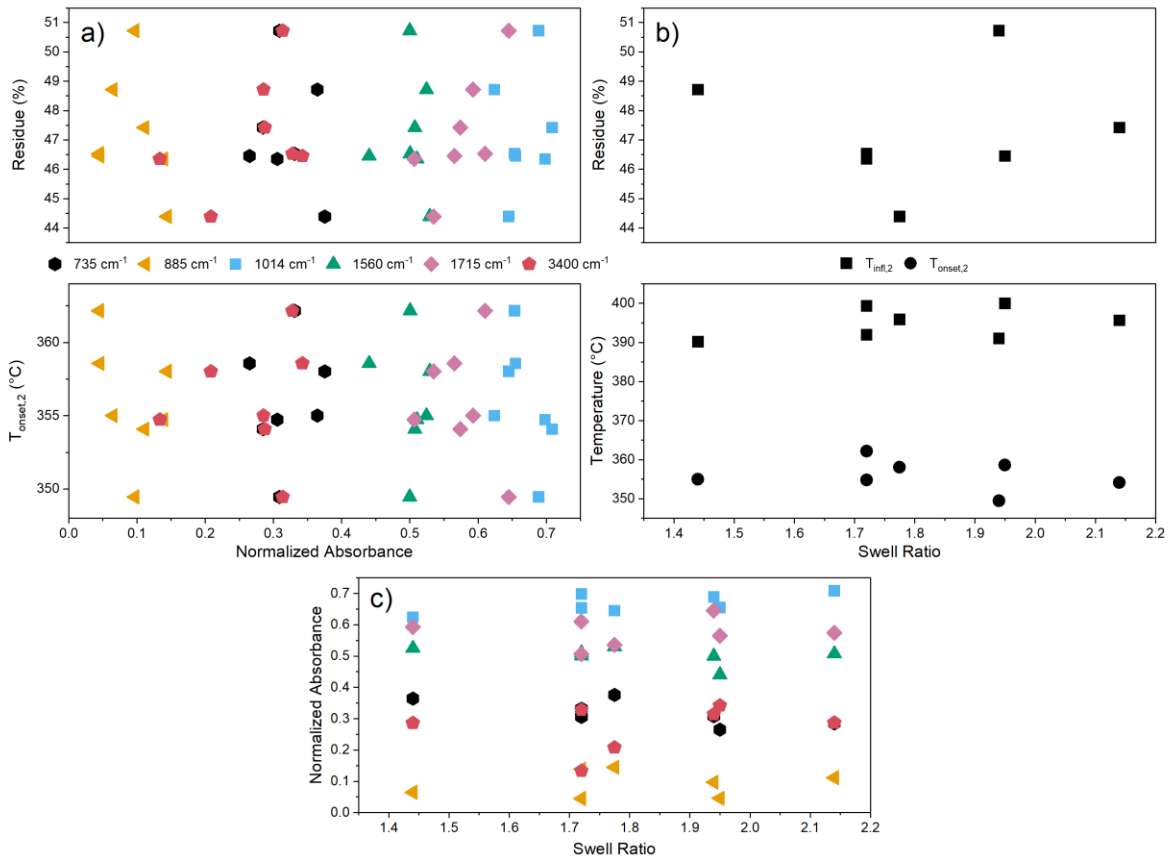


Figure 3.15. Structure-property correlations across all PFA/alcohol characterization techniques. (a) Thermal stability metrics, residue at 800°C and onset temperature of the second mass loss, as a function of FT-IR absorbances of selected peaks. (b) Thermal stability metrics as a function of swell ratio. (c) FT-IR absorbances as a function of swell ratio.

Characterization of the PFA/alkanol series suggests little influence of individual alkanols on the polymerization of FA. Though the initial hypothesis was for long chain alcohols to exert steric effects and entanglements on the PFA network through attachment to the polymer backbone, evidence of this was not observed by FT-IR, crosslinking, and TGA analysis. No notable or systematic differences in the structure were observed with increasing alcohol chain length. The thermal stability of the PFA were relatively similar across the series and few correlations between the structural information from FT-IR and swell tests and TGA metrics were observed, further confirming that FA polymerization with the addition of various alcohols did not significantly affect the resulting polymer. Linear polymerized chains are predominant in the structure of this PFA series over crosslinked networks.

Interestingly, despite the absence of significant changes in the structural features and thermal stability between individual PFA in the PFA/alkanol series, it exhibited noticeably improved overall thermal properties compared to the other series (Figure 3.17) PFA/alkanol had significantly lower $T_{5\%}$ out of the three series, likely due to the loss of high molecular weight species that were not present in the other polymers. Residue at 800°C stayed in the same range (40-50%) for all series. However, the average onset temperature for the second mass loss for PFA/alkanol was 357°C, which was significantly higher than PFA/acid concentration and PFA/solvent. Since the ring-opening structure was significantly decreased in the PFA/alkanol series (Figure 3.12a) compared to PFA/no alcohol, aromatic units are likely more prevalent in these polymers. This is also consistent with the finding that linear polymerization is dominant in PFA/alkanol over crosslinking as discussed above. The effects of the enhanced thermal stability of the PFA/alkanol series on LIC formation will be discussed in Chapter 4.

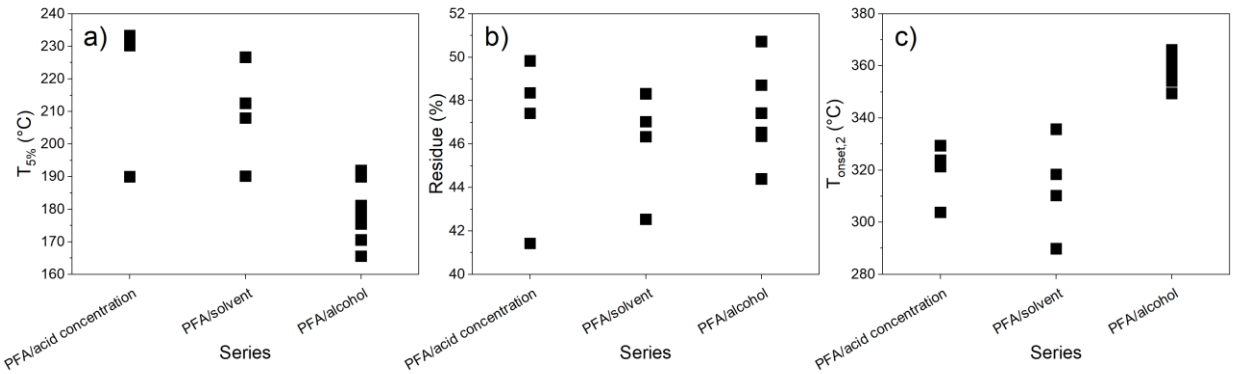


Figure 3.16. Thermal stability comparison of PFA prepared with three different syntheses. (a) $T_{5\%}$, (b) residue at 800°C, and (c) $T_{onset,2}$ values measured for all PFA series.

3.4 Conclusion

Though it has been established historically that the structure of PFA is sensitive to differences in synthetic parameters, this chapter demonstrated that it is possible to target certain functional groups or structures. An inverse relationship was observed between the degree of polymerization and the FA to acid catalyst ratio, which indicates that the PFA/acid concentration series encompasses PFA with varying chain lengths, different amounts of oligomers present in the matrix, and connectivity. Solvent effects were also pronounced in PFA synthesis, where water, ethanol, and acetone were shown to promote furan ring opening, resulting in higher concentrations of

ketones throughout the polymer chain. Consequently, PFA synthesized with such solvents is also more aliphatic in nature, which negatively affects its thermal stability. The PFA/solvent series thus includes samples with different concentrations of ketones and degrees of aromaticity. Finally, the crosslinking density of PFA was unsuccessfully targeted with the PFA/alcohol series. Alkanols did not significantly influence the polymerization of FA, with minor structural differences observed for PFA with various alcohol chain lengths. However, the PFA/alkanol series exhibited overall higher thermal stability than the other two series owing to predominant linear chain polymerization, which will influence LIC formation. The PFA/acid concentration and PFA/solvent series synthesized in this chapter thus encompass distinct structural differences that will allow a targeted investigation of their influence on PFA's performance as a substrate for LIC in the next chapter, while the enhanced thermal stability of the PFA/alcohol series will shed light on the necessity of high thermal resistance on LIC formation.

Chapter 4

Structurally Varied PFA as Substrates for Laser-Induced Carbonization

4.1 Introduction

The extensive work on extending the LIC technique to a range of polymer precursors has focused primarily on lasing parameters, with limited consideration of the substrate's chemical structure.[15,77,78] It is accepted that aromatic benzene motifs in the backbone facilitate the formation of the best quality LIC, as evidenced by the prevalence of polyimide usage in literature, but aliphatic precursors such as hemicellulose and cellulose-based materials have also successfully enabled LIC formation.[23,25] Few investigations have been done on the influence of structural variation between precursors on LIC formation.

Raman spectroscopy of carbons reveals a wealth of information and is the most used characterization technique for such materials. It can distinguish between members of the broad carbon family, including graphene, graphite, and glassy carbon, simply from extracting the peak shapes, positions, and intensities.[56,79–83] It is thus the primary characterization method used to compare LIC on different PFA in this work.

Three main peaks can be observed in the Raman spectra of carbonaceous materials: the D band at 1350 cm^{-1}, G band at 1580 cm^{-1}, and 2D band at 2700 cm^{-1}.[79] The appearance of peaks and their exact Raman shifts will vary depending on both experimental parameters such as the laser wavelength and the structure of the carbon material. The D band arises from disorder and defects such as 5- or 7-membered rings which are known to arise in LIG,[15] and its intensity and full width at half maximum (FWHM) indicate the degree of disorder; this peak is not observed in the Raman spectrum for pristine graphene. The G band arises from the in-plane sp^2 C-C stretch and is persistent in the Raman spectra for all materials comprised of sp^2 carbons. Finally, the 2D peak is the second overtone of the D peak. It is the most prominent peak in the spectrum of graphene, and its shape and height can reveal the number of layers present. The peak is sharp and intense in graphene, though may also appear in the spectra of more disordered carbons if random, single graphene layers are present.[52,84] Peak characteristics such as the FWHM and position reveal information on the carbon structure, as well as the intensity ratio of the D and G peak (I_D/I_G) which characterizes the degree of disorder in a carbon sample.

Depending on the nature of the carbon material and consequently its degree of order, such as the evolution from a pristine graphene monolayer to graphite to amorphous carbons, the characteristics of the observed peaks will vary (Figure 4.1). Previous laser-induced carbonization studies on PFA showed that the carbon material is glassy carbon instead of graphene,[26,27] and so a high I_D/I_G ratio and broad peaks are expected from the Raman spectra.[52,56] The D peak is expected to appear around 1350 cm^{-1} and the G peak at 1590 cm^{-1}. 2D bands can also appear in GC when heat treated at high temperatures, suggesting the formation of ordered nanocrystalline graphitic domains within the amorphous structure resulting in increased ordering.[52,84]

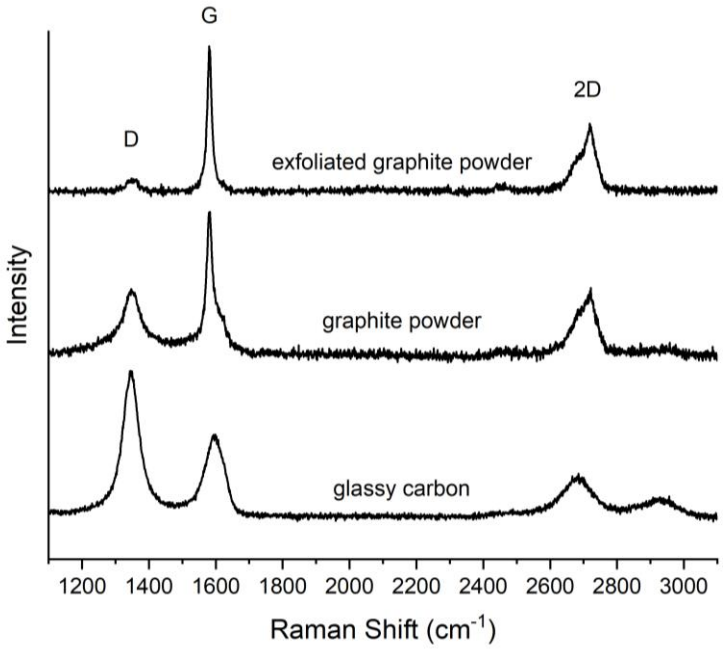


Figure 4.1. Raman spectra of exfoliated graphite powder, bulk graphite powder, and glassy carbon.

Within the disordered structure of glassy carbons, there is a range of disorder that the material can take on. This was explored by Ferrari et al.,[85] who quantitatively described an "amorphization trajectory" for disordered and amorphous carbons using Raman spectra (Figure 4.2). On the most ordered end of the trajectory is a graphitic sheet structure comprised of sp^2 bonds, and the most disordered structure that carbon can adopt is diamond-like, with a mixture of sp^3 and sp^2 bonds.[85] Glassy carbon falls in Stage 2 of the trajectory, meaning nanocrystalline graphitic domains can be found within its generally amorphous structure.[86] Using the position of the G peak and I_D/I_G ratio, along with other metrics such as the FWHM of the D peak, the 2D band characteristics, and I_{2D}/I_G ratio, the point along the amorphization trajectory on which the LIC

belongs can be determined. Subsequently, comparisons between the quality of the LIC formed on different precursors can be made using these metrics.

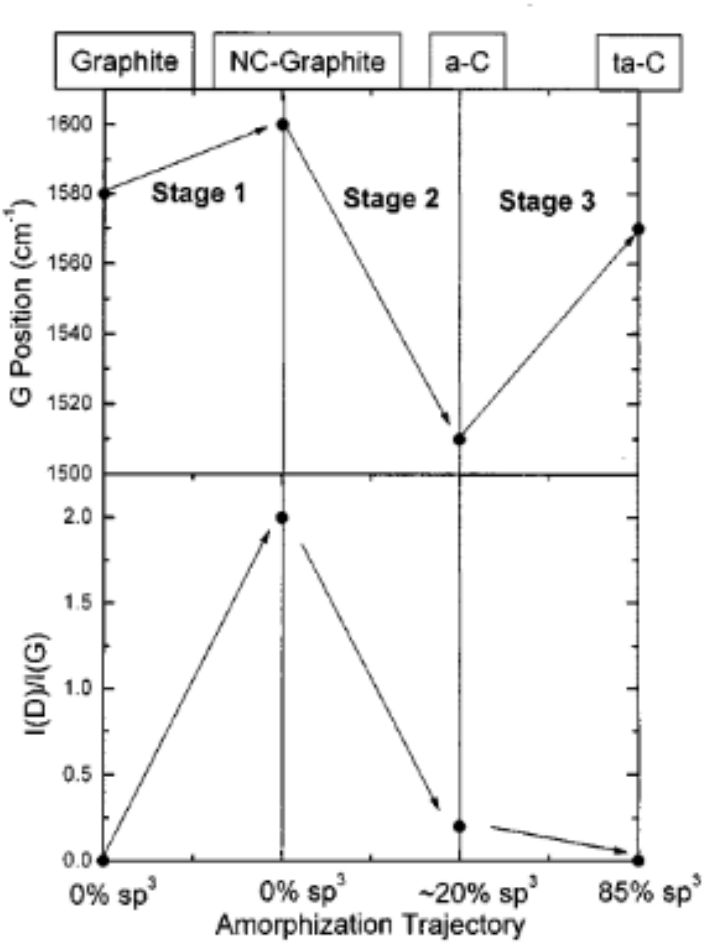


Figure 4.2. Amorphization trajectory of disordered and amorphous carbons. Reproduced with permission from American Physical Society.[85]

In this chapter, LIC formed on the three PFA series discussed in Chapter 3 – PFA/acid concentration, PFA/solvent, PFA/alkanol – are characterized by ESEM and Raman spectroscopy to investigate the effects of precursor chemistry on the laser-induced carbonization process. The effects of increased degree of polymerization as demonstrated by the PFA/acid concentration series, greater concentration of ring opening seen in the PFA/solvent series, and the enhanced thermal stability of the PFA/alkanol series are shown to have notable effects on LIC quality. Pristine PFA is shown to be a potential candidate as a precursor for laser-induced formation of glassy carbon, and the optimal structural features enable ordered LIC formation are revealed.

4.2 LIC on PFA with Varied Acid Concentration

SEM imaging of the LIC on the PFA/acid concentration series, where samples prepared with higher acid catalyst concentration had a greater degree of polymerization, showed systematic changes in the carbon morphology with increasing degree of polymerization (Figure 4.3). The images were taken on the best LIC formed from each precursor as determined by Raman analysis, discussed later in this section. Two distinct regions of carbonization were observed, corresponding to the first laser trace on the right and the "bulk" of the LIC on the left (Figure 4.3a,c,e,g). This is discussed in further detail in Section 4.3. On each precursor, the LIC exhibits a fibrous, foam-like structure. This has been previously observed for LIC on pristine PFA, though it is significantly different from that on other polymer precursors.[15,17,27] The foam-like morphology arises from the evolution of gases during lasing, which leaves holes in the structure.[15] PFA prepared with greater acid catalyst concentration, resulting in increased degree of polymerization as shown in Chapter 3, significantly reduced the porosity of LIC. PFA/0.3 M and PFA/0.4 M also did not form LIC as fibrous as PFA/0.1 M and PFA/0.2 M, instead creating a flatter structure. The increased degree of polymerization represents a more highly connected polymer network, which can slow the release of gases therefore decreasing the porosity of the LIC.

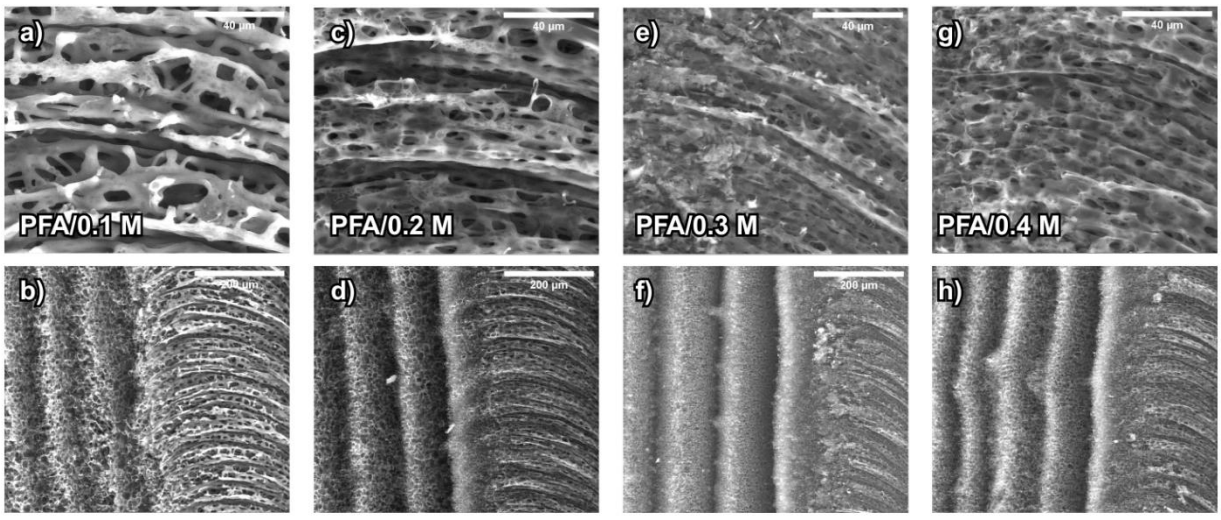


Figure 4.3. Top-down SEM images of optimal LIC formed by various laser powers on PFA/acid concentration. (a,b) PFA/no solvent (5.0 W), (c,d) PFA/water (5.0 W), (e,f) PFA/ethanol (4.90 W), and (g,h) PFA/acetone (4.95 W). (a,c,e,g) are at 1000x magnification and (b,d,f,h) are at 200x magnification.

Raman spectra of the LIC on PFA/acid concentration exhibits the expected D and G peaks at 1350 cm^{-1} and 1595 cm^{-1} respectively, confirming the formation of carbonaceous material on all PFA (Figure 4.4). The G peak position ca. 1600 cm^{-1} suggests that the LIC structure is Stage 2 of the amorphization trajectory, between nanocrystalline graphite and amorphous carbon, within this laser power range.[85] Its position stays constant across all laser powers (Figure 4.5a). On all precursors, the peaks are broad and overlapping when formed by lower laser powers but become increasingly separated as the laser power increases, signifying increased ordering of the structure. The FWHM of the D peak generally narrows with higher laser power, except in the case of PFA/0.3 M where a sharp increase is observed (Figure 4.5b). Narrowing of the D band is well-documented behaviour for pyrolytic glassy carbon that is heat-treated at high temperatures due to increased ordering, suggesting the formation of more graphitic LIC.[52,56,86,87] Several bumps appear in the spectra obtained on LIC formed at 4.80 W, which are attributed to the PET substrate showing through from PFA ablation and incomplete carbonization at this power.[88] The presence of single graphene layers at laser powers above 4.90 W is confirmed by emergence of a broad 2D peak.[27,52] This band is not typically observed in pyrolytic glassy carbon unless heat-treated above 1500°C.[52,84,86] This evolution of the Raman spectra shows that a threshold of thermal energy must be exceeded to form more ordered, graphitic LIC.

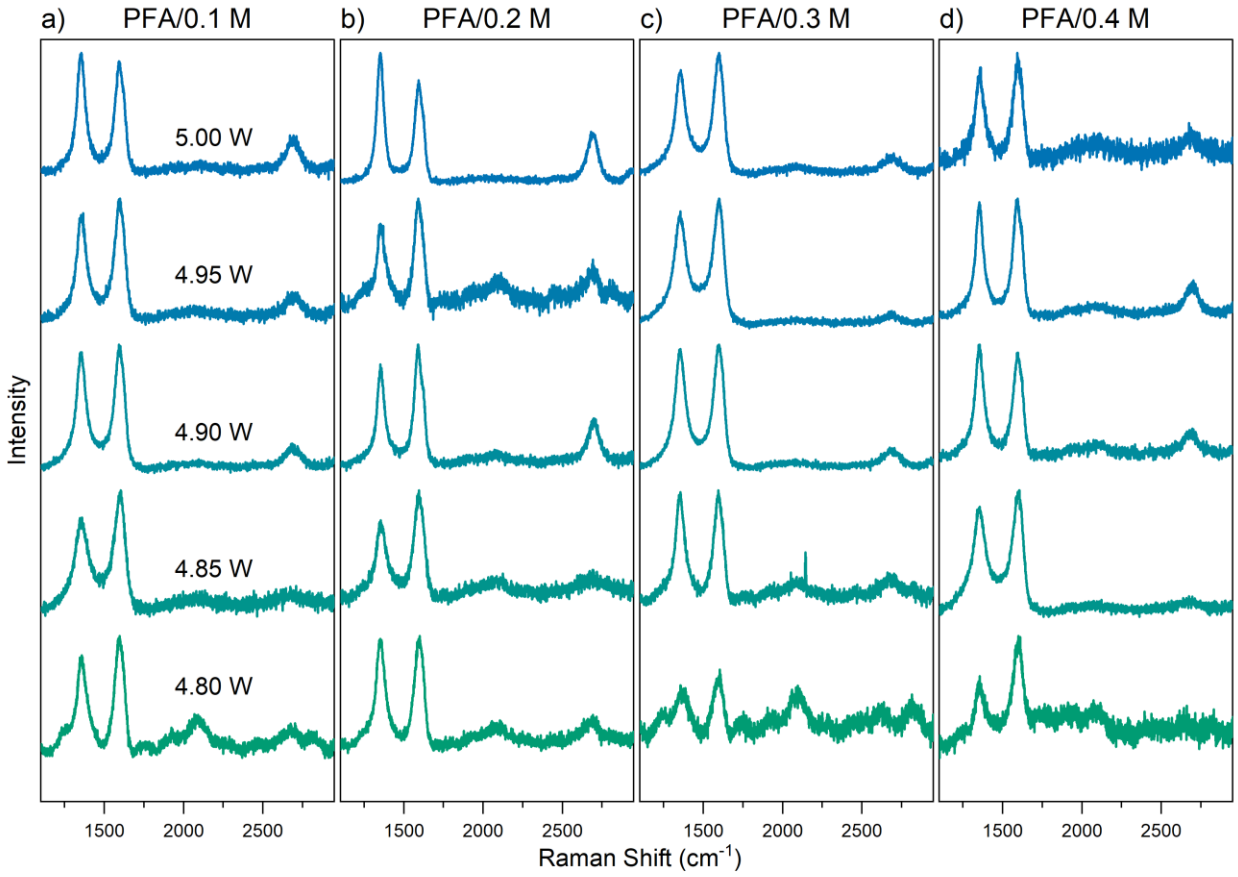


Figure 4.4. Raman spectra of LIC formed by varied laser powers on PFA/acid concentration. Spectra of LIC on (a) PFA/0.1 M, (b) PFA/0.2 M, (c) PFA/0.3 M, and (d) PFA/0.4 M.

Further analysis of the Raman spectra shows that the intensity ratio of the D and G peaks varies with increasing laser power (Figure 4.5c). For LIC on PFA/0.1 M, I_D/I_G increased with increasing laser power, whereas on PFA/0.3 M and PFA/0.4 M, the opposite relationship was observed (Figure 4.5c). In Stage 2 of the amorphization trajectory, increasing I_D/I_G indicates the formation of more graphitic crystalline domains.[85] This is supported by the simultaneous evolution and narrowing of the 2D band and subsequently increased I_{2D}/I_G at higher laser powers. The most ordered LIC on this series of precursors, hereby referred to as "optimal", would thus have high I_D/I_G, G peak position near 1600 cm^{-1}, as well as high I_{2D}/I_G and a narrow 2D band.[27] The laser power forming the optimal LIC according to these criteria is highlighted in green in Figure 4.6a. PFA/0.1 M and PFA/0.2 M both formed the optimal LIC with 5.0 W laser power whereas 4.90 W and 4.95 W were sufficient to form the best LIC on PFA/0.3 M and PFA/0.4 M, respectively. The Raman spectra obtained from the LIC formed by each optimal laser power are shown in Figure

4.6b. The 2D peak narrows significantly with higher I_D/I_G, further confirming the relationship between increasing I_D/I_G and structure ordering (Figure 4.6c).

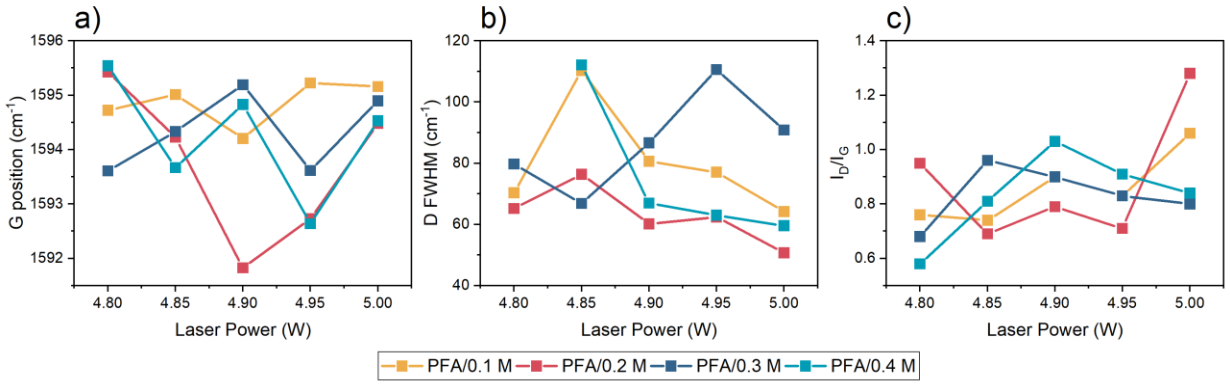


Figure 4.5. Raman analysis of LIC on PFA/acid concentration series. (a) Change in I_D/I_G, (b) position of the G band, and (c) FWHM of the D band on PFA as a function of laser power.

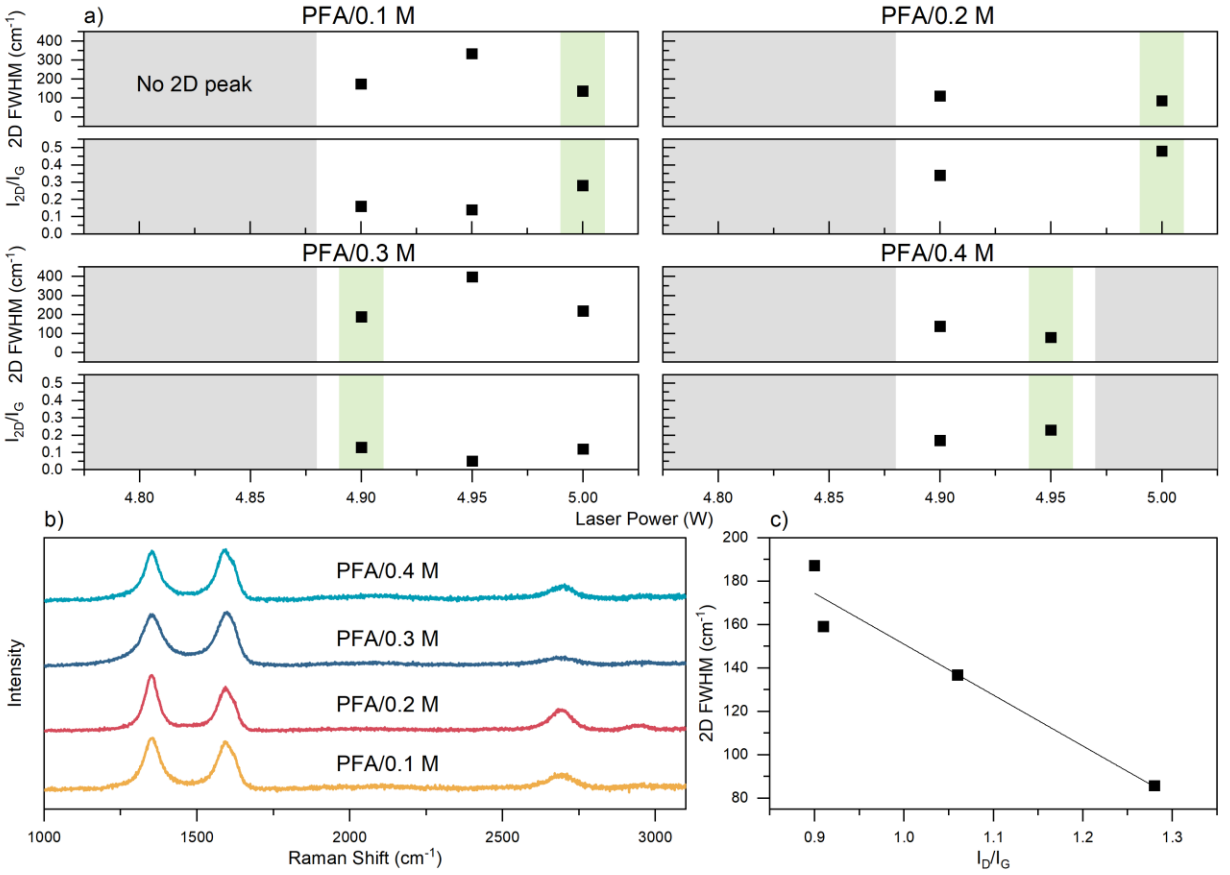


Figure 4.6. Analysis of the 2D band observed in the Raman spectra of LIC on PFA/acid concentration. (a) Comparison of the 2D band FWHM and I_{2D}/I_G for determination of the optimal laser power for LIC formation on PFA/acid concentration precursors. The optimal laser power

where the minimum FWHM and maximum I_{2D}/I_G is observed is shaded in green. Laser powers that did not result in 2D peaks are shaded in grey. (b) Raman spectra of LIC formed by the optimal laser power for each precursor. (c) Narrowing of the 2D band with increasing I_D/I_G for LIC formed by the optimal laser power.

The quality of the optimal LIC formed on each PFA differs between precursors, demonstrated by Raman analysis (Figure A.3). The G band appears at 1595 cm^{-1} for LIC on PFA/0.1 M, PFA/0.2M, and PFA/0.3 M but on PFA/0.4 M it appears at 1592 cm^{-1}, suggesting that PFA with higher degree of polymerization forms more disordered LIC (Figure 4.7a). PFA/0.2 M had both the lowest FWHM of the D band and highest I_D/I_G, as well as the most narrow 2D peak and highest I_{2D}/I_G (Figure 4.7b-e) of all PFA in this series. LIC on PFA/0.3-0.4 M showed similar I_D/I_G and I_{2D}/I_G, suggesting that the carbon structure is similarly disordered on both precursors. Of the four precursors, the optimal LIC formed on PFA/0.2 M thus exhibited the most graphitized structure.

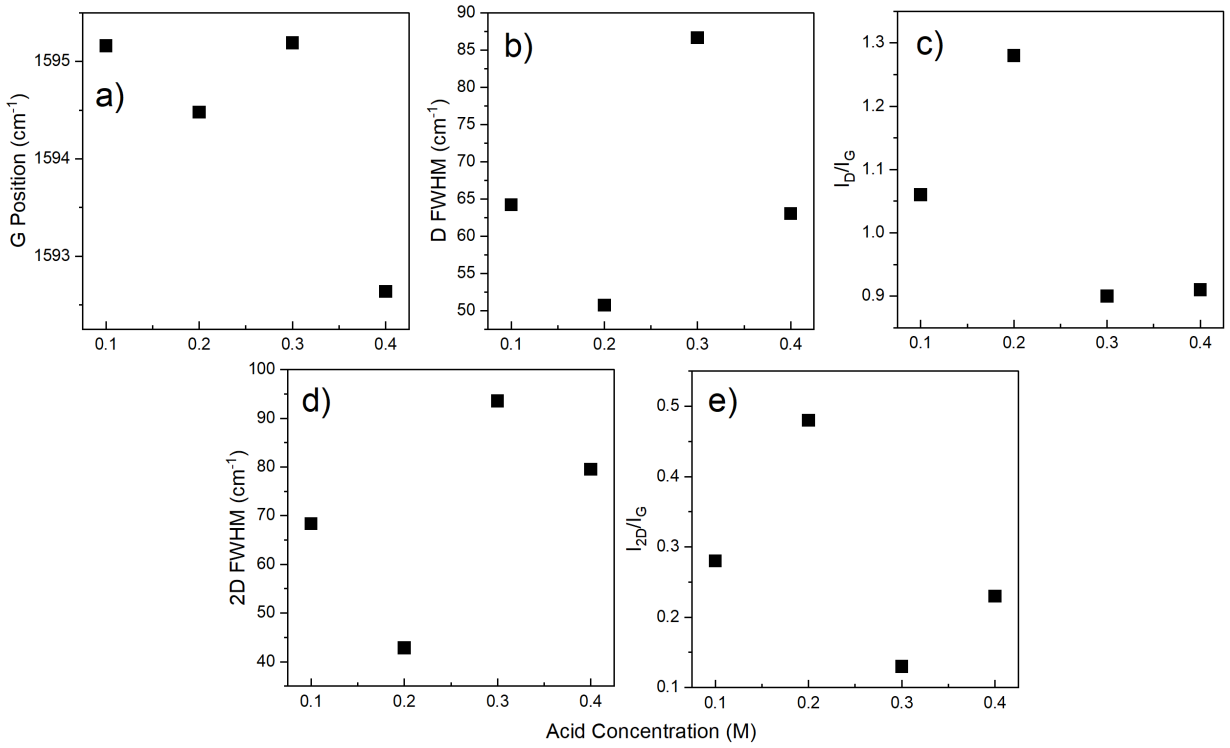


Figure 4.7. Raman analysis of the optimized LIC formed on PFA prepared with varied acid concentration. (a) Position of the G band, (b) FWHM of the D peak, (c) I_D/I_G, (d) FWHM of the 2D band, and (e) I_{2D}/I_G of the optimal LIC on each precursor.

As discussed in Chapter 3, PFA/0.1 M is an anomalous sample in that significantly more residual monomer and water was in the polymer matrix (Figure 3.3b) whereas the matrices of PFA/0.2 M, PFA/0.3 M, and PFA/0.4 M were similar, meaning differences in their properties are directly related to the polymer structure. This allows a systematic comparison of the structure's effect on the resulting LIC, and so focus is placed on these three precursors for Raman analysis.

Of the three remaining samples, PFA/0.2 M had the lowest degree of polymerization, and the LIC it formed was noticeably better in quality than LIC formed on PFA with higher acid concentrations (Figure 4.8a-d). A systematic trend is not observed, but higher 1014 cm^{-1} band intensity can be correlated to broader D and 2D peaks, along with lower I_D/I_G and I_{2D}/I_G seen with PFA/0.3 M and PFA/0.4 M. Increasing swell ratio of the precursor, which suggests lower crosslinking density, resulted in more ordered LIC. The least crosslinked PFA precursor had the minimum D peak FWHM and maximum I_D/I_G and I_{2D}/I_G of the series (Figure 4.8e-h). This is consistent with previous studies on the pyrolysis of polymers, where highly crosslinked carbon precursors were determined to be non-graphitizing.[89,90] The onset temperature of the polymer backbone degradation is linked with the crosslinking density as previously discussed, and of the three precursors, the least thermally stable PFA formed the best LIC (Figure 4.8i-l). From the structure-Raman data correlation, it appears that the crosslinking density of the PFA precursor has the most apparent effect on the degree of order of the LIC.

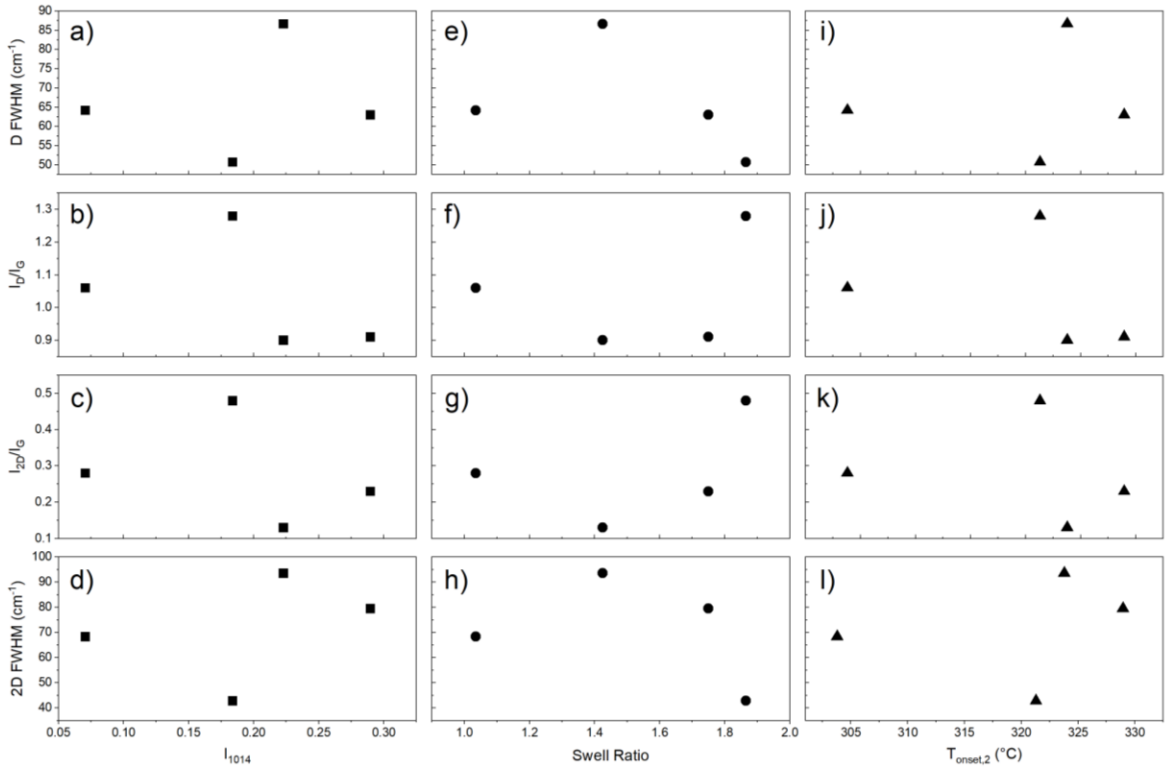


Figure 4.8. Structure-Raman correlation of the optimal LIC formed on PFA/acid concentration precursors. Changes in the FWHM of the D band, I_D/I_G, I_{2D}/I_G, and FWHM of the 2D band with (a-d) the intensity of the 1014 cm^{-1} band from FT-IR indicating the degree of polymerization, (e-h) swell ratio indicating the crosslinking density, and (i-l) onset temperature of polymer backbone degradation.

Analysis of the LIC formed from PFA precursors prepared with varied acid catalyst concentrations demonstrates that variations in the degree of polymerization impart noticeable effects on the carbon structure. PFA/0.2 M formed the most graphitic LIC, with its intermediate degree of polymerization and crosslinking. This is attributed to it having the lowest degree of crosslinking of the precursors, which enables increased graphitization.[52,90]

4.3 LIC on PFA with Varied Solvent

SEM imaging of the LIC formed from PFA prepared with various solvents showed morphological differences between samples with various extents of ring opening (Figure 4.9), though the general structures are similar except for LIC on PFA/water. The 50x magnification images show the entire width of the scribed LIC, which was comprised of three rows of laser lines (Figure 4.9a,d,g,j). Three regions of distinct morphologies were observed, corresponding to each pass of the laser.

The first region on the left consists of a fibrous, thickly branched morphology with visible bumps on the branched structures. In the narrow middle region, the fibrous structure ends abruptly and becomes a flat, porous structure. Finally, PFA is visibly ablated in the last region, though minimal GC formation is still observed. These three regions are likely the result of a combination of the multiple lasing effect and the non-uniform temperatures induced by the laser trace.[25,27,91] This effect is readily observed in the 200x magnification images (Figure 4.9b,e,h,k).

At 600x magnification, the fibrous morphologies of the first region can be examined on each PFA (Figure 4.9c,f,i,l). LIC formed on PFA/no solvent, PFA/ethanol, and PFA/acetone show similarly branched structures with significant bumps on the surface, indicating that gases were still being released at the time of carbonization. This suggests incomplete carbonization during lasing, as the gases are expected to be fully eliminated from the backbone for the remaining carbon atoms to rearrange into a graphitic structure.[15,92] The PFA/no solvent and PFA/ethanol LIC both exhibit a high degree of these bumps whereas PFA/acetone LIC contains noticeably less. The morphology of PFA/water LIC differs significantly from the rest. Though a porous structure forms, it is flat and does not have the same fibrous network. PFA/water was thus visibly more resistant to carbonization, even with multiple lases, compared to PFA prepared in other solvents.

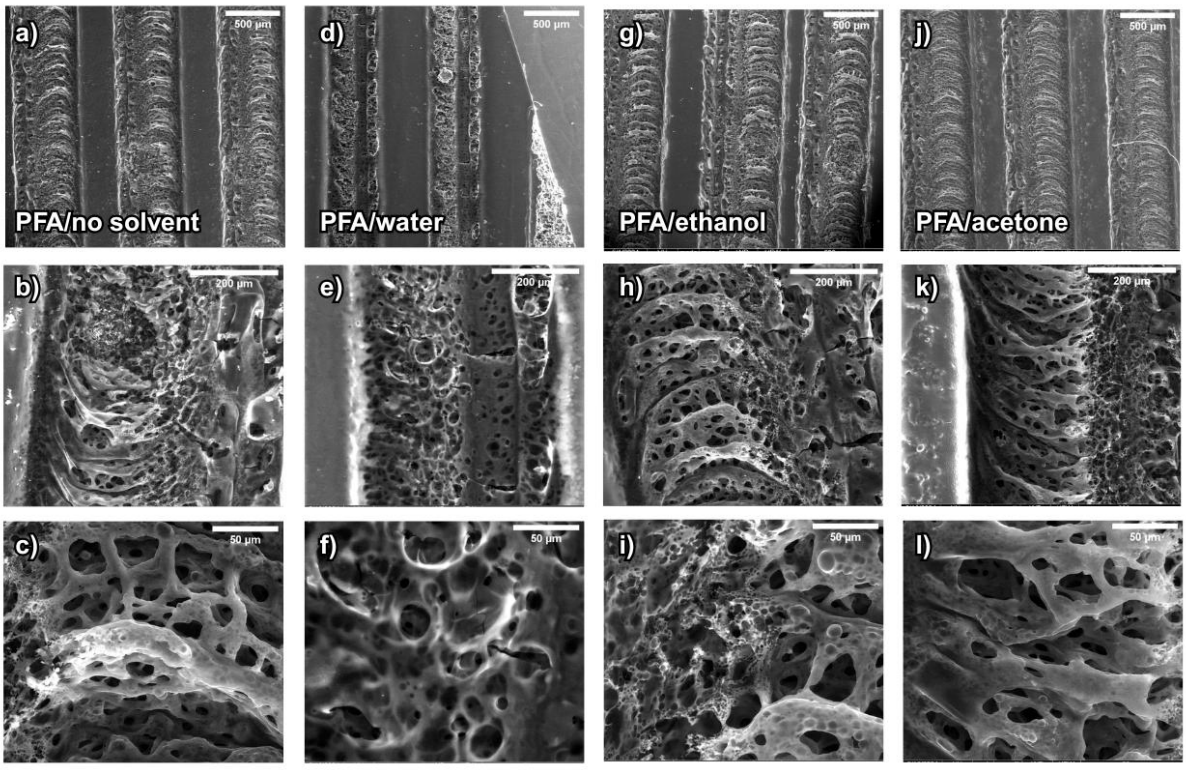


Figure 4.9. Top-down SEM images of LIC formed on PFA/solvent. (a-c) PFA/no solvent, (d-f) PFA/water, (g-i) PFA/ethanol, and (j-l) PFA/acetone. (a,d,g,j) are at 50x magnification, (b,e,h,k) are at 200x magnification, and (c,f,i,l) are at 600x magnification.

Raman spectra of the LIC formed on PFA/solvent again confirm the formation of carbonaceous material by the appearance of D and G peaks at 1360 cm^{-1} and 1590 cm^{-1} (Figure 4.10). The position of the G band again indicates that the LIC structure is between nanocrystalline graphite and amorphous carbon which is Stage 2 of the amorphization trajectory.[85] The G band position increased ~5 cm^{-1} from 1590 cm^{-1} as the laser power increased for LIC on PFA/no solvent, suggesting a systematic ordering at higher powers (Figure 4.11a). A similar increase in I_D/I_G with increasing laser power supports this (Figure 4.11b). LIC on PFA/water exhibited the opposite trend, with the G band generally decreasing in position at higher powers. The band position fluctuated significantly for LIC on PFA/ethanol, but exhibits a peak at 5.3 W. No clear trend was observed for the changes in the D band FWHM with different laser powers, but I_D/I_G was generally higher for the LIC formed beyond 5.5 W. For LIC on PFA/acetone, the G band position stayed constant. Similarly, the FWHM of the D band and I_D/I_G exhibited minimal fluctuation for the carbonized PFA/acetone. Carbonization was observed in the full range of laser powers and at both the lowest

power of 4.75 W and highest power of 5.65 W. Generally, the peaks are broad and overlapping, indicating that the LIC is more akin to glassy carbon than an ordered graphitic material. Furthermore, the 2D peak is not observed in any of the spectra despite being lased at an even wider range of powers compared to that in Section 4.2. This suggests that the PFA synthesized with various solvents (Section 2.2.2) is incapable of forming ordered graphitic carbon.

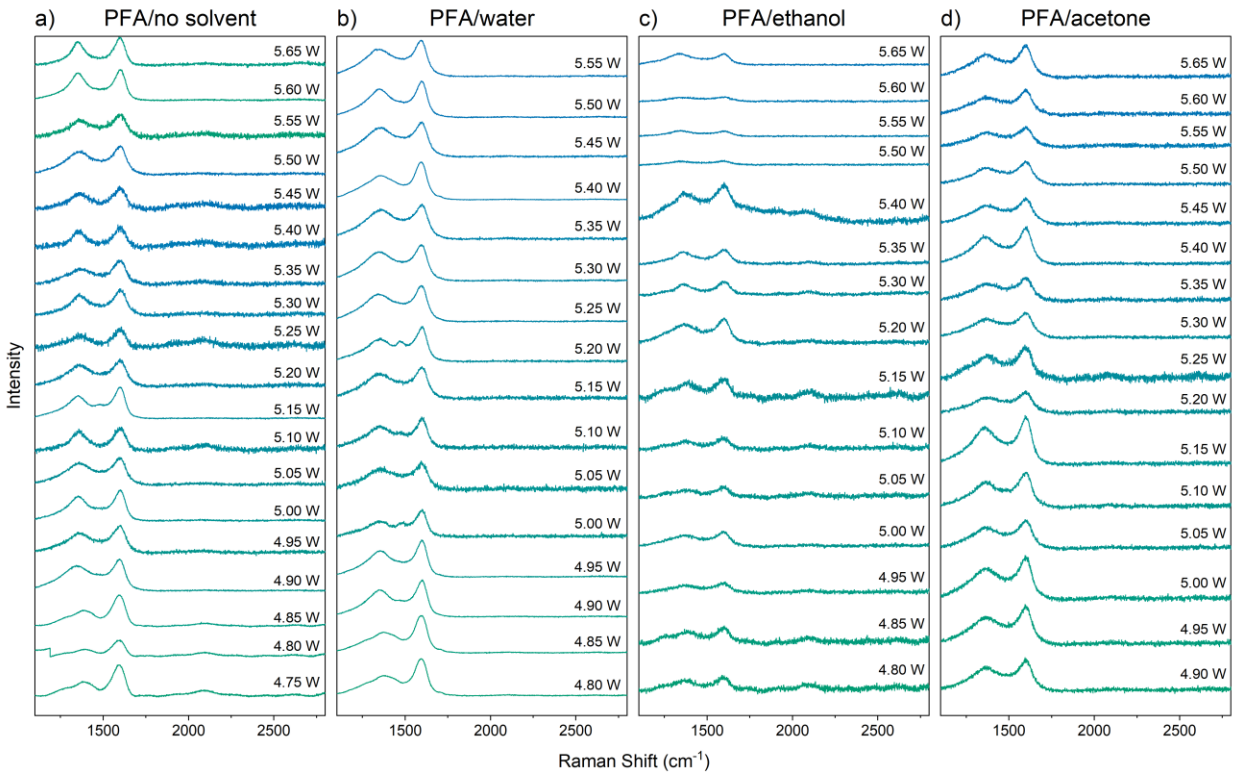


Figure 4.10. Raman spectra of LIC formed on (a) PFA/no solvent, (b) PFA/water, (c) PFA/ethanol, and (d) PFA/acetone with various laser powers.

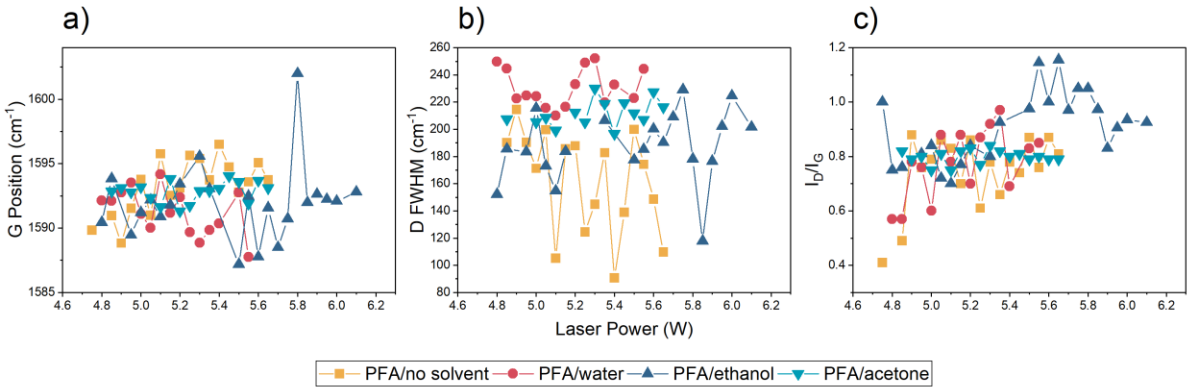


Figure 4.11. Raman analysis of LIC formed on PFA/solvent. Changes in (a) position of the G band, (b) FWHM of the D band, and (c) I_D/I_G across a range of laser powers.

The absence of a 2D band prevents determination of the optimal laser power with the same method as Section 4.2, and fluctuations in I_D/I_G make it impractical to select a single optimal power based on the highest ratio. Thus, to compare the LIC formed between the various precursors, the average value of each Raman metric across the range of laser powers was used (Figure 4.12). This method assesses the general ability of each precursor to form LIC and its resulting quality. The coefficient of variation for each metric did not exceed 25%. The most significant spread was observed for the position of the G band for LIC on PFA/ethanol, but other parameters varied within a reasonable range. LIC on PFA/acetone had the least deviation for all parameters, showing an unexpected resistance to variations induced by higher laser powers. On all precursors, the position of the G peak was around 1592 cm^{-1}. The widths of the D peaks were in the range of 160-240 cm^{-1}, which is characteristic for glassy carbon.[53] I_D/I_G ratios around 1 also indicate the more disordered nature of the carbon structure.[86]

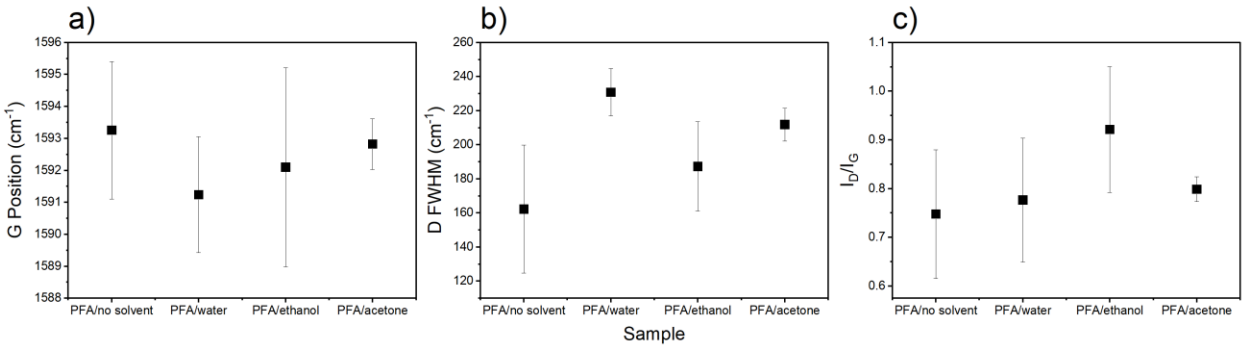


Figure 4.12. Averaged values of LIC metrics across the full range of laser powers. (a) Position of the G band, (b) FWHM of the D band, and (c) I_D/I_G of LIC on PFA/solvent. Error bars show the standard deviation.

LIC formed on PFA/solvent precursors varied in quality though a systematic effect on the degree of ordering was not observed (Figure A.4). An increased degree of polymerization, seen by increased intensity of the band at 1014 cm^{-1} in the FT-IR spectra, resulted in increased I_D/I_G. The G band position and FWHM of the D band were not systematically affected in a similar way (Figure 4.13a,d,g). The onset temperature of the second mass loss obtained from TGA, which describes the thermal stability of the precursor, had no noticeable effect on the I_D/I_G and D band FWHM. It did, however, increase the position of the G band (Figure 4.13b,e,h). Finally, a decrease in the position of the G band was observed with increasing ratio of ring opened motifs, though a trend in the D band FWHM and I_D/I_G is not observed (Figure 4.13c,f,i). Analysis of structural parameters of the LIC shows that the varied solvent systems studied here have no systematic effect on the quality of the LIC formed from the PFA/solvent precursors.

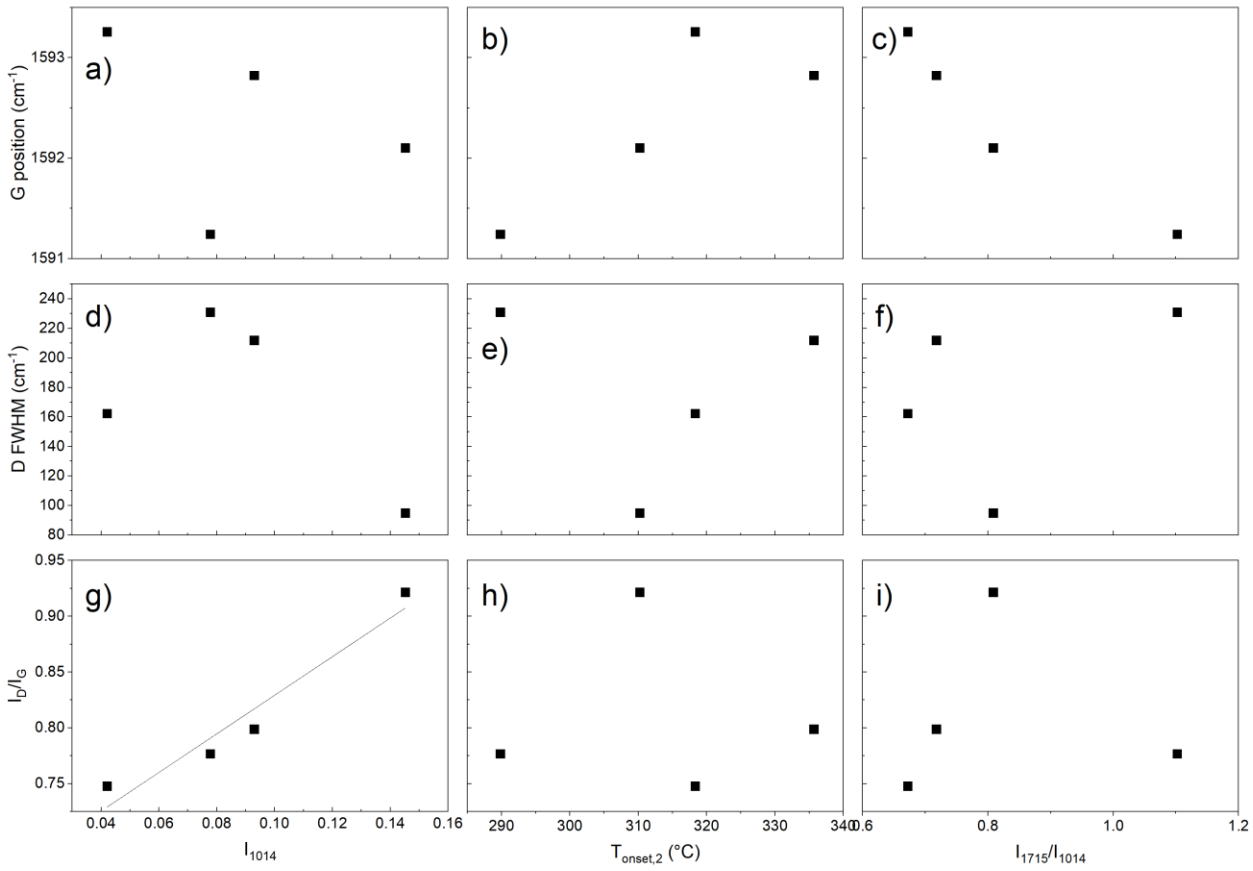


Figure 4.13. PFA/solvent structure correlation to LIC properties. Variations in (a-c) the position of the G band, (d-f) FWHM of the D band, and (g-i) I_D/I_G with changes in the PFA structure, including (a,d,g) the intensity of the 1014 cm^{-1} band from FT-IR indicating degree of polymerization, (b,e,h) the onset temperature of the second mass loss event from TGA, and (c,f,i) intensity ratio of the 1715 cm^{-1} and 1014 cm^{-1} bands from FT-IR.

This section has shown again that pristine PFA is a suitable precursor for laser-induced carbonization across a broad range of laser powers if glassy carbon is the desired material. ESEM imaging showed that the LIC formed has a fibrous morphology, but the laser powers used in this study were not sufficient for graphitization of any of the precursors, which is shown by evidence of ongoing release of gaseous products on the fibrous branches. Raman analysis of the LIC formed on each precursor shows that lasing forms glassy carbon with a low degree of order on all precursors. Structural analysis did not show systematic correlations between the degree of polymerization, ring opening, or thermal stability and the quality of LIC formed, though this series was overall unable to form highly ordered carbon.

4.4 LIC on PFA with Varied Alkanols

The morphologies of the LIC formed on the PFA/alkanol precursors were distinctly different from each other, as observed in the ESEM images (Figure 4.14). LIC on PFA/ethanol exhibited a similar fibrous, stringy structure to that observed in the previous sections, and appeared to be the most porous of the series. PFA/butanol formed LIC with a unique morphology that has not been previously observed. It appears thin with protruding tendrils, which arises from polymer ablation instead of carbonization.[17] The LIC formed on the remaining precursors exhibit similar structures, which are porous but flat. The overall morphology and pores of the LIC on these precursors are significantly smaller than that of PFA/ethanol and PFA/butanol. This type of morphology has not been observed in LIC formed on other polymer precursors.[21,77]

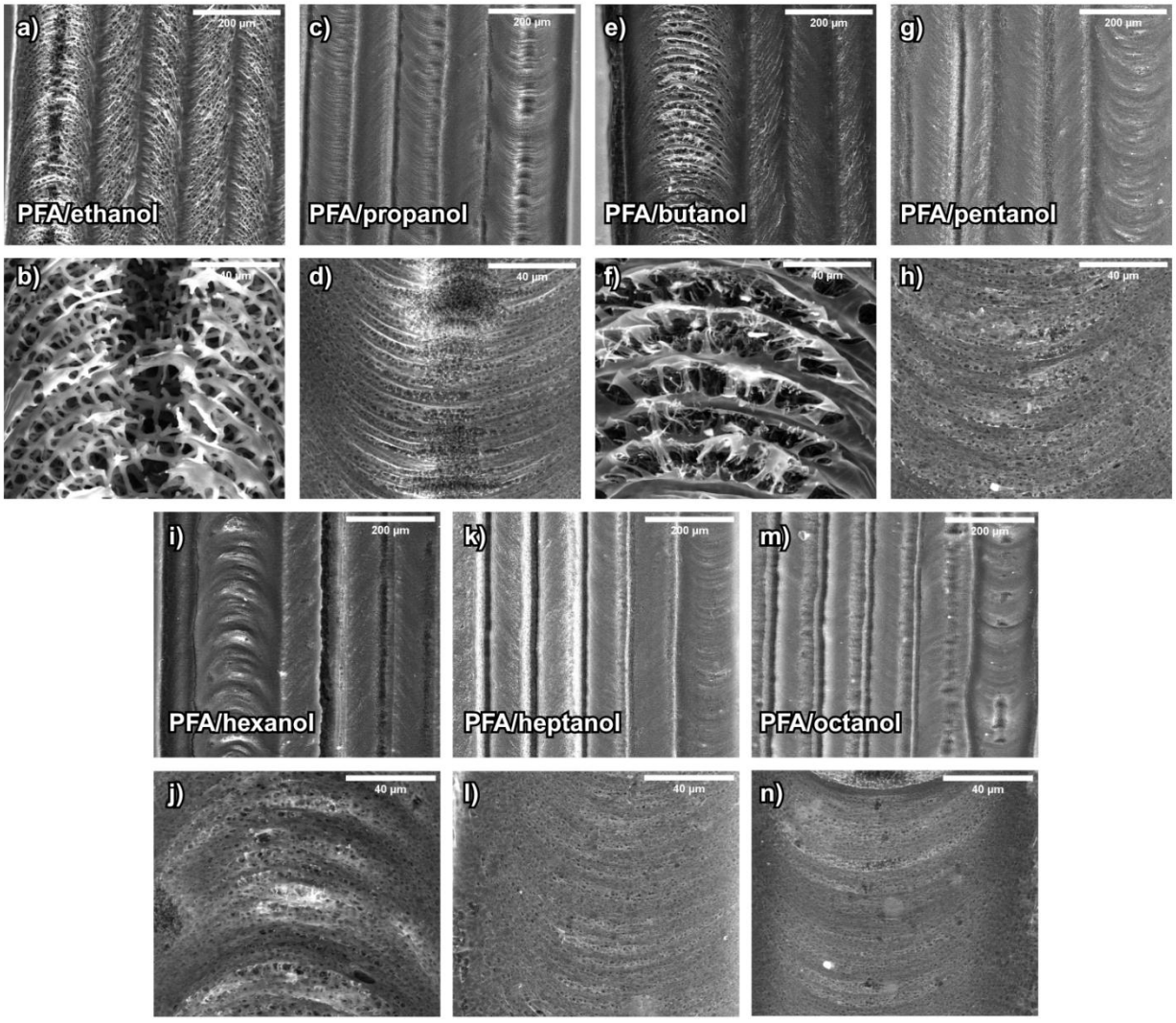


Figure 4.14. Top-down SEM images of LIC formed by the optimal laser power on (a-b) PFA/ethanol, (c-d) PFA/propanol, (e-f) PFA/butanol, (g-h) PFA/pentanol, (i-j) PFA/hexanol, (k-

l) PFA/heptanol, and (m-n) PFA/octanol. Images in the top row are at 200x magnification and images in the bottom row are at 1000x magnification.

Raman spectra of the LIC formed on the PFA/alcohol precursors show how the carbon structure was affected by the laser power (Figure 4.15). The observed D peaks are broad, appearing between 1350-1380 cm^{-1}. They overlap with the G peak, though to a lesser extent than observed in the previous two PFA series. Higher laser powers resulted in increased ordering, as evidenced by the gradual shifting of the G peak towards 1600 cm^{-1}. Extra bumps in the baseline appear for LIC formed by low laser powers from 1.35-1.5 W due to incomplete carbonization or partial ablation of the PFA. The precursors from PFA/ethanol to PFA/heptanol showed some carbonization starting at 1.35 or 1.4 W, but PFA/octanol required 1.5 W before the laser had any effect. The 2D peak appeared only at sufficiently high laser powers on all precursors except for PFA/ethanol. On the remaining precursors, laser powers above 1.55 W were required to form the 2D peak. On PFA/propanol, a wide breadth of laser powers resulted in a 2D peak, whereas only few laser powers formed this degree of ordered carbon on the other precursors.

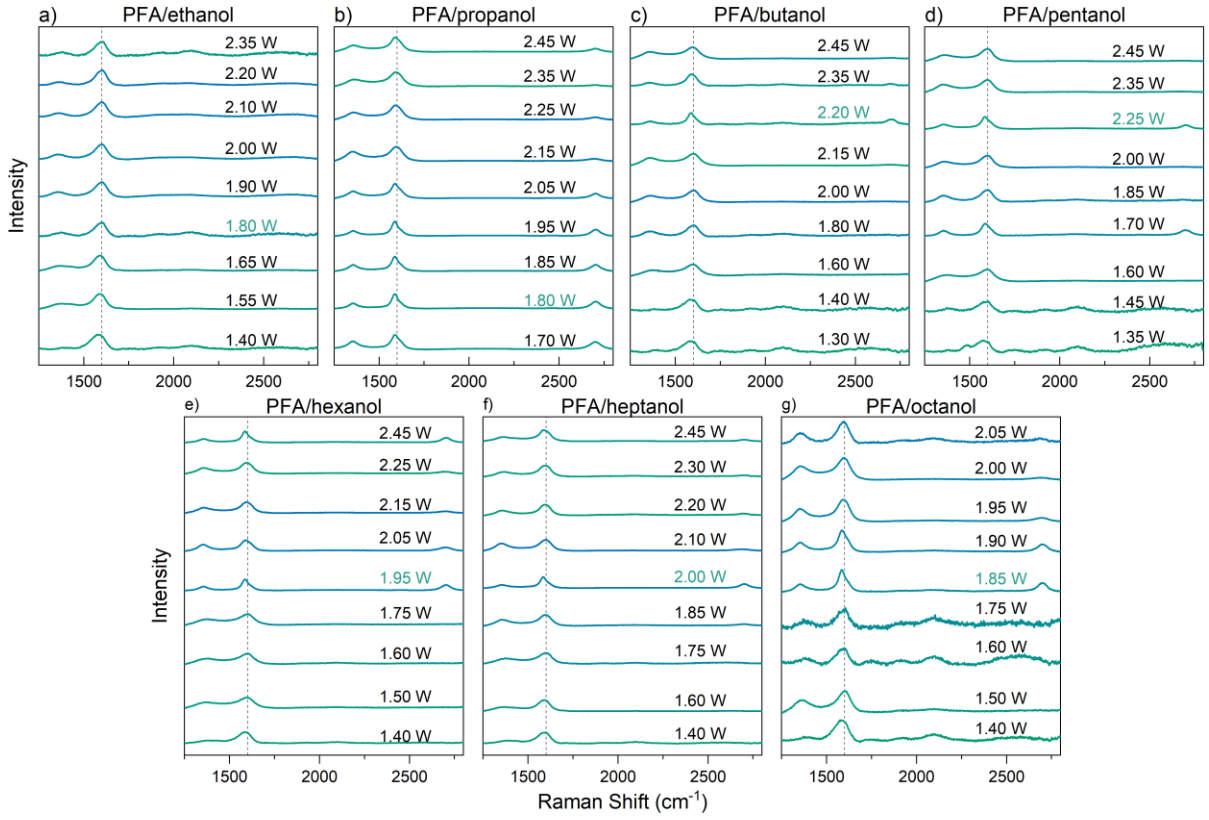


Figure 4.15. Raman spectra of LIC formed on PFA/alkanol at select laser powers. Spectra of LIC from (a) PFA/ethanol, (b) PFA/propanol, (c) PFA/butanol, (d) PFA/pentanol, (e) PFA/hexanol, (f)

PFA/heptanol, and (g) PFA/octanol with 1.30-2.45 W laser power. A dotted line at 1600 cm^{-1} shows the shift of the G band with increasing laser power.

Further analysis of the Raman peaks and how they evolve with increasing laser power exhibits the ordering trajectory of the LIC, the reverse of the amorphization trajectory described by Ferrari et al.[85] Changes in the G peak position and I_D/I_G for the LIC formed on PFA/propanol are shown as a function of laser power as an example in Figure 4.16. The position of the G band is lowest for the LIC formed at the lowest laser powers and increases until 1.65 W, corresponding to the second stage of the trajectory wherein more nanocrystalline graphitic domains begin to appear in the amorphous carbon. The same trend is observed for the I_D/I_G ratio. After 1.65 W, both parameters noticeably decrease, indicating entry into the first stage of the crystallization trajectory where the LIC structure becomes more graphitic. This is also supported by the first appearance of the 2D band at this power. Knowing the stage of the ordering trajectory that the LIC is in governs how the Raman parameters are used to assess the optimal LIC quality between different precursors.

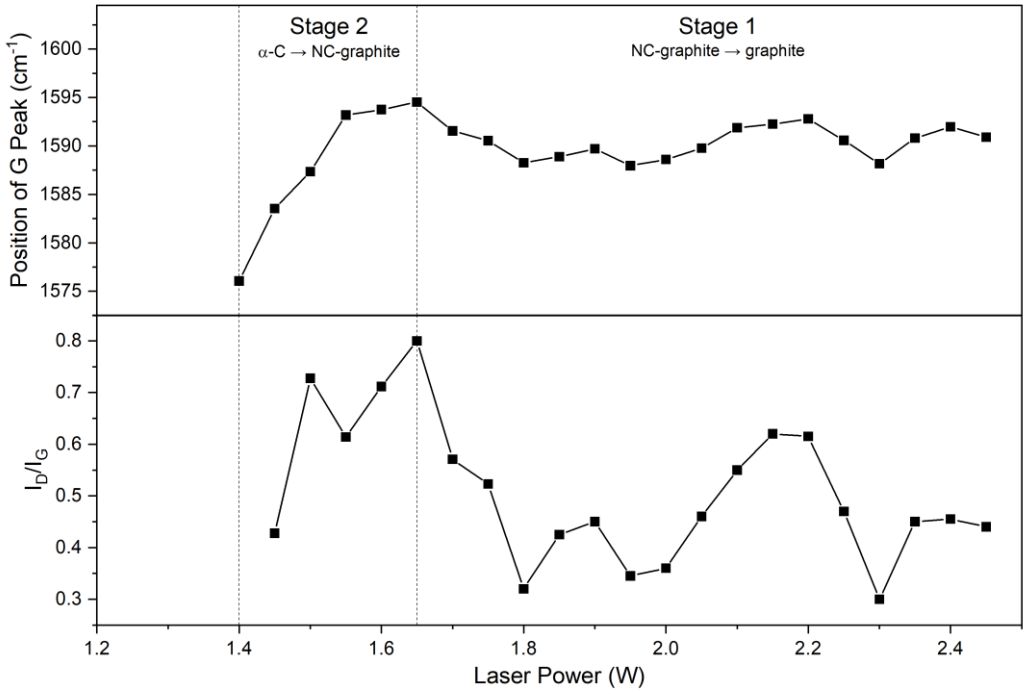


Figure 4.16. Ordering trajectory of the LIC on PFA/propanol demonstrated by the evolution of the G peak position and I_D/I_G ratio across the range of laser powers.

The optimal laser power for LIC formation on each precursor was determined by analyzing when the FWHM of the 2D band was at a minimum and I_{2D}/I_G was at a maximum (Figure 4.17).

This allows a comparison of the best LIC quality that can be formed on each precursor. An optimal power cannot be determined using this method for PFA/ethanol due to the absence of a 2D peak. However, since it was structurally similar to PFA/propanol (as seen from the FT-IR spectra and TGA data in Chapter 3), the optimal laser power for LIC formation on PFA/propanol is used for PFA/ethanol. The optimal LIC was formed on PFA/propanol with only 1.8 W of laser power, whereas the optimal laser powers for PFA/butanol and PFA/pentanol were significantly higher at 2.20 W and 2.25 W, respectively. The optimal powers for PFA/hexanol, PFA/heptanol, and PFA/octanol decreased to within 1.85-2.0 W (Figure 4.17h). Aside from PFA/ethanol, which was shown to not produce an ordered structure in this laser power range, the optimal LIC on each precursor falls within Stage 1 of the crystallization trajectory. Thus, to compare the quality of LIC formed on different precursors, low I_D/I_G, blue shifted G peaks, narrow FWHM of the D band, and high I_{2D}/I_G are considered desirable.

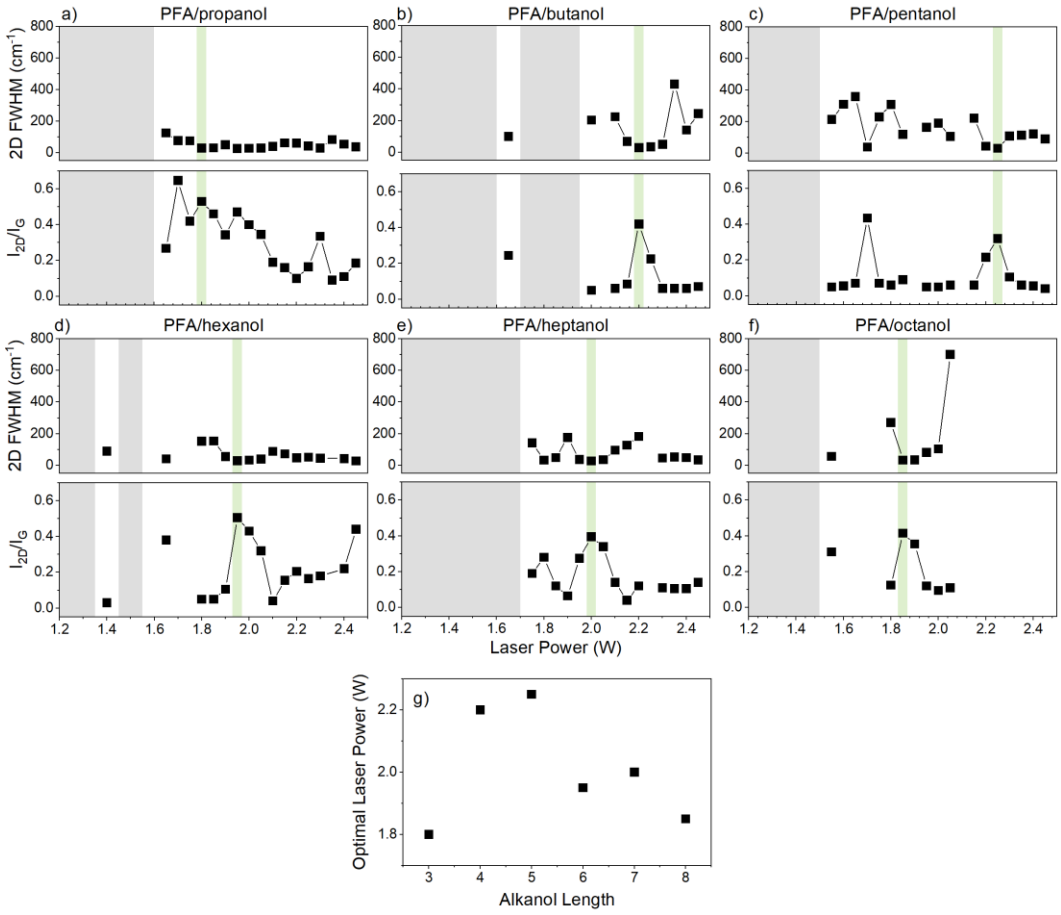


Figure 4.17. Analysis of the 2D band observed in the Raman spectra of the LIC formed on PFA/alcohol precursors to determine the optimal laser power for LIC formation. The laser powers

that induced the minimum FWHM of the 2D band and maximum I_{2D}/I_G on (a) PFA/propanol (1.8 W), (b) PFA/butanol (2.2 W), (c) PFA/pentanol (2.25 W), (d) PFA/hexanol (1.95 W), (e) PFA/heptanol (2.0 W), and (f) PFA/octanol (1.85 W) are highlighted in green. Laser powers that did not form 2D peaks are shaded grey. (g) Optimal laser power for LIC formation as a function of the alkanol length used in the precursor synthesis.

No clear trends were observed in the quality of the optimal LIC formed as the length of the alkanol used in the precursor synthesis increased (Figure 4.18). Each parameter – the position of the G peak, FWHM of the D peak, I_D/I_G, I_{2D}/I_G, and FWHM of the 2D peak – falls within the same range, suggesting that the quality of the best LIC on each precursor is comparable to one another, aside from PFA/ethanol which formed the poorest quality LIC of the series (Figure A.5).

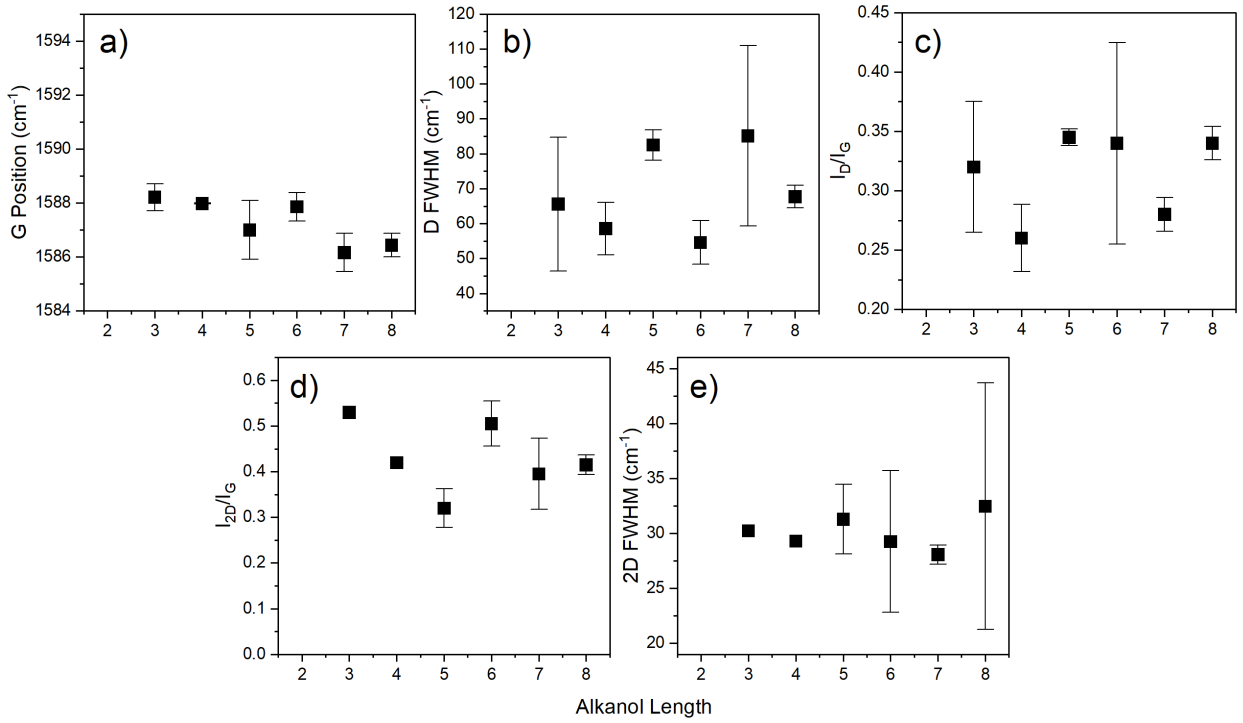


Figure 4.18. Raman parameters of the optimal LIC formed on each precursor. (a) Position of the G band, (b) FWHM of the D band, (c) I_D/I_G, (d) I_{2D}/I_G, and (e) FWHM of the 2D band of the LIC as a function of the alkanol length. Error bars show the standard deviation.

The influence of the PFA structure on LIC formation is investigated by correlating the thermal properties of the precursors to the Raman data obtained for the optimal LIC (Figure 4.19). No correlations were observed between the FT-IR structural analysis and LIC parameters (Figure A.6). The LIC quality did not change significantly with increased thermal stability. The position of the G peak was observed to stay within 1586 cm^{-1} to 1589 cm^{-1} with increasing thermal stability,

while the FWHM of the D band was within the range of 50-90 cm^{-1}. The I_D/I_G and I_{2D}/I_G ratios were similar between the samples, with average values of 0.31 ± 0.04 and 0.43 ± 0.08, respectively. The I_D/I_G ratio is lower and I_{2D}/I_G ratio is higher than those observed for glassy carbon obtained from pyrolyzed PFA, indicating that the LIC formed on the PFA/alcohol precursors is more ordered than pyrolytic GC.[52,53] It is also improved over previously formed LIC on PFA precursors,[26] though it remains to be investigated whether the difference is caused by structural variation in the PFA or differences in the operational methods of the laser instrument.

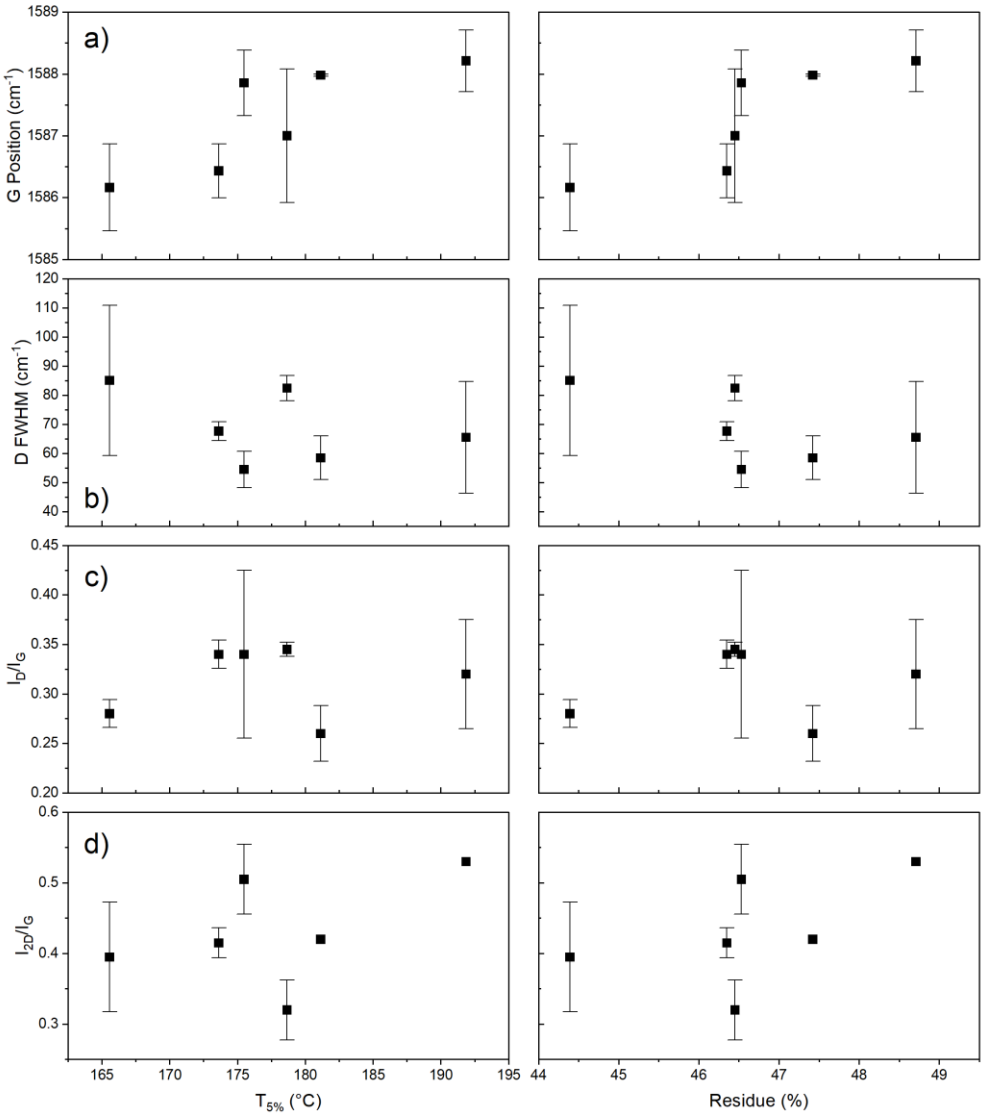


Figure 4.19. Analysis of Raman data with respect to thermal properties of the PFA/alcohol precursors. Changes in the (a) position of the G peak, (b) FWHM of the D peak, (c) I_D/I_G, and (d) I_{2D}/I_G as a function of $T_{5\%}$ and residue. Error bars show the standard deviation.

This section demonstrates that pristine PFA synthesized with varying lengths of alkanol is a suitable precursor for laser-induced carbonization. The small scale, porous morphology of the LIC formed on these precursors was notably different from that formed on the previous PFA series and from LIC formed on other precursors in literature. Subsequent Raman analysis of the LIC showed that the PFA/alkanol precursors could form a more ordered carbon material with the appearance of 2D bands and narrow peaks. The quality of the best LIC formed on each precursor was relatively similar, and so structural analysis could not elucidate clear correlations between the LIC and the precursor's thermal stability.

4.5 Discussion

For each series, the average Raman parameters of the optimal LIC formed on each PFA precursor was determined to compare the LIC across series, except for PFA/solvent where the parameters across the whole range of laser powers were averaged, similarly to its treatment in Section 4.3. Laser-induced carbonization of the three PFA series resulted in significant variations in the quality of LIC owing to the different preparation methods of each described in Chapter 3 (Figure 4.20). The LIC formed on each series fell on distinct points of the carbon ordering trajectory. PFA/solvent formed the most amorphous LIC, demonstrated by the absence of a 2D peak at any laser power in the tested range. Its broad D peak widths were 175 ± 61 cm^{-1}, along with intermediate values for the position of the G peak and I_D/I_G, which fall within Stage 2 of the ordering trajectory. LIC formed on PFA/acid concentration was between Stages 1 and 2, where the amorphous carbon structure contains more nanocrystalline graphitic domains. 2D peaks in the Raman spectra indicated a higher degree of ordering than LIC on PFA/solvent, and the narrow FWHM of the D peak around 66 ± 15 cm^{-1} and high I_D/I_G at 1.04 ± 0.18 are characteristic of the increased order of the carbon structure at this stage. Finally, the most ordered LIC was formed on PFA/alkanol, which was in Stage 1 of the ordering trajectory. 2D peaks were similarly observed in the optimal LIC and accompanied by narrow D peaks with widths similar to that on PFA/acid concentration, the G band positions ca. 1587 cm^{-1}, and the lowest I_D/I_G at 0.31 ± 0.04.

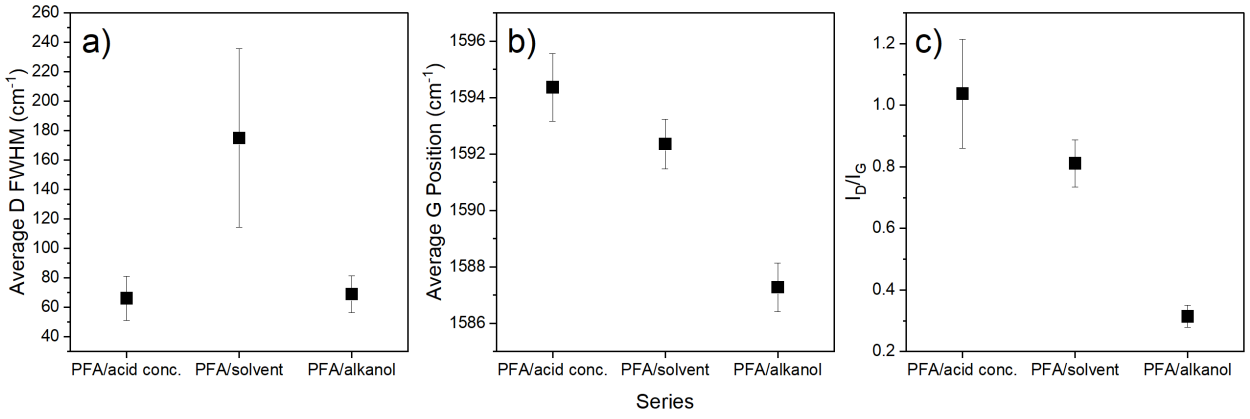


Figure 4.20. Average Raman parameters of the optimal LIC formed on each PFA series. (a) Average FWHM of the D peak, (b) average position of the G peak, and (c) average I_D/I_G of the optimal LIC of the PFA/acid concentration, PFA/solvent, and PFA/alkanol series. Error bars show the standard deviation.

The structures of each PFA series varied noticeably from each other, shown in Chapter 3, and this influenced the resulting LIC quality on each precursor though not systematically (Figure 4.21). Trends in the I_D/I_G ratio and position of the G peak were not observed as a function of the degree of polymerization, indicated by the FT-IR band at 1014 cm^{-1} (Figure 4.21a-b). PFA/acid concentration had the highest polymerization degree of the three series, but did not produce the most ordered LIC. However, increasing swell ratios and therefore decreased crosslinking density of the precursors resulted in lower I_D/I_G and a lower frequency G peak position, suggesting a more ordered structure (Figure 4.21c-d). Increased crosslinking density in polymers is known to prevent graphitization since the crosslinked bonds are maintained at higher temperatures, hindering the rearrangement of atoms into graphitic domains.[89,90] A more robust method for determining the crosslinking density of the PFA series is required to confirm this relationship. The PFA series with the highest thermal stability, reflected by the temperature $T_{infl,2}$ where the maximum mass loss during backbone degradation was observed, resulted in the most ordered LIC (Figure 4.21e-f). The other two series had similar $T_{infl,2}$ and accordingly, similar I_D/I_G ratios and G peak positions. However, the two series are notably different in the degree of order in the carbon structure, suggesting that the effect of thermal stability has a minor effect on the graphitizing ability of the precursors and that other factors are more influential in this regard.

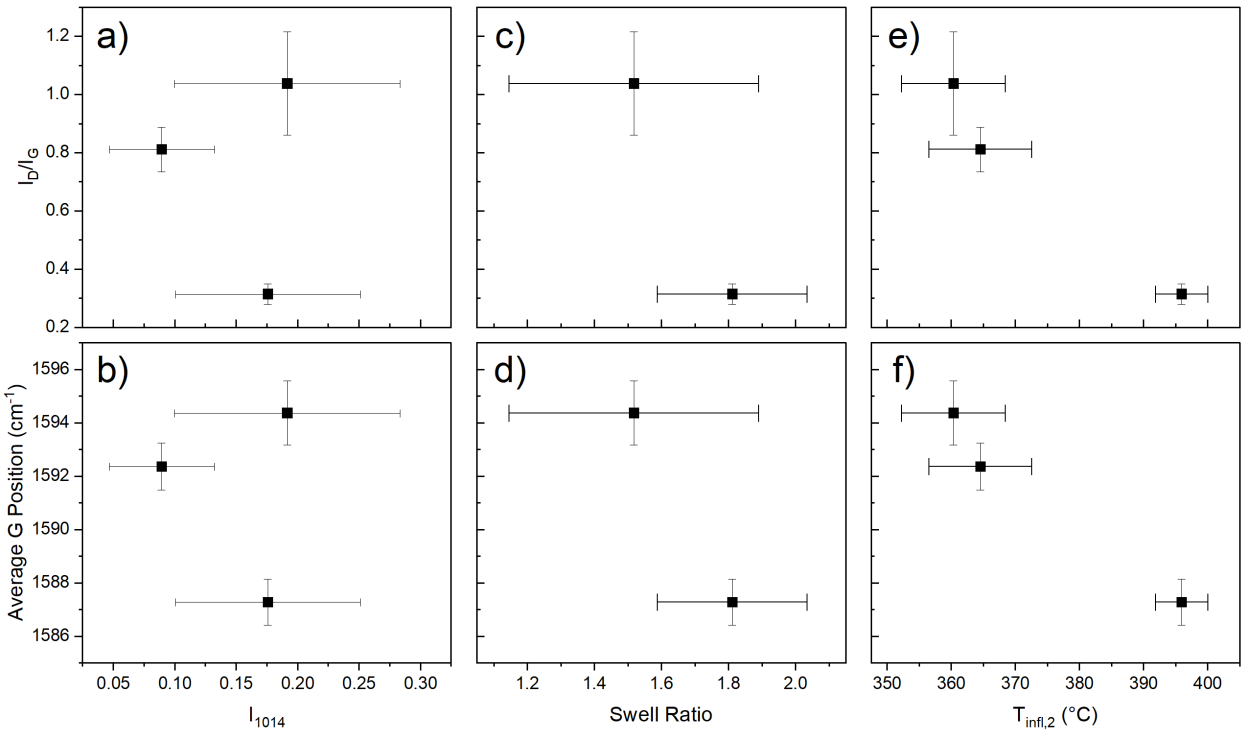


Figure 4.21. Average Raman parameters of the optimal LIC on each PFA series as a function of various PFA structure data. Changes in I_D/I_G and the average position of the G peak as a function of (a-b) the degree of polymerization, (c-d) swell ratio, and (e-f) temperature at which the maximum mass loss is observed during backbone degradation. Error bars show the standard deviation.

The structural analysis and its effect on the LIC quality reveals some insight on the precursor chemistry that would enable the laser-induced graphenization of PFA. The key features of the precursor series that formed the most ordered LIC were low crosslinking density and high thermal stability, suggesting that PFA comprised of more such qualities would be conducive for LIG formation. The temperature of maximum mass loss for Kapton, the most widely used LIG precursor, is between 500-600°C.[93,94] It is also not crosslinked.[95] This has been shown to be advantageous for LIG substrates, since a single laser pass can form LIG. However, other thermoset polymers such as phenolic resin and polystyrene were successfully converted into LIG through the multiple lasing technique after only forming an amorphous carbon upon a single lase.[25] Modifications to lasing parameters can thus also affect the LIC quality without changing the chemistry of the precursor, which could be the case with the PFA/alkanol series which was lased with a different type of laser than the other two series. Further investigation of both the structural influence of the precursor and lasing parameters is required.

4.6 Conclusion

Overall, investigation of the LIC on the three PFA series mainly demonstrated the potential of pristine PFA as a precursor for laser-induced carbonization. Glassy carbon was confirmed to form on all three series of precursors to varying degrees of order, with the PFA/alkanol precursors resulting in the highest quality LIC. However, unsystematic structural variations between precursors made it challenging to identify the structural motifs that enabled the formation of more ordered LIC. Trends were also not observed between the structures of the PFA/solvent samples and the resulting LIC, despite notable variation in the degree of ring opening between precursors. LIC formed on the PFA/acid concentration series, however, showed that decreased crosslinking could positively influence the ordering of carbon structure. Comparison of the LIC formed across the three series suggested that high thermal stability and low crosslinking density increase the order of the LIC structure that can form. PFA with minimal crosslinking and increased thermal stability, which would be similar to existing LIG precursors, would be ideal for LIG formation on PFA.

Chapter 5

Conclusions and Future Work

5.1 Conclusions

This work investigated the influence of the PFA structure on the quality of LIC that can form by varying synthetic conditions to target various structural features such as increased degree of polymerization, ring opened ketones, and crosslinking density. Increasing the concentration of the acid catalyst promoted the degree of polymerization, while the solvent in which the polymerization is performed can effectively increase the concentration of ring opened ketone structures along the backbone. The addition of progressively longer chain alkanols did not have a systematic effect on the structural motifs in the PFA backbone but significantly increased the thermal stability of PFA overall. With three PFA series comprising of different key features, their effects on LIC were investigated.

These variations in the structure and properties of PFA resulted in LIC with varying degrees of ordering as elucidated by Raman spectroscopy, ranging from mainly amorphous GC to significantly more ordered GC with more graphitic crystalline domains. PFA with the lowest crosslinking density and highest thermal stability formed the most ordered LIC, suggesting that a greater abundance of these features in PFA could enable the formation of LIG on an attractive, bio-based precursor. Typically, higher ordered GC on PFA can only be formed under high heat treatment temperatures with significantly higher defect density.[52] This work revealed that laser irradiation of PFA under ambient conditions with a CO_2 IR laser can form highly ordered GC with the potential for graphenization.

5.2 Future Work

Several avenues can be explored to further investigate and confirm the effect of PFA chemistry on LIC, starting with a more comprehensive collection of the different structural features PFA can adopt. More robust methods for crosslinking the PFA and subsequent characterization will reveal better insight on the effect of crosslinking density on carbonization, such as variations in curing time, the use of chemical crosslinkers, and a dynamic mechanical analyzer for characterization.[29,66,96] The conjugated structure can also be targeted, for example by the addition

of hydrogen peroxide to the polymerization, which subsequently increases the potential for the Diels-Alder crosslinking to occur.[63] A broader view of the PFA chemistry would allow stronger conclusions to be drawn on the effect of its structures on LIC quality.

Lasing parameters such as the laser wavelength, scan rate, and pulse duration are key contributors to LIC formation, though they were not the focus of this work. However, switching from a continuous-wave laser to a pulsed laser for the PFA/alkanol series likely had a significant impact on the resulting LIC, since shorter laser pulses increase the heat accumulation on the precursor. More photothermal energy is thus delivered to the precursor which facilitates graphitization.[21] Irradiation using this laser on the other two PFA series would reveal whether the chemical structure or fabrication method is the major contributor to LIC quality on polymer precursors.

References

(1) Novoselov, K. S.; Geim, A. K.; Morozov, S. V.; Jiang, D.; Zhang, Y.; Dubonos, S. V.; Grigorieva, I. V.; Firsov, A. A. Electric Field Effect in Atomically Thin Carbon Films. *Science* **2004**, *306* (5696), 666–669. https://doi.org/10.1126/science.1102896.

(2) Liao, L.; Peng, H.; Liu, Z. Chemistry Makes Graphene beyond Graphene. *Journal of the American Chemical Society* **2014**, *136* (35), 12194–12200. https://doi.org/10.1021/ja5048297.

(3) Manzeli, S.; Ovchinnikov, D.; Pasquier, D.; Yazyev, O. V.; Kis, A. 2D Transition Metal Dichalcogenides. *Nature Reviews Materials* **2017**, *2* (8), 1–15. https://doi.org/10.1038/natrevmats.2017.33.

(4) Geim, A. K. Graphene: Status and Prospects. *Science* **2009**, *324* (5934), 1530–1534. https://doi.org/10.1126/science.1158877.

(5) Geim, A. K.; Novoselov, K. S. The Rise of Graphene. *Nature Materials* **2007**, *6* (3), 183–191. https://doi.org/10.1038/nmat1849.

(6) Novoselov, K. S.; Mishchenko, A.; Carvalho, A.; Castro Neto, A. H. 2D Materials and van Der Waals Heterostructures. *Science* **2016**, *353* (6298), aac9439. https://doi.org/10.1126/science.aac9439.

(7) Gupta, A.; Sakthivel, T.; Seal, S. Recent Development in 2D Materials beyond Graphene. *Progress in Materials Science* **2015**, *73*, 44–126. https://doi.org/10.1016/j.pmatsci.2015.02.002.

(8) Ren, W.; Cheng, H.-M. The Global Growth of Graphene. *Nature Nanotechnology* **2014**, *9* (10), 726–730. https://doi.org/10.1038/nnano.2014.229.

(9) Avouris, P.; Dimitrakopoulos, C. Graphene: Synthesis and Applications. *Materials Today* **2012**, *15* (3), 86–97. https://doi.org/10.1016/S1369-7021(12)70044-5.

(10) Tiwari, S. K.; Sahoo, S.; Wang, N.; Huczko, A. Graphene Research and Their Outputs: Status and Prospect. *Journal of Science: Advanced Materials and Devices* **2020**, *5* (1), 10–29. https://doi.org/10.1016/j.jsamd.2020.01.006.

(11) Lin, L.; Peng, H.; Liu, Z. Synthesis Challenges for Graphene Industry. *Nature Materials* **2019**, *18* (6), 520–524. https://doi.org/10.1038/s41563-019-0341-4.

(12) Zurutuza, A.; Marinelli, C. Challenges and Opportunities in Graphene Commercialization. *Nature Nanotechnology* **2014**, *9* (10), 730–734. https://doi.org/10.1038/nnano.2014.225.

(13) Kong, W.; Kum, H.; Bae, S.-H.; Shim, J.; Kim, H.; Kong, L.; Meng, Y.; Wang, K.; Kim, C.; Kim, J. Path towards Graphene Commercialization from Lab to Market. *Nature Nanotechnology* **2019**, *14* (10), 927–938. https://doi.org/10.1038/s41565-019-0555-2.

(14) Kairi, M. I.; Dayou, S.; Kairi, N. I.; Bakar, S. A.; Vigolo, B.; Mohamed, A. R. Toward High Production of Graphene Flakes – a Review on Recent Developments in Their Synthesis Methods and Scalability. *Journal of Materials Chemistry A* **2018**, *6* (31), 15010–15026. https://doi.org/10.1039/C8TA04255A.

(15) Lin, J.; Peng, Z.; Liu, Y.; Ruiz-Zepeda, F.; Ye, R.; Samuel, E. L. G.; Yacaman, M. J.; Yakobson, B. I.; Tour, J. M. Laser-Induced Porous Graphene Films from Commercial Polymers. *Nature Communications* **2014**, *5* (1), 5714. https://doi.org/10.1038/ncomms6714.

(16) Ye, R.; James, D. K.; Tour, J. M. Laser-Induced Graphene: From Discovery to Translation. *Advanced Materials* **2019**, *31* (1), 1803621. https://doi.org/10.1002/adma.201803621.

(17) Lamberti, A.; Serrapede, M.; Ferraro, G.; Fontana, M.; Perrucci, F.; Bianco, S.; Chiolerio, A.; Bocchini, S. All-SPEEK Flexible Supercapacitor Exploiting Laser-Induced

Graphenization. *2D Materials* **2017**, *4* (3), 035012. https://doi.org/10.1088/2053-1583/aa790e.
(18) Garland, N. T.; McLamore, E. S.; Cavallaro, N. D.; Mendivelso-Perez, D.; Smith, E. A.; Jing, D.; Claussen, J. C. Flexible Laser-Induced Graphene for Nitrogen Sensing in Soil. *ACS Applied Materials & Interfaces* **2018**, *10* (45), 39124–39133. https://doi.org/10.1021/acsami.8b10991.
(19) Lamberti, A.; Perrucci, F.; Caprioli, M.; Serrapede, M.; Fontana, M.; Bianco, S.; Ferrero, S.; Tresso, E. New Insights on Laser-Induced Graphene Electrodes for Flexible Supercapacitors: Tunable Morphology and Physical Properties. *Nanotechnology* **2017**, *28* (17), 174002. https://doi.org/10.1088/1361-6528/aa6615.
(20) Imbrogno, A.; Islam, J.; Santillo, C.; Castaldo, R.; Sygellou, L.; Larrigy, C.; Murray, R.; Vaughan, E.; Hoque, Md. K.; Quinn, A. J.; Iacopino, D. Laser-Induced Graphene Supercapacitors by Direct Laser Writing of Cork Natural Substrates. *ACS Applied Electronic Materials* **2022**, *4* (4), 1541–1551. https://doi.org/10.1021/acsaelm.1c01202.
(21) Le, T.-S. D.; Phan, H.-P.; Kwon, S.; Park, S.; Jung, Y.; Min, J.; Chun, B. J.; Yoon, H.; Ko, S. H.; Kim, S.-W.; Kim, Y.-J. Recent Advances in Laser-Induced Graphene: Mechanism, Fabrication, Properties, and Applications in Flexible Electronics. *Advanced Functional Materials* **2022**, *32* (48), 2205158. https://doi.org/10.1002/adfm.202205158.
(22) Vashisth, A.; Kowalik, M.; Gerringer, J. C.; Ashraf, C.; van Duin, A. C. T.; Green, M. J. ReaxFF Simulations of Laser-Induced Graphene (LIG) Formation for Multifunctional Polymer Nanocomposites. *ACS Applied Nano Materials* **2020**, *3* (2), 1881–1890. https://doi.org/10.1021/acsanm.9b02524.
(23) C. Claro, P. I.; Pinheiro, T.; Silvestre, S. L.; Marques, A. C.; Coelho, J.; Marconcini, J. M.; Fortunato, E.; C. Mattoso, L. H.; Martins, R. Sustainable Carbon Sources for Green Laser-Induced Graphene: A Perspective on Fundamental Principles, Applications, and Challenges. *Applied Physics Reviews* **2022**, *9* (4), 041305. https://doi.org/10.1063/5.0100785.
(24) Singh, S. P.; Li, Y.; Zhang, J.; Tour, J. M.; Arnusch, C. J. Sulfur-Doped Laser-Induced Porous Graphene Derived from Polysulfone-Class Polymers and Membranes. *ACS Nano* **2018**, *12* (1), 289–297. https://doi.org/10.1021/acsnano.7b06263.
(25) Chyan, Y.; Ye, R.; Li, Y.; Singh, S. P.; Arnusch, C. J.; Tour, J. M. Laser-Induced Graphene by Multiple Lasing: Toward Electronics on Cloth, Paper, and Food. *ACS Nano* **2018**, *12* (3), 2176–2183. https://doi.org/10.1021/acsnano.7b08539.
(26) Hawes, G. F.; Yilman, D.; Noremberg, B. S.; Pope, M. A. Supercapacitors Fabricated via Laser-Induced Carbonization of Biomass-Derived Poly(Furfuryl Alcohol)/Graphene Oxide Composites. *ACS Applied Nano Materials* **2019**, *2* (10), 6312–6324. https://doi.org/10.1021/acsanm.9b01284.
(27) Hawes, G. F.; Verma, P.; Uceda, M.; Karimi, G.; Noremberg, B. S.; Pope, M. A. Salt-Induced Doping and Templating of Laser-Induced Graphene Supercapacitors. *Acs Applied Materials & Interfaces* **2023**, *15* (8), 10570–10584. https://doi.org/10.1021/acsami.2c17476.
(28) Origo, F. D.; Arisseto, J. C.; Seixas, F. L.; Miyakawa, W.; Damião, A. J.; Oishi, S. S.; Botelho, E. C. Acid Catalyst Influence on the Polymerization Time of Polyfurfuryl Alcohol and on the Porosity of Monolithic Vitreous Carbon. *Journal of Applied Polymer Science* **2016**, *133* (20). https://doi.org/10.1002/app.43272.
(29) Marefat Seyedlar, R.; Imani, M.; Mirabedini, S. M. Rheokinetics in Curing Process of Polyfurfuryl Alcohol: Effect of Homologous Acid Catalysts. *Iranian Polymer Journal* **2017**, *26* (4), 281–293. https://doi.org/10.1007/s13726-017-0518-0.

(30) Kim, T.; Assary, R. S.; Kim, H.; Marshall, C. L.; Gosztola, D. J.; Curtiss, L. A.; Stair, P. C. Effects of Solvent on the Furfuryl Alcohol Polymerization Reaction: UV Raman Spectroscopy Study. *Catalysis Today* **2013**, *205*, 60–66. https://doi.org/10.1016/j.cattod.2012.09.033.
(31) Oishi, S. S.; Rezende, M. C.; Origo, F. D.; Damião, A. J.; Botelho, E. C. Viscosity, pH, and Moisture Effect in the Porosity of Poly(Furfuryl Alcohol). *Journal of Applied Polymer Science* **2013**, *128* (3), 1680–1686. https://doi.org/10.1002/app.38332.
(32) Yin, J.; Zhang, A.; Liew, K. Y.; Wu, L. Synthesis of Poly(Ether Ether Ketone) Assisted by Microwave Irradiation and Its Characterization. *Polymer Bulletin* **2008**, *61* (2), 157–163. https://doi.org/10.1007/s00289-008-0942-6.
(33) Sysel, P.; Kulhánková, H.; Weinertová, K. Polyimides Prepared without the Use of Toxic Amidic Solvents. *Journal of Polymer Research* **2020**, *27* (8), 227. https://doi.org/10.1007/s10965-020-02177-3.
(34) Ye, R.; Chyan, Y.; Zhang, J.; Li, Y.; Han, X.; Kittrell, C.; Tour, J. M. Laser-Induced Graphene Formation on Wood. *Advanced Materials* **2017**, *29* (37), 1702211. https://doi.org/10.1002/adma.201702211.
(35) Qu, W.; Zhao, Z.; Wang, J.; Dong, F.; Xu, H.; Sun, X.; Jin, H. Direct Laser Writing of Pure Lignin on Carbon Cloth for Highly Flexible Supercapacitors with Enhanced Areal Capacitance. *Sustainable Energy & Fuels* **2021**, *5* (14), 3744–3754. https://doi.org/10.1039/D1SE00828E.
(36) Shindo, A.; Izumino, K. Structural Variation during Pyrolysis of Furfuryl Alcohol and Furfural-Furfuryl Alcohol Resins. *Carbon* **1994**, *32* (7), 1233–1243. https://doi.org/10.1016/0008-6223(94)90107-4.
(37) Fitzer, E.; Schaefer, W.; Yamada, S. The Formation of Glasslike Carbon by Pyrolysis of Polyfurfuryl Alcohol and Phenolic Resin. *Carbon* **1969**, *7* (6), 643–648. https://doi.org/10.1016/0008-6223(69)90518-1.
(38) Burket, C. L.; Rajagopalan, R.; Marencic, A. P.; Dronvajjala, K.; Foley, H. C. Genesis of Porosity in Polyfurfuryl Alcohol Derived Nanoporous Carbon. *Carbon* **2006**, *44* (14), 2957–2963. https://doi.org/10.1016/j.carbon.2006.05.029.
(39) Conley, R. T.; Metil, I. An Investigation of the Structure of Furfuryl Alcohol Polycondensates with Infrared Spectroscopy. *Journal of Applied Polymer Science* **1963**, *7* (1), 37–52. https://doi.org/10.1002/app.1963.070070104.
(40) Barr, J. B.; Wallon, S. B. The Chemistry of Furfuryl Alcohol Resins. *Journal of Applied Polymer Science* **1971**, *15* (5), 1079–1090. https://doi.org/10.1002/app.1971.070150504.
(41) Schmitt, C. R. Polyfurfuryl Alcohol Resins. *Polymer-Plastics Technology and Engineering* **1974**, *3* (2), 121–158. https://doi.org/10.1080/03602557408545025.
(42) He, L.; Li, D.; Zhang, G.; Webley, P. A.; Zhao, D.; Wang, H. Synthesis of Carbonaceous Poly(Furfuryl Alcohol) Membrane for Water Desalination. *Industrial & Engineering Chemistry Research* **2010**, *49* (9), 4175–4180. https://doi.org/10.1021/ie901886c.
(43) Men, X. H.; Zhang, Z. Z.; Song, H. J.; Wang, K.; Jiang, W. Functionalization of Carbon Nanotubes to Improve the Tribological Properties of Poly(Furfuryl Alcohol) Composite Coatings. *Composites Science and Technology* **2008**, *68* (3), 1042–1049. https://doi.org/10.1016/j.compscitech.2007.07.008.
(44) Liu, J.; Wang, H.; Cheng, S.; Chan, K.-Y. Nafion–Polyfurfuryl Alcohol Nanocomposite Membranes for Direct Methanol Fuel Cells. *Journal of Membrane Science* **2005**, *246* (1), 95–101. https://doi.org/10.1016/j.memsci.2004.08.016.

(45) Wang, H.; Yao, J. Use of Poly(Furfuryl Alcohol) in the Fabrication of Nanostructured Carbons and Nanocomposites. *Industrial & Engineering Chemistry Research* **2006**, *45* (19), 6393–6404. https://doi.org/10.1021/ie0602660.
(46) Pascault, J.-P.; Williams, R. J. J. Thermosetting Polymers. In *Handbook of Polymer Synthesis, Characterization, and Processing*; John Wiley & Sons, Ltd, 2013; pp 519–533. https://doi.org/10.1002/9781118480793.ch28.
(47) Dunlop, A. P.; Peters, F. N. The Nature of Furfuryl Alcohol. *Industrial & Engineering Chemistry* **1942**, *34* (7), 814–817. https://doi.org/10.1021/ie50391a010.
(48) Choura, M.; Belgacem, N. M.; Gandini, A. Acid-Catalyzed Polycondensation of Furfuryl Alcohol: Mechanisms of Chromophore Formation and Cross-Linking. *Macromolecules* **1996**, *29* (11), 3839–3850. https://doi.org/10.1021/ma951522f.
(49) Tondi, G.; Cefarin, N.; Sepperer, T.; D'Amico, F.; Berger, R. J. F.; Musso, M.; Birarda, G.; Reyer, A.; Schnabel, T.; Vaccari, L. Understanding the Polymerization of Polyfurfuryl Alcohol: Ring Opening and Diels-Alder Reactions. *Polymers* **2019**, *11* (12), 2126. https://doi.org/10.3390/polym11122126.
(50) D'Amico, F.; Musso, M. E.; Berger, R. J. F.; Cefarin, N.; Birarda, G.; Tondi, G.; Bertoldo Menezes, D.; Reyer, A.; Scarabattoli, L.; Sepperer, T.; Schnabel, T.; Vaccari, L. Chemical Constitution of Polyfurfuryl Alcohol Investigated by FTIR and Resonant Raman Spectroscopy. *Spectrochimica Acta Part A: Molecular and Biomolecular Spectroscopy* **2021**, *262*, 120090. https://doi.org/10.1016/j.saa.2021.120090.
(51) Manocha, L. M. The Effect of Heat Treatment Temperature on the Properties of Polyfurfuryl Alcohol Based Carbon-Carbon Composites. *Carbon* **1994**, *32* (2), 213–223. https://doi.org/10.1016/0008-6223(94)90185-6.
(52) Jurkiewicz, K.; Pawlyta, M.; Zygadło, D.; Chrobak, D.; Duber, S.; Wrzalik, R.; Ratuszna, A.; Burian, A. Evolution of Glassy Carbon under Heat Treatment: Correlation Structure–Mechanical Properties. *Journal of Materials Science* **2018**, *53* (5), 3509–3523. https://doi.org/10.1007/s10853-017-1753-7.
(53) Cheng, L.-T.; Tseng, W. J. Effect of Acid Treatment on Structure and Morphology of Carbons Prepared from Pyrolysis of Polyfurfuryl Alcohol. *Journal of Polymer Research* **2010**, *17* (3), 391–399. https://doi.org/10.1007/s10965-009-9325-4.
(54) Fitzer, E.; Schäfer, W. The Effect of Crosslinking on the Formation of Glasslike Carbons from Thermosetting Resins. *Carbon* **1970**, *8* (3), 353–364. https://doi.org/10.1016/0008-6223(70)90075-8.
(55) Wang, Z.; Lu, Z.; Huang, X.; Xue, R.; Chen, L. Chemical and Crystalline Structure Characterizations of Polyfurfuryl Alcohol Pyrolyzed at 600 °C. *Carbon* **1998**, *36* (1), 51–59. https://doi.org/10.1016/S0008-6223(97)00150-4.
(56) Nakamizo, M.; Kammereck, R.; Walker, P. L. Laser Raman Studies on Carbons. *Carbon* **1974**, *12*, 259–267. https://doi.org/10.1016/0008-6223(74)90068-2.
(57) Maryott, A. A.; Smith, E. R. *Table of Dielectric Constants of Pure Liquids*; U.S. Government Printing Office, 1951.
(58) Mark, J. E. *Physical Properties of Polymers Handbook*, 2nd ed.; Springer: New York, 2007.
(59) Flory, P. J.; Rehner, J. Statistical Mechanics of Cross-Linked Polymer Networks II. Swelling. *The Journal of Chemical Physics* **1943**, *11* (11), 521–526. https://doi.org/10.1063/1.1723792.
(60) Guigo, N.; Mija, A.; Vincent, L.; Sbirrazzuoli, N. Chemorheological Analysis and Model-Free Kinetics of Acid Catalysed Furfuryl Alcohol Polymerization. *Physical Chemistry Chemical Physics* **2007**, *9* (39), 5359–5366. https://doi.org/10.1039/B707950H.

(61) Marefat Seyedlar, R.; Imani, M.; Mirabedini, S. M. Curing of Polyfurfuryl Alcohol Resin Catalyzed by a Homologous Series of Dicarboxylic Acid Catalysts. II. Swelling Behavior and Thermal Properties. *Journal of Applied Polymer Science* **2018**, *135* (5), 45770. https://doi.org/10.1002/app.45770.
(62) Sadler, J. M.; Yeh, I.-C.; Toulan, F. R.; McAninch, I. M.; Rinderspacher, B. C.; La Scala, J. J. Kinetics Studies and Characterization of Poly(Furfuryl Alcohol) for Use as Bio-Based Furan Novolacs. *Journal of Applied Polymer Science* **2018**, *135* (34), 46608. https://doi.org/10.1002/app.46608.
(63) Shibutani, K.; Nakai, J.; Aphichartsuphapkhajorn, K.; Kayaki, Y.; Kuwata, S.; Arao, Y.; Kubouchi, M. The Activation of Furfuryl Alcohol Polymerization by Oxygen and Its Enhanced Mechanical Properties. *Journal of Applied Polymer Science* **2021**, *138* (17), 50311. https://doi.org/10.1002/app.50311.
(64) He, L.; Li, D.; Dong, D.; Yao, J.; Huang, Y.; Wang, H. Effects of Polymerization Conditions on the Properties of Poly(Furfuryl Alcohol) Composite Membranes. *Journal of Applied Polymer Science* **2012**, *124* (4), 3383–3391. https://doi.org/10.1002/app.35356.
(65) Cesano, F.; Scarano, D.; Bertarione, S.; Bonino, F.; Damin, A.; Bordiga, S.; Prestipino, C.; Lamberti, C.; Zecchina, A. Synthesis of ZnO–Carbon Composites and Imprinted Carbon by the Pyrolysis of ZnCl2-Catalyzed Furfuryl Alcohol Polymers. *Journal of Photochemistry and Photobiology A: Chemistry* **2008**, *196* (2), 143–153. https://doi.org/10.1016/j.jphotochem.2007.07.033.
(66) Falco, G.; Guigo, N.; Vincent, L.; Sbirrazzuoli, N. Opening Furan for Tailoring Properties of Bio-Based Poly(Furfuryl Alcohol) Thermoset. *ChemSusChem* **2018**, *11* (11), 1805–1812. https://doi.org/10.1002/cssc.201800620.
(67) Barsberg, S.; Thygesen, L. G. Poly(Furfuryl Alcohol) Formation in Neat Furfuryl Alcohol and in Cymene Studied by ATR-IR Spectroscopy and Density Functional Theory (B3LYP) Prediction of Vibrational Bands. *Vibrational Spectroscopy* **2009**, *49* (1), 52–63. https://doi.org/10.1016/j.vibspec.2008.04.013.
(68) Lange, J.-P.; van de Graaf, W. D.; Haan, R. J. Conversion of Furfuryl Alcohol into Ethyl Levulinate Using Solid Acid Catalysts. *ChemSusChem* **2009**, *2* (5), 437–441. https://doi.org/10.1002/cssc.200800216.
(69) Varganici, C.-D.; Rosu, D.; Barbu-Mic, C.; Rosu, L.; Popovici, D.; Hulubei, C.; Simionescu, B. C. On the Thermal Stability of Some Aromatic-Aliphatic Polyimides. *Journal of Analytical and Applied Pyrolysis* **2015**, *113*, 390–401. https://doi.org/10.1016/j.jaap.2015.02.031.
(70) Witkowski, A.; Stec, A. A.; Hull, T. R. Thermal Decomposition of Polymeric Materials. In *SFPE Handbook of Fire Protection Engineering*; Hurley, M. J., Gottuk, D., Hall, J. R., Harada, K., Kuligowski, E., Puchovsky, M., Torero, J., Watts, J. M., Wieczorek, C., Eds.; Springer New York: New York, NY, 2016; pp 167–254. https://doi.org/10.1007/978-1-4939-2565-0_7.
(71) Kim, S.; Chen, J.; Cheng, T.; Gindulyte, A.; He, J.; He, S.; Li, Q.; Shoemaker, B. A.; Thiessen, P. A.; Yu, B.; Zaslavsky, L.; Zhang, J.; Bolton, E. E. PubChem 2025 Update. *Nucleic Acids Research* **2025**, *53* (D1), D1516–D1525. https://doi.org/10.1093/nar/gkae1059.
(72) Triwulandari, E.; Fatriasari, W.; Iswanto, A. H.; Septiyanti, M.; Umam, E. F.; Ghozali, M. Effect of Reaction Time on the Molecular Weight Distribution of Polyurethane Modified Epoxy and Its Properties. *Journal of Materials Research and Technology* **2022**, *19*, 2204–2214. https://doi.org/10.1016/j.jmrt.2022.05.185.

(73) Lin, Q.; Lim, J. Y. C.; Xue, K.; Chee, C. P. T.; Loh, X. J. Supramolecular Thermogels from Branched PCL-Containing Polyurethanes. *RSC Advances* **2020**, *10* (64), 39109–39120. https://doi.org/10.1039/D0RA07426H.
(74) Haynes, W. M. *CRC Handbook of Chemistry and Physics*, 97th ed.; CRC Press: Boca Raton, 2016. https://doi.org/10.1201/9781315380476.
(75) Wade, L. G. *Organic Chemistry*, 8th ed.; Pearson: Boston, Massachussetts, 2013.
(76) Origo, F. D.; Arisseto, J. C.; Seixas, F. L.; Miyakawa, W.; Damião, A. J.; Oishi, S. S.; Botelho, E. C. Acid Catalyst Influence on the Polymerization Time of Polyfurfuryl Alcohol and on the Porosity of Monolithic Vitreous Carbon. *Journal of Applied Polymer Science* **2016**, *133* (20). https://doi.org/10.1002/app.43272.
(77) Bai, S.; Ruan, L.; Chen, H.; Du, Y.; Deng, H.; Dai, N.; Tang, Y. Laser-Induced Graphene: Carbon Precursors, Fabrication Mechanisms, Material Characteristics, and Applications in Energy Storage. *Chemical Engineering Journal* **2024**, *493*, 152805. https://doi.org/10.1016/j.cej.2024.152805.
(78) Movaghgharnezhad, S.; Kang, P. Laser-Induced Graphene: Synthesis Advances, Structural Tailoring, Enhanced Properties, and Sensing Applications. *Journal of Materials Chemistry C* **2024**, *12* (19), 6718–6742. https://doi.org/10.1039/D3TC04677J.
(79) Childres, I.; Jauregui, L. A.; Park, W.; Cao, H.; Chen, Y. P. Raman Spectroscopy of Graphene and Related Materials. In *New Developments in Photon and Materials Research*; Jang, J. I., Ed.; 2013.
(80) Dresselhaus, M. S.; Jorio, A.; Saito, R. Characterizing Graphene, Graphite, and Carbon Nanotubes by Raman Spectroscopy. *Annual Review of Condensed Matter Physics* **2010**, *1* (Volume 1, 2010), 89–108. https://doi.org/10.1146/annurev-conmatphys-070909-103919.
(81) Wang, Y.; Alsmeyer, D. C.; McCreery, R. L. Raman Spectroscopy of Carbon Materials: Structural Basis of Observed Spectra. *Chemistry of Materials* **1990**, *2* (5), 557–563. https://doi.org/10.1021/cm00011a018.
(82) Escribano, R.; Sloan, J. J.; Siddique, N.; Sze, N.; Dudev, T. Raman Spectroscopy of Carbon-Containing Particles. *Vibrational Spectroscopy* **2001**, *26* (2), 179–186. https://doi.org/10.1016/S0924-2031(01)00106-0.
(83) Nathan, M. I.; Smith, J. E., Jr.; Tu, K. N. Raman Spectra of Glassy Carbon. *Journal of Applied Physics* **2003**, *45* (5), 2370. https://doi.org/10.1063/1.1663599.
(84) Lentz, C. M.; Samuel, B. A.; Foley, H. C.; Haque, M. A. Synthesis and Characterization of Glassy Carbon Nanowires. *Journal of Nanomaterials* **2011**, *2011* (1), 129298. https://doi.org/10.1155/2011/129298.
(85) Ferrari, A. C.; Robertson, J. Interpretation of Raman Spectra of Disordered and Amorphous Carbon. *Physical Review B* **2000**, *61* (20), 14095–14107. https://doi.org/10.1103/PhysRevB.61.14095.
(86) Stein, I. Y.; Constable, A. J.; Morales-Medina, N.; Sackier, C. V.; Devoe, M. E.; Vincent, H. M.; Wardle, B. L. Structure-Mechanical Property Relations of Non-Graphitizing Pyrolytic Carbon Synthesized at Low Temperatures. *Carbon* **2017**, *117*, 411–420. https://doi.org/10.1016/j.carbon.2017.03.001.
(87) McCulloch, D. G.; Prawer, S. The Effect of Annealing and Implantation Temperature on the Structure of C Ion-Beam-Irradiated Glassy Carbon. *Journal of Applied Physics* **1995**, *78* (5), 3040–3047. https://doi.org/10.1063/1.360054.
(88) Hogan, Úna. E.; Voss, H. B.; Lei, B.; Smith, R. D. L. Integrating C–H Information to Improve Machine Learning Classification Models for Microplastic Identification from Raman Spectra.

Analytical Chemistry **2025**, *97* (4), 2214–2222. https://doi.org/10.1021/acs.analchem.4c05197.
(89) Franklin, R. E. Crystallite Growth in Graphitizing and Non-Graphitizing Carbons. *Proceedings of the Royal Society A* **1951**, *209* (1097), 196–221. https://doi.org/10.1098/rspa.1951.0197.
(90) Kipling, J. J.; Sherwood, J. N.; Shooter, P. V.; Thompson, N. R. Factors Influencing the Graphitization of Polymer Carbons. *Carbon* **1964**, *1* (3), 315–320. https://doi.org/10.1016/0008-6223(64)90285-4.
(91) Karimi, G.; Lau, I.; Fowler, M.; Pope, M. Parametric Study of Laser-Induced Graphene Conductive Traces and Their Application as Flexible Heaters. *International Journal of Energy Research* **2021**, *45* (9), 13712–13725. https://doi.org/10.1002/er.6701.
(92) Kemppainen, J.; Gallegos, I.; Krieg, A. S.; Gissinger, J. R.; Wise, K. E.; Kowalik, M.; King, J. A.; Gowtham, S.; van Duin, A.; Odegard, G. M. Evolution of Glassy Carbon Derived from Pyrolysis of Furan Resin. *ACS Applied Engineering Materials* **2023**, *1* (10), 2555–2566. https://doi.org/10.1021/acsaenm.3c00360.
(93) Li, L.; Guan, C.; Zhang, A.; Chen, D.; Qing, Z. Thermal Stabilities and the Thermal Degradation Kinetics of Polyimides. *Polymer Degradation and Stability* **2004**, *84* (3), 369–373. https://doi.org/10.1016/j.polymdegradstab.2003.11.007.
(94) Pramoda, K. P.; Chung, T. S.; Liu, S. L.; Oikawa, H.; Yamaguchi, A. Characterization and Thermal Degradation of Polyimide and Polyamide Liquid Crystalline Polymers. *Polymer Degradation and Stability* **2000**, *67* (2), 365–374. https://doi.org/10.1016/S0141-3910(99)00138-X.
(95) Xu, A.; Zhou, J.; Yan, C.; Liu, Z.; Luo, H.; Chen, S. Significantly Enhanced Energy Storage Performance of Polyimide Dielectrics at High Temperatures via Manipulating Crosslinked Density. *Journal of Energy Storage* **2024**, *86*, 111209. https://doi.org/10.1016/j.est.2024.111209.
(96) Moazzen, K.; Zohuriaan-Mehr, M. J.; Jahanmardi, R.; Kabiri, K. Toward Poly(Furfuryl Alcohol) Applications Diversification: Novel Self-Healing Network and Toughening Epoxy–Novolac Resin. *Journal of Applied Polymer Science* **2018**, *135* (12), 45921. https://doi.org/10.1002/app.45921.

Appendix A

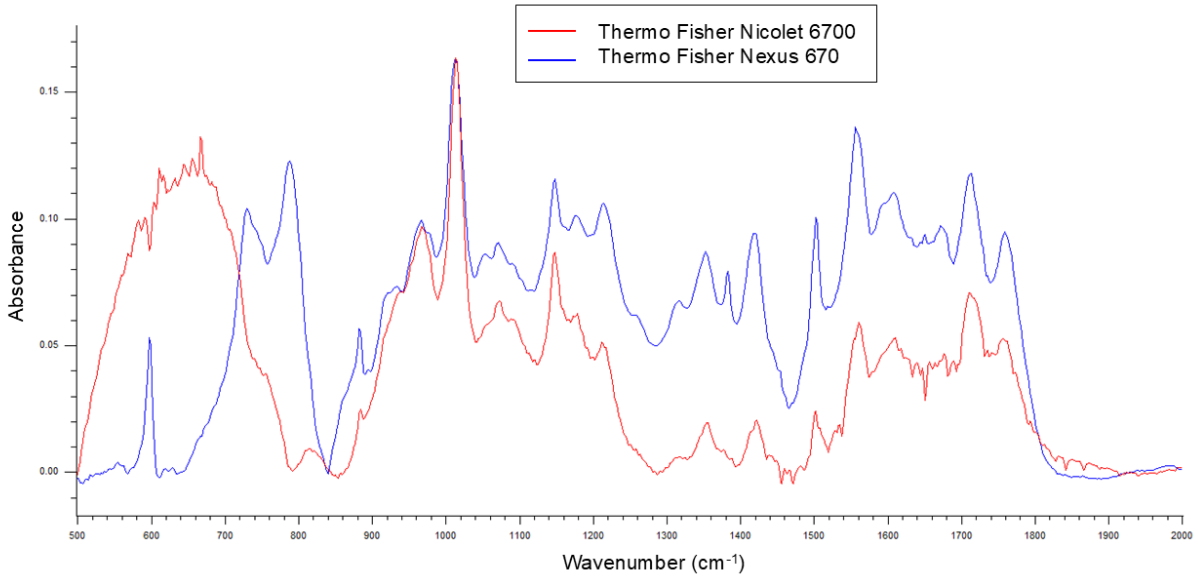


Figure A.1. Comparison of FT-IR spectra of PFA/ethanol from the PFA/solvent series obtained by the Thermo Fisher Nicolet 6700 and the Thermo Fisher Nexus 670, the latter of which could not capture peaks below 900 cm^{-1}.

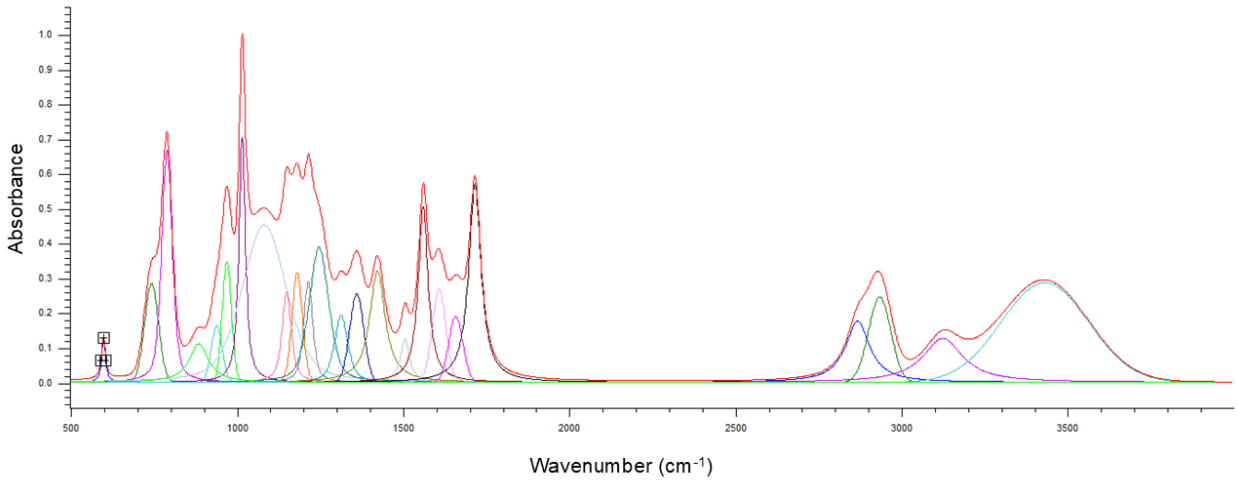


Figure A.2. Example peak fit of the transmission FT-IR spectra of PFA. Example shown is PFA/butanol.

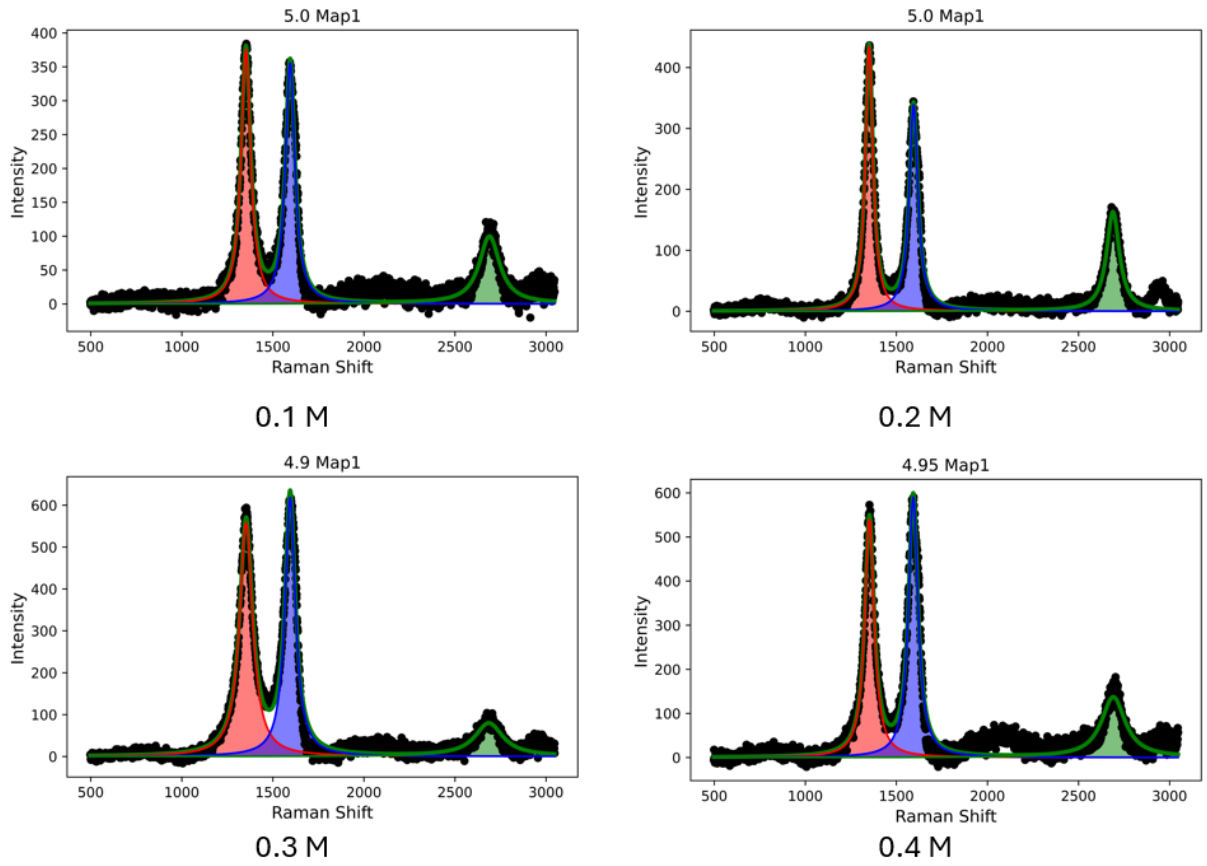


Figure A.3. Lorentzian peak fits of the Raman spectra obtained from the optimal LIC on PFA/acid concentration.

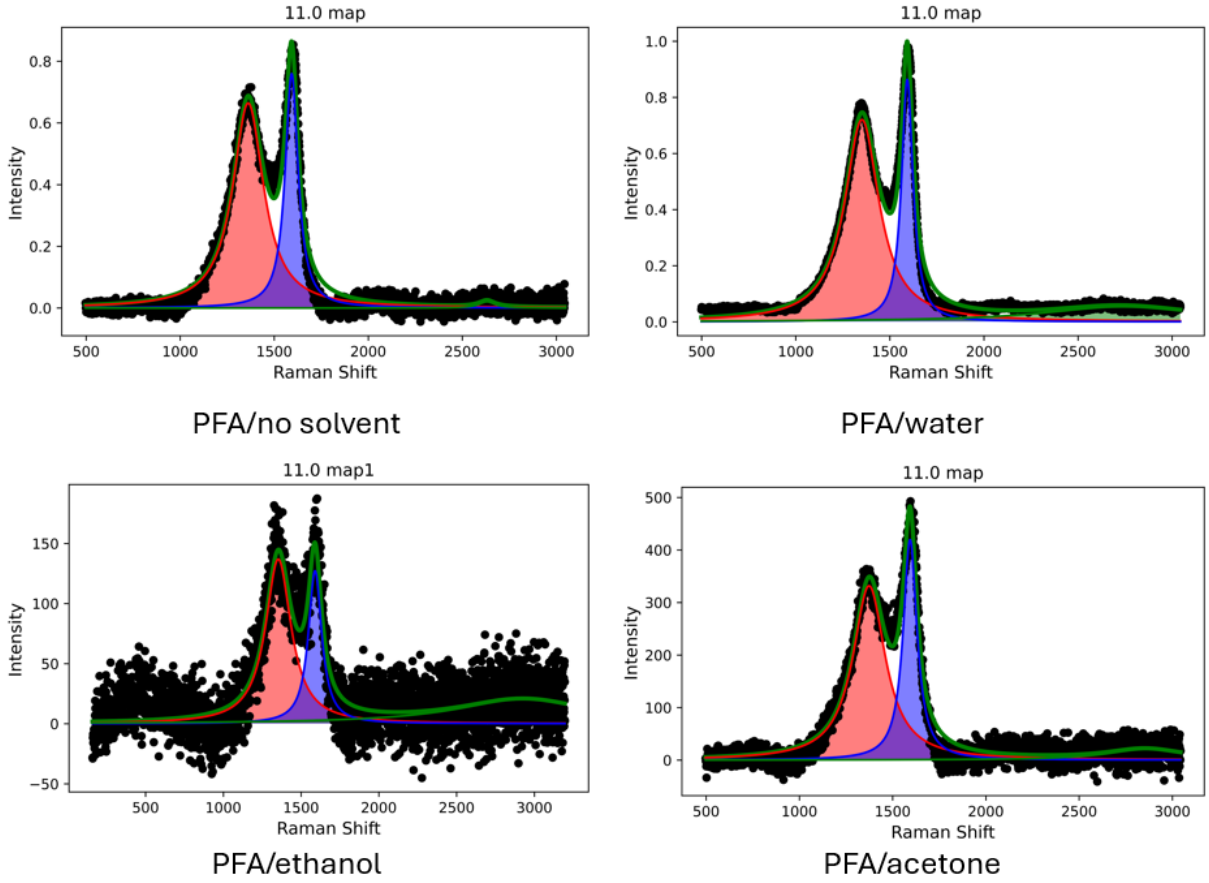


Figure A.4. Lorentzian peak fits of the Raman spectra obtained from the optimal LIC on PFA/solvent.

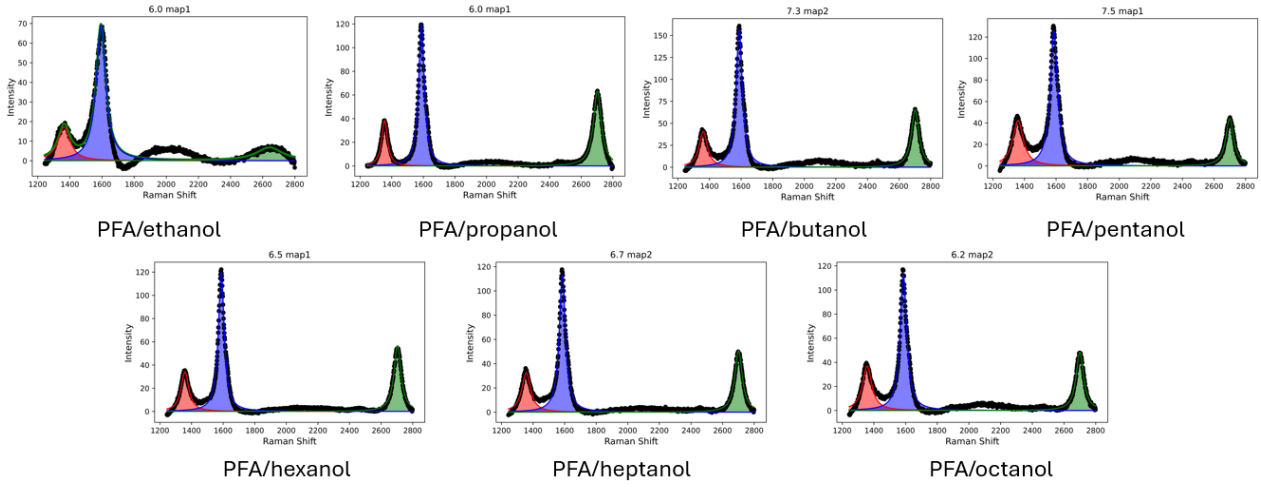


Figure A.6. Lorentzian peak fits of the Raman spectra obtained from the optimal LIC on PFA/alkanol.

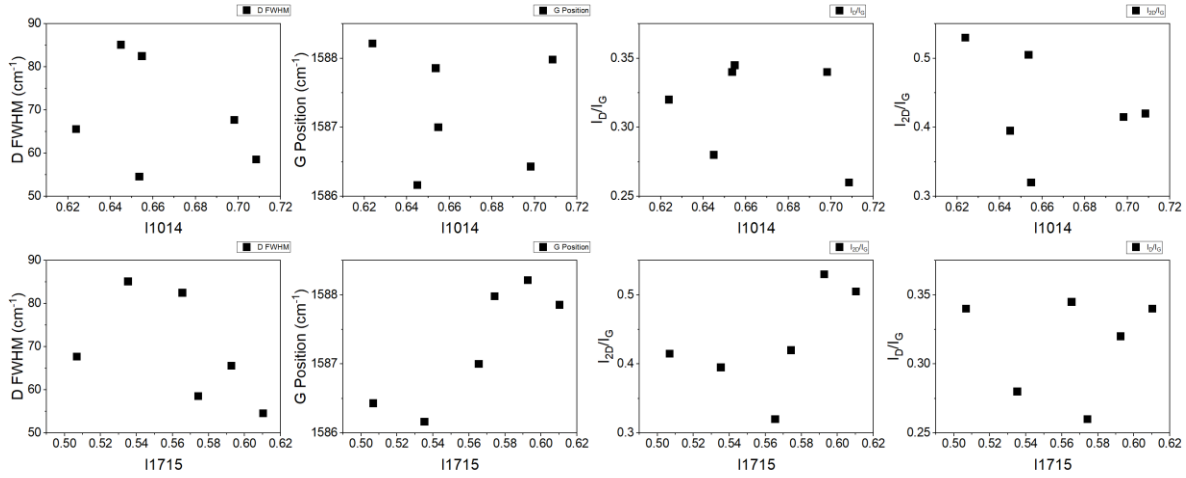


Figure A.5. Raman parameters of the LIC formed from PFA/alkanol as a function of the intensities of the 1014 cm^{-1} and 1715 cm^{-1} bands from FT-IR.